UNIVERSITÀ
DEGLI STUDI
FIRENZE

DOTTORATO DI RICERCA IN
SCIENZE CHIMICHE

CICLO XXVII

COORDINATORE Prof. Goti Andrea

SINGLE-MOLECULE MAGNETS AND SURFACES AT DENSITY FUNCTIONAL LEVEL OF THEORY: A STUDY OF THEIR PROPERTIES BEFORE AND AFTER ADSORPTION

Settore Scientifico Disciplinare CHIM/03

Dottorando
Dott. Ninova Silviya

(firma)

Tutore
Dott. Totti Federico

(firma)

Coordinatore
Prof. Goti Andrea

(firma)

Anni 2012/2014

CONTENTS

1 Introduction **1**

2 Theory **5**
2.1 DFT . . . 5
2.1.1 Exchange-Correlation Functionals . . . 7
2.1.2 London Dispersion Correction DFT-D3 . . . 7
2.2 DFT+U . . . 8
2.3 Simulation of STM image . . . 9
2.4 Density of states . . . 10
2.5 Magnetism and DFT . . . 11
2.5.1 Spin and Spin Hamiltonian . . . 11
2.5.2 Magnetic properties of SMMs . . . 12

3 Isolated Magnetic Clusters **15**
3.1 Computational protocol . . . 16
3.2 Geometry . . . 18
3.3 Electronic properties . . . 18
3.4 Determination of the U parameter and DFT+U results . . . 24

4 Surfaces **31**
4.1 Au(111) . . . 34
4.2 CuN . . . 36
4.3 LSMO . . . 43
4.3.1 Bulk . . . 46
4.3.2 Surfaces . . . 48
4.3.3 Studies of possible contaminants of the surface . . . 63
4.3.4 Conclusion . . . 66

5 Magnetic Molecules on Surfaces **69**
5.1 $Fe_4(dpm)_6$@Au(111) . . . 70
5.1.1 Contaminants . . . 75
5.2 $Fe_4(dpm)_6$@CuN . . . 80
5.2.1 Geometry . . . 80
5.2.2 Magnetic properties . . . 81
5.2.3 Electronic properties . . . 83
5.3 $Fe_4(dpm)_6$@LSMO . . . 87
5.3.1 Geometry . . . 87

5.3.2 Magnetic properties 88
5.3.3 Electronic properties 91

6 Conclusions **95**

Bibliography **97**

Acknowledgements **107**

CHAPTER
ONE

INTRODUCTION

In the past few years, considerable interest has been devoted to the synthesis of new materials to be used in spintronics.[1] This relatively new and very promising branch in material science considers the spin as the main carrier of information. Its nature is exploited to preferentially transport information on one spin over the other, depending on the external magnetic field that is applied and the properties of the magnetic materials.

A new emerging field combines the molecular magnetism and spintronics.[2–5] One of its main goals is to quench the thirst for the increasing on daily basis needs of high-density memory and data storage devices. Promising candidates for such applications are the single-molecule magnets (SMMs).

The SMMs are a special class of molecules, which have a high ground spin state and exhibit slow relaxation of the magnetization at low temperature.[6] Their bulk magnetic properties are of pure molecular origin and are not due to interactions between the clusters, therefore one molecule can be considered as one bit of information.

For practical use, it is important to establish the energy needed to reverse the sign of the magnetization, which determines the magnetic memory effect. In the case of SMMs, the energy potential is presented with the well-known potential well, where the minima represent the two opposite directions of the magnetization (see Figure 1.1). In first approximation, the barrier depends on the ground spin state S_z and the easy-axis anisotropy, characteristic for these compounds. The relaxation of the magnetization follows thermally activated mechanism, where the relaxation time depends exponentially on the inverse of the temperature. One of the most striking features of the SMMs is the quantum tunnelling of the magnetization, which produces the steps observed in the hysteresis of the SMMs. The application of external magnetic field preferentially supports one spin state, blocking the other, which can be very useful in spintronics.

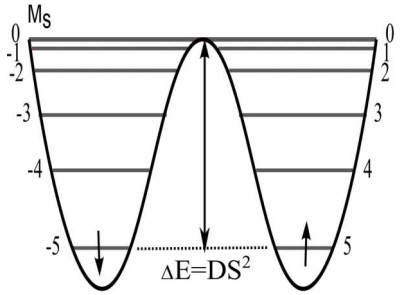

Figure 1.1: General scheme for the energy potential well of the SMMs.

One of the actual challenges in molecular spintronics is to exploit the quantum spin properties of single-molecule magnets (SMMs) when included in new class of spin valves (SV), data storing, and other devices.[5,7–9] The general class of SVs consists of two ferromagnetic layers with different characteristic coercive fields separated by an insulating layer. They work in low and high resistivity modes through the application of external field. Such materials are mainly known for their giant magnetoresistance and tunnelling magnetoresistance, which permits their use for hard-drive devices.

A modern development of the SVs are the organic SVs (OSV), where the isolating layer is substituted with organic semiconductors. Such systems are known to be more flexible than their inorganic equivalents due, for instance, to their long spin diffusion length,[10] properties needed for the spin-polarized injection and transport applications.[11] A very successful example developed by Xiong et al. is presented in Figure 1.2.

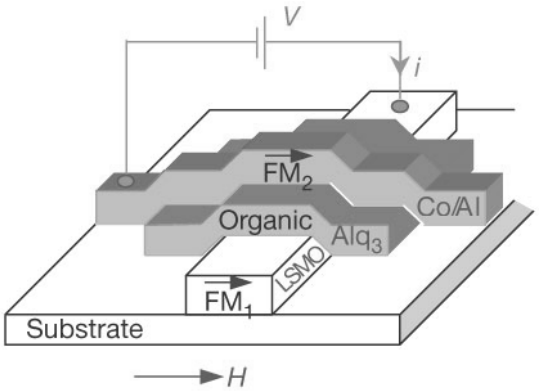

Figure 1.2: An example of spin valve presented by Xiong et al.[12]

The interface between the organic semi-conductor and the magnetic electrode is known to be the origin of losses in the spin polarization of the current through the device. The implementation of a thin layer of SMMs in the specific interface is expected to tune the interaction, by acting as a spin filter. The spin filters inject spin of only one direction from the substrate to the semiconducting layer, giving thus rise to spin waves. Indeed, a theoretical study of the Mn_3Ni SMM grafted between two Au leads proved the suitability of the class for such applications.[13]

The implementation of SMMs in such devices inevitably entails their interaction with different kinds of surfaces. The flexibility of their molecular structure plays a major role. The SMMs have a magnetic core, responsible for the magnetic behaviour, which usually consists of a small number of paramagnetic ions, transition metals and/or rare-earth ones, linked by organic bridges. The core is protected from the environment by organic ligands, which can be tailored for adsorption on different surfaces or junctions, through chemisorption or physisorption.

However, the passage from bulk crystalline phase to adsorbed one can have serious consequences on the properties of such systems. While the SMMs exhibit magnetism and stability in bulk phase, they are by no means guaranteed upon grafting. Indeed, such big complexes can easily be too fragile for deposition on surfaces. Moreover, there are examples of SMMs, such as bis(phthalocyaninato)terbium(III) ($TbPc_2$), that lose their magnetic properties upon sublimation on metallic surfaces.[14–18] Therefore, it is necessary first to have a complete understanding of the behaviour of these complex molecular systems in assembled hybrid structures.

A reliable picture of the adsorption process is obtained by a variety of experimental techniques.[19] The structure of the surface and the adsorbed molecules are estimated by time of flight second ion mass spectrometry (Tof-SIMS) and low-energy ion scattering (LEIS). In addition, X-ray photoemission spectroscopy (XPS) is considered very helpful for the determination of elements in the sample, however, its main drawback remains that it cannot be used as a standalone tool. The scanning tunnelling microscopy (STM) is also widely used to study molecules on the surfaces. It successfully determines the topography of the surface and the way the adsorbate are positioned. It also permits to observe the molecular states for certain energy window. Unfortunately, it is easier to identify the observed object when working with flat and simple molecules, which is not the case.

Important information about the interaction with the surface is obtained from the density of states of the molecule. However, they are difficult to observe for monolayers with ultra-violet photoemission spectroscopy (UPS) for instance, since they remain partially or fully covered by those of the substrate. On the other hand, the STM-based dI/dV mapping gives only local information of the sample.

Last but not least, the magnetic properties of the system are determined by X-ray magnetic circular dichroism (XMCD). It gives information about the magnetic state of the ions as well as their environment. However, this technique requires the use of a syncrotron.

In order to fully understand the changes that occur upon adsorption the experimental results need to be complemented with computational methods. The density functional theory (DFT) is a powerful tool for characterization of various systems, reproducing fairly well the experimental data. In the case of such hybrid systems it can provide information about the integrity and orientation of the molecule on the surface. In addition, the electronic structure through the density of states and the simulated STM image can be readily compared with the experimental data, confirming thus the electronic structure of the cluster and the strength of interaction with the substrate. This is very important for the development of a strategy to organize SMMs on surfaces. Moreover, a thorough investigation and reproduction of the electronic and magnetic properties is also mandatory. Such integrated approach has proved to be successful in several studies.[20–25]

The aim of this thesis is to elucidate and evaluate the microscopic interaction between the deposited SMM and the underlying surface and to propose a reliable computational protocol, able to reproduce their specific characteristic properties. Special attention will be given to the changes that occur in the hybrid structures upon their formation, such as discrepancies in their structural, electronic, and magnetic properties with respect to the isolated form. In this way, the thesis confines itself to the study of the adsorption, leaving for the future a thorough investigation of the spin transport, where methods beyond the density functional theory are required.

The SMM of interest is part of the Fe_4 family. Other members have already been studied experimentally and theoretically and are known to retain their magnetic properties upon grafting on conducting surfaces.[26] The special features of the SMM used in this study is that it can be evaporated, which is crucial for its deposition on highly reactive metals. Moreover, the chemistry of its ligands implies a physisorption on the substrates.

Three different surfaces have been considered - Au(111), Cu(100)$c(2\times2)$N, and LSMO ($La_{1-x}Sr_xMnO_3$). The complexity of the surfaces studied passes from the relatively simple and widely studied conducting one to ferromagnetic oxide surface. Moreover, in the latter case, special attention is also needed to reproduce its magnetic properties. The material is widely used in spintronics for the construction of SVs (see Figure 1.2) since

it is known to exhibit colossal magnetoresistance effect. Indeed, the final goal is to be able to predict the behaviour of the Fe_4 clusters on LSMO and eventually to check their suitability to act as spin filters.

The complexity and variety of the hybrid structures are an even greater challenge for the computational protocol. It is also interesting to observe the different influence that a conducting and ferromagnetic surface has on SMMs. The methodology acquired assumes first the study of the SMM and surfaces separately, and once a good agreement with the available experimental results has been achieved, the study can continue with the investigation of the adsorbed systems.

The structure of the thesis is the following:

Chapter 2 briefly presents the computational methods that have been used throughout the thesis and their reliability. Special attention is given on the mixed Gaussian plane-wave DFT framework and the DFT+U approach. In addition, a brief review of the evaluation of the magnetic properties at a theoretical level of such complex systems is also presented.

Chapter 3 contains the results of the study of the SMM in the bulk phase. Two SMM, $Fe_4(dpm)_6$ and $Fe_4(pta)_6$, are presented. A stress has been put on the difference induced upon fluorination of the ligands as well as the reproduction of UPS spectra and experimental magnetic data through two different approaches - hybrid functional and DFT+U approach. Moreover, the procedure for the setting of the U parameter is explained in detail.

Chapter 4 consists of three sections for the three different surfaces that have been studied - Au(111), Cu(001) $c(2\times2)$N and $La_{1-x}Sr_xMnO_3$. Each models has been tested for reproduction of the electronic, structural and where present, magnetic properties.

Chapter 5 covers the results of the study of the SMM deposited on the different surfaces with thorough analysis and comparison with the experimental results.

The last chapter draws the general conclusion of the behaviour of the SMM on the different surfaces as well as comments on the reliability of the presented computational protocol.

CHAPTER
TWO

THEORY

In the recent years, the density functional theory (DFT) has established itself as a reliable tool for the study of the properties of various range of systems. Its general performance is generally satisfactory, which explains its wide use. It is reasonably fast and it gives reliable geometries, which are among the advantages of the DFT scheme. However, the good results strongly depend on the exchange-correlation (XC) functionals, since they are approximate and while they succeed to describe certain systems, they fail for others. Moreover, the dispersion interactions are not considered explicitly, so a correction is needed to account for them. Last but not least, one of its most serious failures concerns the treatment of strongly correlated systems. Therefore, the study of metal systems needs special attention and the use of additional methods.

The following section presents the approaches and corrections to DFT used to study the hybrid structures investigated in this thesis.

2.1 DFT

The electronic energy within the Kohn-Sham formulation is presented with the equation 2.1:

$$E^{el}[\rho] = E^{T}[\rho] + E^{V}[\rho] + E^{H}[\rho] + E^{XC}[\rho] \tag{2.1}$$

where $E^{T}[\rho]$ is the kinetic energy, $E^{V}[\rho]$ is the electronic interaction with the ionic cores, $E^{H}[\rho]$ is the electronic Hartree energy, and $E^{XC}[\rho]$ is the exchange-correlation energy. Within this method, the electronic density is described with a set of orbitals and their corresponding occupation numbers (see equation 2.2). These Kohn-Sham orbitals are linearly expanded in basis functions (see equation 2.3).

The choice of the basis set is of great importance. On one hand, there are the historical Gaussian-based basis sets. They are localized, accurate, but also expensive and present the basis set superposition error (BSSE). They are still preferred for the description of molecules. On the other hand, the plane-wave (PW) basis sets are usually used for periodic systems. They are used together with pseudopotentials, which eliminate the core electrons and thus reduce the number of orbitals to be calculated. The PWs are independent of the atomic position and do not lead to BSSE. In addition, they facilitate the calculation of the Hartree potential and their accuracy is adjustable by varying their cut-off. However, one of their drawbacks is the computational inefficiency for the

description of molecules. The precision with which the atom-filled and empty regions are treated is the same, so they are also very much memory-demanding.

In 1997, Lippert et al. combined the advantages of both of the above-mentioned basis sets and presented a DFT-based algorithm for periodic and non-periodic *ab initio* calculations called Gaussian and plane waves method (GPW). The scheme uses pseudopotentials in order to integrate out the core electrons from the problem. The valence pseudo-wavefunctions are expanded in Gaussian-type orbitals and the density is represented in a plane-wave auxiliary basis.[27]

The density is defined as spin-restricted orbitals $\{\Psi_i\}$ with their occupation numbers f_i (see equation 2.2). The former on their turn are expanded in a basis set of Gaussian-based localized functions $\{\varphi_\mu\}$ (see equation 2.3). Since they are going to be used in periodic conditions, the orbitals are turned into a periodic function (see equation 2.4).

$$\rho = \sum_i f_i |\Psi_i|^2 \tag{2.2}$$

$$\Psi_i(\mathbf{r}) = \sum_i C_{\mu i} \varphi_\mu^{\mathbf{P}}(\mathbf{r}) \tag{2.3}$$

$$\varphi_\mu^{\mathbf{P}}(\mathbf{r}) = \sum_i \varphi_\mu(r - l_i) \tag{2.4}$$

In agreement with the PW scheme, pseudopotentials are used to describe the interaction of the valence electrons with the nuclei and the core electrons by effective potentials. The norm-conserving separable dual-space Goedecker, Teter, Hutter (GTH) pseudopotentials are preferred, since they are based on Gaussians depending on small number of parameters, and are characterized with accuracy and transferability.[28]

The auxiliary basis sets, in this case the PWs, serve in the expansion of the electronic density. For periodic system the density is expressed as:

$$\rho(\mathbf{r}) = \frac{1}{\Omega} \sum_G \rho(\mathbf{G}) \exp^{i\mathbf{Gr}} \tag{2.5}$$

where the sum is over all reciprocal lattice vectors, and Ω is the volume of the periodic cell in real space. The expression in equation 2.5 can be truncated and limited to the sum of the PWs, whose kinetic energy is smaller than the preassigned cut-off $\frac{1}{2}G_c^2$. This is a density cut-off, different from the one usually referred in PW calculations, which is a wavefunction cut-off. In order to get an equivalent value, the latter should be multiplied by a factor of four. The accuracy of the calculation of the electronic density depends on the PW cut-off and on the screeening parameter, ε_s, which determines the integration range on the basis of overlap integral.

The GPW is a method suitable for the study of adsorbed systems for several reasons. Firstly, the advantages of both Gaussian and PW basis sets are exploited, therefore the vacuum space, which appears with the surface creation, is adequately described. Secondly, large simulation cells are needed to host the molecules on the surfaces. The study of large systems is the strong point of the GPW, since it scales almost linearly with the system size, unlike the PW codes, typically scaling quadratically. Moreover, the fact that the sampling of the Brillouin zone is covered by the Γ point is accepted and justified for large systems. Indeed, GPW and the k-point PW calculations give similar results for the electronic and magnetic properties of transition metal surfaces and bulk, both in good agreement with the experiment, when a sufficiently large number of atoms

are used.[29] Last but not least, even though the periodicity is implicitly included, it can be evaded and isolated systems, needed for preliminary investigation on the adsorbed molecule for instance, can be studied by correctly choosing the size of the simulation cell. This proves that GPW is a valuable and accurate tool for the study of complex systems.

2.1.1 Exchange-Correlation Functionals

One of the main difficulties stemming from the way DFT is defined remains the choice of the XC functional, which best describes the investigated systems. These functionals are divided into three main groups - local density approximation (LDA), generalized gradient approximation (GGA), and meta-GGA, depending on the way the density is calculated at a certain point in space.

GGA functionals are known to improve the total energies, the atomization energies, the energy barriers and the structural energy differences. In the recent years, the established functional for solids is PBE.[30] On the other hand, one of its revised versions, revPBE,[31] improves both the atomic total energies and the molecule atomization energies, making it more suitable for simulation of molecules. Another derivative is the PBEsol functional, which is designed for the description of solids and their surfaces.[32]

Problematic remains the choice of functional for the study of hybrid systems. In 2010, Fabiano et al. proposed a functional designed for such systems - PBEint.[33] Tested on gold nanoparticles, it gives a well balanced description of atomization energies, structural properties, energy differences between isomers, and bulk properties.[34] Unfortunately, PBEint has not been implemented yet in the Cp2k program, therefore the revPBE and PBEsol functionals have been used for the hybrid systems studied in this thesis.

2.1.2 London Dispersion Correction DFT-D3

The standard DFT does not account for the London dispersion interactions. However, these are very important for the accurate description of physisorption processes and of systems possessing hydrogen bonds. There are several methods in literature which propose different ways to correct this shortage. In a recent review,[35] Grimme discusses four different approaches - (a) vdW-DF methods whereby a non-local dispersion term is included explicitly in the functional, (b) parameterized functional which accounts for some dispersion (like the M06-2x functional), (c) semiclassical corrections, labeled typically as DFT-D, which add an atom-pair term that typically has an r^{-6} form, and (d) one-electron corrections. The third one, developed by the author, is proven to be robust and suited for different kinds of systems, where intra- and intermolecular interactions are of great importance, as well as for surface science and solid state chemistry.

In this work, the latest version of the Grimme's method, DFT-D3,[36] has been used as implemented in Cp2k. The resulting total energy (E_{DFT-D3}) is obtained by subtracting the dispersion energy (E_{disp}) from the standard Kohn-Sham energy (E_{KS-DFT}) 2.6:

$$E_{DFT-D3} = E_{KS-DFT} - E_{disp} \tag{2.6}$$

The dispersion energy is described by the sum of the two-body correction energies 2.7, where the three-body ones have not been taken into consideration. It is the sum over all atom pairs , where s_n are the scaling factors, truncated at $n = 6, 8$; C_n^{AB} are the n-th order dispersion coefficients, and $f_{d,n}$ are the dampling functions, which are used to determine the range of the dispersion corrections (equation 2.8) and depend also on

the cut-off radius R_0^{AB}.

$$E_{disp} = \sum_{AB} \sum_{n=6,8} S_n \frac{C_n^{AB}}{r_{AB}^n} f_{d,n}(r_{AB}) \tag{2.7}$$

$$f_{d.n}(r_{AB}) = \frac{1}{1 + 6\left(\frac{r_{AB}}{s_{r,n} R_0^{AB}}\right)^{-\alpha_n}} \tag{2.8}$$

The parameters α_6 and α_8 are adjusted manually and fixed to the values 14 and 16, respectively. With $s_{r,8}$ fixed to 1, the other parameters, s_6, s_8, $s_{r,6}$, are adjusted according to the exchange-correlation functional used for the specific systems.

In the present work, the DFT-D3 method has been tested on a simpler model of benzene dimers adsorbed on Au(111) surface. Satisfactory results in agreement with the experiment have been obtained, therefore the method has been included in the calculation of more complex systems, such as SMMs on surfaces.

2.2 DFT+U

One of the major drawbacks of the DFT is its failure to describe properly correlated materials, such as metals. Indeed, the theory tends to over-delocalize the valence electrons and to stabilize metallic ground states. This is a consequence of the fact that the charge distribution of an electron interacts with itself resulting in repulsion, called self-interaction error (SIE). This error appears as a result of the approximation of the XC functional. In fact, the SIE is introduced by the Coulomb term even in the Hartree-Fock (HF) model, however, it is cancelled out by the exact exchange term. This is not possible in DFT since the XC functional is not exact.

A way out of this problem is the use of hybrid functionals. In these cases, a portion of the exact Hartree exchange term is added to the approximate functionals. The amount varies from functional to functional and is determined semi-empirically. In the case of PBE0, for instance, only 25% of the E_X^{HF} is included, which makes it a reliable functional for a lot of properties and systems. The expression for its XC energy is the following:[37]

$$E_{XC}^{PBE0} = E_{XC}^{GGA} + 0.25(E_X^{HF} - E_X^{GGA}) \tag{2.9}$$

However, the hybrid functionals are computationally expensive, since they scale as $O(N^4)$. They are affordable for small compounds, such as isolated molecules, but become cumbersome for large hybrid systems, as the ones in this study.

Another method, which corrects this shortcoming of the DFT, is the Hubbard-based DFT+U method.[38,39] The advantages of this method are its cheapness and easy implementation, which makes it ideal for studies of isolated and adsorbed systems. The idea is to describe in a special way only strongly correlated states, while the remaining states are treated at DFT level. The general formula for the total energy is presented in equation 2.10:

$$E_{DFT+U}(n, \hat{n}) = E_{DFT}(n) + E_U(\hat{n}) - E_{dc}(\hat{n}) \tag{2.10}$$

The Hubbard HF-like term E_U takes into account the on-site interactions. It is added to the approximate energy E_{DFT}, subtracting the double-counting (dc) term, which treats the contributions from the localized orbitals in the E_{DFT} term. $\hat{n}$ is the operator for the number of electrons occupying a particular atomic site.

Dudarev et al. proposed a simplified and rotationally invariant DFT+U method (see equation 2.11).[40] This version has been implemented in the Cp2k program package.

$$E_{DFT+U} = E_{DFT} + \frac{(\bar{U} - \bar{J})}{2} \sum_{\sigma} \Big[\Big(\sum_{m_1} n^{\sigma}_{m_1,m_1} \Big) - \Big(\sum_{m_1,m_2} \hat{n}^{\sigma}_{m_1,m_2} - \hat{n}^{\sigma}_{m_2,m_1} \Big) \Big] \quad (2.11)$$

In this approach, the spherically averaged matrix elements of the screened Coulomb, U, and exchange, J, interactions are not treated separately, but an effective U parameter, U_{eff} is used instead (referred to as U through the thesis). $\hat{n}^{\sigma}_{m}$ is the operator for the number of electrons occupying a particular site with a projection of the spin σ. n^{σ}_{m} is the occupation number of the mth state.

The final version of the energy expression (equation 2.12) is invariant with respect to a unitary transformation of orbitals. ρ^{σ}_{lj} denotes the density matrix of the electrons and the last term represents the dc correction. It is important to stress out that the DFT+U is used to correct only states, for which the SIE is expected to be larger.

$$E_{DFT+U} = E_{DFT} + \frac{(\bar{U} - \bar{J})}{2} \sum_{l,j.\sigma} \rho^{\sigma}_{l,j} \rho^{\sigma}_{j,l} \quad (2.12)$$

The results in this approach depend on the parameter U. In general, there are two mainstreams to determine its value for a specific system. The strictly *ab initio* approaches include many ways of evaluation among which are: 1) the U is computed as second derivative of the energy with respect to the occupation of the orbitals, and 2) it is evaluated by projecting unrestricted HF molecular orbitals onto atomic orbitals and retaining only on-site (intra-atomic) terms from the HF interactions, averaged over the states (of specific angular momentum) of the same atoms.[41] *and references therein*

The other mainstream includes the semi-empirical approach, where the parameter is fitted to experimental data. When molecules are concerned, usually their density of states is used to match the experimental ultra-violet photoemission spectra (UPS), or U is chosen in agreement with an observed band gap. In solids, the lattice constants and bulk modulus are considered as well.

The DFT+U is cheap and to a certain extent transferable for similar systems, especially when molecules are considered, therefore its applicability to adsorbed systems is tested in this thesis, in comparison with hybrid functionals where possible.

2.3 Simulation of STM image

The scanning tunnelling microscopy (STM) is a powerful tool for studying the structure of surfaces and adsorbed molecules at atomic level. The experiment consists in scanning a conducting surface with a metallic tip. By applying a voltage bias, electrons from the tip tunnel to the surface (or vice versa) and thus scan its energy levels. STM images give information about the electron density in a certain energy window and about the geometry/roughness of the surface or adsorbed molecules. However, often it is quite challenging to associate the observed objects with certain species. Therefore, it is mandatory to support the experimental data with theoretical simulations.

There are two theoretical ways of simulation of STM images. The first is the Bardeen approach,[42] which is based on time dependent perturbation theory. It treats the system and the tip first separately and then the current flow is calculated between the two at a surface in the vacuum.

The second approach is the Tersoff-Hamann.[43] It shows that the current at the position of the tip is proportional to the local density of states. Therefore, for a given energy window, the projected charge density is computed as a sum of the states from the Fermi level to the selected bias multiplied by their corresponding occupation numbers. It is assumed that the wave function of the outermost tip atom is an atomic s-wave-function. Tersoff-Hamann method is not dependent on the tip and is easy to calculate, for that reason it is used in the majority of electronic calculation programs. However, it could produce unreliable images, when more complex tips are used in the experiment.

In order to have reliable STM images to compare with the experimental ones, it is important that the simulation is within the right energy window and thus the right states. The DFT is a ground state calculation, therefore it is assumed that when the occupied states are probed, they should correspond to the experimental bias used. However, when probing the empty states the gap should be taken into consideration, since DFT usually underestimates it.[44]

In this thesis, the Tersoff-Hamann approach has been used as implemented in Cp2k program package.

2.4 Density of states

Investigation of the electronic structure of isolated molecules and surfaces is done using the density of states (DOS). From a theoretical point of view, the DOS is the number of states per interval of energy. The total DOS (TDOS) is computed according to equation 2.13. It does not discriminate with respect to element, molecular orbital or spatial distribution.

$$n(E) = \sum_i \delta(\epsilon_i - E) \tag{2.13}$$

The projected DOS (PDOS), instead, provides the contributions from specific orbitals, by projecting onto a given subset of basis set functions:[29]

$$n_d(E) = \sum_i \left[\sum_{\alpha \in d} |\langle \psi_i | \varphi_\alpha \rangle|^2 \delta(\epsilon_i - E) \right] = \sum_i \left[\sum_{\alpha \in d} (S^{1/2} P^i S^{1/2})_{\alpha\alpha} \right] \tag{2.14}$$

where $S = [\langle \varphi_\alpha | \varphi_\beta \rangle]$ is the overlap matrix and $P^i = [C_{\gamma i} C_{\gamma' i}]$ is the density matrix associated with the ith state. Within the GPW method, the DOS covers only the explicitly treated electrons, which are determined from the pseudopotential. Typically, the DOS needs to be convoluted with Gaussians with width σ in order to match the experimental spectra.

The most frequently used experimental techniques for the study of the electronic structure of molecules are the ultraviolet photoemission(UPS), variable energy photoemission, resonant photoemission, and valence band X-ray photoemission (XPS) spectroscopies. They all study the occupied states of the system, which permits a direct comparison with DFT results.

In the case of surfaces of solids, the angle-resolved photoemission spectroscopy (ARPES) is used, since it produces the DOS with variation of the angle of measurement, thus giving prevalence of the surface over the bulk states. In addition, the STM is also used, since it can measure the Local DOS (LDOS) of the surface in two manners. The dI/dV

map shows the DOS for a certain bias energy as a function of the position, whereas the dI/dV spectrum measures the LDOS as a function of the energy at a certain position.

2.5 Magnetism and DFT

Magnetism has been known since antiquity. Today, it is exploited in some of the most modern technologies, and it pioneers the way of spintronics as most promising and leading field for memory and data storage applications.

The orientation of the magnetic moments in materials gives rise to different kinds of magnetic interaction. The paramagnetism has spin moments randomly oriented, which strongly react with an external field. On the other hand ferromagnetic materials have perfectly aligned spin moments and this behaviour does not depend on the external field. There are also systems where the neighbouring spins have opposite direction. When the total magnetic moment is zero, it is called antiferromagnetism, and when it is not, this is ferrimagnetism.

The magnetic properties on molecular level are generally described by two types of interaction between paramagnetic centres - trough-space and through-bond. The first is characterized by a weak interaction resulting in magnetic coupling, while the second is strong, electrostatic in origin, and it describes the chemical bond. The strength of the molecular magnetic phenomenon is evaluated by determining the interaction. Exchange interaction occurs directly between two paramagnetic centres, while the super-exchange happens through a diamagnetic ligand.

In the following sections, the attention will be focused on the description of the spin and the magnetic interactions in close relation to the single-molecule magnets. The super-exchange mechanism will de discussed in Section 4.3 with respect to the LSMO system, where it appears.

2.5.1 Spin and Spin Hamiltonian

The experiment of Stern and Gerlach (1922) led to the discovery of a new intrinsic property of the particles with no classical equivalent. It has been described by Goudsmit and Uhlenbeck in 1925 and later Pauli denoted this property as "spin". The spin is an intrinsic characteristic of the electron and its value is $\frac{1}{2}$. Its operator can be presented as in equation 2.15, where σ_i are the Pauli matrices. Moreover, it can be decomposed into three components with respect to the orientation in space (see equation 2.16).

$$\hat{\mathbf{s}} = \frac{\hbar}{2}(\sigma_x, \sigma_y, \sigma_z)^T \tag{2.15}$$

$$\hat{\mathbf{s}}^{\mathbf{2}} = \hat{s}_x^2 + \hat{s}_y^2 + \hat{s}_z^2 \tag{2.16}$$

In the case of many-electron systems, the sum of the spins of the individual electrons gives the total spin operator $\hat{\mathbf{S}}$ and its projection $\hat{S}_z$ (see equations 2.17). In agreement with the one-electron equivalents, they commute with the Hamiltonian of the system.[45]

$$\hat{\mathbf{S}}^2 = \sum_{i=1}^{N} \hat{\mathbf{s}}(s_i) \tag{2.17}$$

$$\hat{S}_z = \sum_{i=1}^{N} \hat{s}_z(s_i) \tag{2.18}$$

The magnetic properties arise as a result of the presence of unpaired electrons in atoms, which react to the presence of other unpaired electrons and/or to external magnetic field. In order to evaluate these interactions, a Spin Hamiltonian is needed. An example for two magnetic centres is given in the equation 2.19.[46]

$$H = \sum_{i=1,2} H_i + \mathbf{S}_1 \cdot \mathbf{J}_{12} \cdot \mathbf{S}_2 \tag{2.19}$$

The first term in equation 2.19 covers the contributions of the separate centres (see equation 2.20). It is described by three contributions (equation 2.20). The first, so-called Zeeman, term estimates the interaction of the spin with an external magnetic field, which results in splitting of the spin levels. μ_B is the Bohr magneton, B is the external magnetic field, and g is the g-factor, a tensor which connects the magnetic field and the spin vectors. Second is the crystal field term, which describes zero-field splitting, due to the environment of the magnetic center. In the case of atoms, it estimates their anisotropy, where D determines the axial and E the rhombic anisotropy (see equation 2.21, the modified version of the term in equation 2.20). The last term describes the hyperfine interaction between the magnetic center and magnetic nuclei, where $\mathbf{I}_j$ is the angular momentum operator of the nucleus constituting the magnetic centre i, $\mathbf{A}_j$ is the tensor describing the interaction.

$$H_i = \mu_B \mathbf{B} \cdot \mathbf{g} \cdot \mathbf{S} + \mathbf{S} \cdot \mathbf{D} \cdot \mathbf{S} + \sum_j \mathbf{S} \cdot \mathbf{A}_j \cdot \mathbf{I}_j \tag{2.20}$$

$$H_{CF} = DS_z^2 + E(S_x^2 - S_y^2) \tag{2.21}$$

The second term in equation 2.19 describes the spin interactions between the two magnetic centres (equation 2.22). These are composed of three contributions - isotropic or Heisenberg (first term), anisotropic (second term) and antisymmetric or Dzyaloshinsky-Moriya (third term) (see equation 2.22). The antisymmetric term exists only when there is no center of symmetry.

$$\mathbf{S}_1 \cdot \mathbf{J}_{12} \cdot \mathbf{S}_2 = J_{12}\mathbf{S}_1 \cdot \mathbf{S}_2 + \mathbf{S}_1 \cdot \mathbf{D}_{12} \cdot \mathbf{S}_2 + \mathbf{d}_{12} \cdot \mathbf{S}_1 \times \mathbf{S}_2 \tag{2.22}$$

When the isotropic part is larger than the two other terms describing the spin-spin interaction, $J_{ij} \gg D_{ij}$, the system is within the strong exchange limit. In such cases, the total spin of an isolated pair of spins is considered a good quantum number. Exceptions in this case are the rare earth metals, where the three terms have similar values.

2.5.2 Magnetic properties of SMMs

Interestingly enough, both experiment and theory do not evaluate the magnetic interactions directly. The most widely used method for the extraction of the exchange constants considers magnetic susceptibility measurements with variation of the temperature. The

experimental curve is fitted with a predefined spin Hamiltonian for the specific system, thus enabling the evaluation of the coupling parameters. Complex systems would need more parameters to describe their magnetic states, theorefore help from other techniques may be compulsory.[46,47]

On the other hand, the most widely used approach in the theory to evaluate the exchange coupling constants is the broken symmetry (BS) approach, developed by Noodleman and Norman.[48,49] It is based on the Heisenberg-Dirac-van Vleck (HDVV)[50–52] spin Hamiltonian (equation 2.23) and in order to apply it, only the energies of two single determinants are needed. The first one is the high spin (HS) state, where the spins on the interacting magnetic centres are parallel or aligned ferromagnetically. The second one is the broken symmetry (BS) determinant, where the spins are in opposite direction or antiferromagnetically aligned. While the HS state can be correctly described by a single determinant, this is not the case of the BS one, which is not an eigenstate of $\mathbf{S}^2$.

$$H_{HDVV} = J\hat{\mathbf{S}}_1 \cdot \hat{\mathbf{S}}_2 \tag{2.23}$$

The resulting dependence of the exchange coupling constant on the energies of the HS and BS states for orthogonal magnetic orbitals is presented in equation 2.24. The positive value means the systems prefers antiferromagnetic coupling, while the negative value stands for ferromagnetic direction of the spins.

$$J = \frac{E(HS) - E(BS)}{2S_1 S_2} \tag{2.24}$$

In the case of polynuclear complexes, where more than one coupling parameters are to be considered, a different approach is required. Generally, the HDVV for such systems takes the form:

$$H_{HDVV} = \sum_{i<j} J_{ij}\hat{\mathbf{S}}_i \cdot \hat{\mathbf{S}}_j \tag{2.25}$$

Bencini and Totti applied the BS-based approach to polynuclear complexes, where the HS and a certain number of BS states must be computed. This approach has been successfully applied for the J_{ij} reproduction for different exchange coupling complexes,[53,54] as well as single-molecule magnets.[24,55] For this reason, it is also assumed for the description of the Fe_4 molecules investigated in this study.

The common feature between the members of the Fe_4 family is their magnetic core. It consists of a central Fe(III) ion, which is antiferromagnetically coupled with three Fe(III) ions. The interaction happens through oxygen bridges. There are two J constants to be accounted for - the one of the nearest neighbour (J_1) and the one of the next-nearest neighbour (J_2) (see Figure 2.1). The Fe_4 SMMs can be treated in the strong exchange limit, therefore the sum of the spins on the Fe ions is considered to be good quantum numbers ($S_{Fe} = \frac{5}{2}$). An idealized trigonal symmetry best describes the system. The spin Hamiltonian used to fit the experimental magnetic data is given in equation 2.26.[56,57]

$$H = J_1(\mathbf{S}_1 \cdot \mathbf{S}_2 + \mathbf{S}_1 \cdot \mathbf{S}_3 + \mathbf{S}_1 \cdot \mathbf{S}_4) + J_2(\mathbf{S}_2 \cdot \mathbf{S}_3 + \mathbf{S}_3 \cdot \mathbf{S}_4 + \mathbf{S}_2 \cdot \mathbf{S}_4) \tag{2.26}$$

The calculation of the J_{ij} parameters has been done with the help of five determinants: UUUU, DUUU, UDUU, UUDU, and UUUD (where U and D stay for up and down local spins on the four iron ions). The resulting system of equations is presented in 2.27. The nearest-neighbour parameter J_1 has been evaluated with respect to the three peripheral

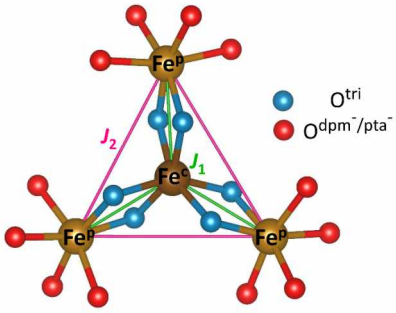

Figure 2.1: Schematic representation of the bonds and magnetic interactions in the Fe_4 core. O^{tri} atoms are in blue and the $O^{dpm/pta}$ are in red. The nearest neighbour exchange constants J_1 are depicted in green while the next-nearest neighbour exchange constants J_2 are in pink.

Fe ions, which provides more information about the different interactions with the central ions. In order to compare with the experimental value, an average value is presented (see equation 2.28).

$$\begin{pmatrix} E_{uuuu} - E_{duuu} \\ E_{uuuu} - E_{uduu} \\ E_{uuuu} - E_{uudu} \\ E_{uuuu} - E_{uuud} \end{pmatrix} = \begin{pmatrix} S_1S_2 & S_1S_3 & S_1S_4 & 0 \\ S_1S_2 & 0 & 0 & S_2S_3 + S_2S_4 \\ 0 & S_1S_3 & 0 & S_2S_3 + S_3S_4 \\ 0 & 0 & S_1S_4 & S_2S_4 + S_3S_4 \end{pmatrix} \begin{pmatrix} J_{12} \\ J_{13} \\ J_{14} \\ J_2 \end{pmatrix} \tag{2.27}$$

$$J_1 = \frac{J_{12} + J_{13} + J_{14}}{3} \tag{2.28}$$

Once there is the scheme for the description of the magnetic properties, it remains to determine the computational protocol. One of the main drawbacks of the DFT when the magnetic interactions are considered is their dependence on the (XC) functional. The pure DFT method is not good since it over-delocalizes the orbitals and therefore overestimates the interaction, which is a consequence of the SIE. Good results are obtained when hybrid functionals are used, as well as with the DFT+U method.

However, the correct description of the magnetic interactions comes at high computational cost. Therefore, in this thesis, the computational protocol consists of geometry optimization of the Fe_4 clusters with pure DFT XC functional in their ground spin state S=5, where the spins on the Fe ions are kept in their high spin state. After that, self-consistent field (SCF) calculations with higher precision have been carried out on the optimized geometry for the different BS states at both hybrid and DFT+U levels of theory. The results presented in the thesis prove the reliability of the chosen protocol.

CHAPTER
THREE

ISOLATED MAGNETIC CLUSTERS

The first step in the study of adsorbed molecules is to find a computational protocol able to reproduce their characteristic features in the bulk phase. It is extremely important that the selected theoretical approach is also cheap and applicable to adsorbed systems, since in that way it can give a clear picture of the changes that occur upon deposition on surfaces.

This chapter is dedicated to the theoretical description of bulk single-molecule magnets and to the importance of the structure of the ligands on the electronic and magnetic properties. More precisely, it is focused on the study of two SMMs belonging to the tetrairon(III) family, Fe_4, namely $[Fe_4(L)_2(dpm)_6]$[56,58] and $[Fe_4(L)_2(pta)_6]$,[57] (Hdpm = dipivaloylmethane, Hpta = pivaloyltrifluoroacetone), labelled hereafter as $Fe_4(dpm)_6$ and $Fe_4(pta)_6$, respectively (see Figure 3.1). These clusters possess a propeller-like molecular structure, where two tripodal ligands (L^{3-} = Ph-$C(CH_2O)_2$ $^{3-}$) connect the central iron ion to the three peripheral ones through double bridging alkoxide oxygen atoms. The three external FeIII ions complete their coordination sphere by binding two β-diketonates (dpm^- or pta^-). Within the Fe_4 family, these two clusters are the only ones to have been successfully sublimated in ultra-high vacuum (UHV) conditions,[58 57] preserving their magnetic properties unaltered. This is a great advantage for adsorption on surfaces, since it is possible to prepare highly pure molecular films suited for *in situ* UHV characterizations.

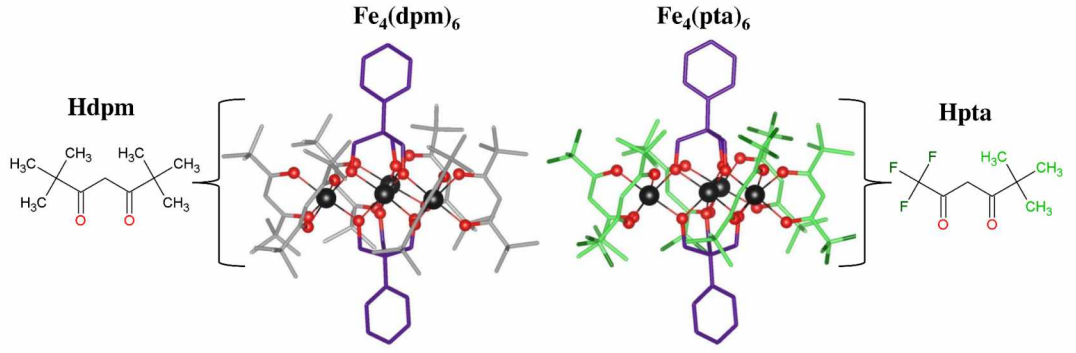

Figure 3.1: Side view of $Fe_4(dpm)_6$ (left) and $Fe_4(pta)_6$ (right). The tripodal ligands are in purple, the dpm^- in grey and the pta^- in green, with F atoms highlighted in dark green. Hydrogen atoms are omitted for a clearer view. A sketch of the β-diketone ligands is also displayed next to the corresponding clusters.

The proper description of the electronic and magnetic structures from a theoretical point of view using density functional theory for different classes of materials and in strongly correlated systems is achieved with the use of hybrid functionals, where the exact Hartree-Fock (HF) exchange is introduced.[54,59,60] There are few DFT studies on Fe_4 propeller-like clusters already present in literature.[61–64] However, there are no calculations of Fe_4 molecules where the pseudopotential Gaussian Plane-Wave (GPW) approach has been used together with a hybrid functional. The latter is mandatory for the isolated molecular systems, but their application to complex magnetic systems within periodic boundary conditions, as SMMs on surfaces, becomes very cumbersome and therefore practically unusable.

For this reason, the alternative parameterized method, DFT+U,[38,39] is introduced, where a HF-like potential describes the interaction between electrons localized on the same centre (on-site interactions) (see Chapter 2). This approach, already tested on other SMMs like Mn_6[65] and Mn_{12},[66–68] is here applied to $Fe_4(dpm)_6$ and $Fe_4(pta)_6$. Through the DFT+U the different element/orbital contributions can be selectively discerned, once the approach has been tuned to a reliable "parameter-free" (hybrid functional) approach and/or to experimental observables. Moreover, a well-defined set of U values could allow a reliable calculation of the evolution of SMM electronic and magnetic properties from bulk to the adsorbed phase, within the approximation of a low deformation of the magnetic core upon adsorption.

The study on the two SMMs is directed in two ways: firstly, the electronic differences induced by the substitution of the dpm^- ligand with the fluorinated one, pta^-, are investigated through an integrated UPS-DFT approach, using the hybrid functional PBE0; then, a computational protocol using DFT+U based on the experimental UPS/PBE0 data is set up. It is to be used for the bulk phase but it is also suitable for the description of adsorbed species in direct contact with surfaces.

3.1 Computational protocol

All calculations were performed with the Cp2k program package[69] within the DFT framework, and the Grimme's D3 parameterization approach[36] was used to introduce the dispersion correction term. Norm-conserving Goedecker-Teter-Hutter (GTH) pseudopotentials[28,70] have been used together with GTH double-ζ polarized molecularly optimized basis sets for all atomic species.[71] An energy cut-off of 400 Ry has been applied to the plane-wave basis sets.

In order to perform plane-wave calculations, the Fe_4 molecules have been put in a full periodic cubic simulation cell with 25 Å side lengths. The shortest distances between the clusters in adjacent simulation cells are about 9.6 and 10.0 Å for $Fe_4(dpm)_6$ and $Fe_4(pta)_6$, respectively. The choice of using a full periodic approach is in the perspective of computing the adsorption process on different surfaces later on.

Both Fe_4 systems were considered in their ground magnetic state (S=5), where the central iron ion, Fe^c, is antiferromagnetically coupled with the peripheral ones, Fe^p, and all ions are kept in their high spin state. The revPBE functional[31] has been chosen for the geometry optimization, where the convergence criteria have been fixed at 1×10^{-6} Hartree for the SCF energy and 1×10^{-3} HartreeBohr^{-1} for the atomic forces. Single point calculations on optimized geometries were also performed at PBE0[37] and revPBE+U levels with a tighter SCF convergence criterion (5×10^{-7} Hartree) in order to obtain the DOS.

In order to account for the experimental resolution and broadening effects, the theoretical TDOS were convoluted with Gaussian functions with a FWHM (σ) of 0.6 and 0.5 eV for $Fe_4(dpm)_6$ and $Fe_4(pta)_6$, respectively. TDOS with Gaussian width of 0.35 eV are also reported for both molecules when explicitly stated. The PDOS are also reported with Gaussian width of 0.35 eV, which allows to better distinguish the different atomic contributions to the TDOS.

As stated in a previous study by Rigamonti et al.,[57] it was not possible to obtain crystals suitable for X-ray diffraction of $Fe_4(pta)_6$. Therefore, three of the possible geometrical isomers, differing in the arrangement of the CF_3 and *t*Bu groups of the ligands (see Figure 3.2), have been chosen in order to reproduce the experimental structure. Two of them have the symmetry of the molecule (formal D_3, neglecting the phenyl groups). The third one has a lower symmetry with mixed arrangement of the pta^- substituents. For this study, when presenting results about $Fe_4(pta)_6$, it would be more correct to take into account a weighted contribution of the three isomers, in order to account for the experimental sample. However, as one can see in Figure 3.3, the TDOS for the three structures are quite similar. Therefore, it has been assumed throughout the study the isomer with the lowest energy as the most representative of the $Fe_4(pta)_6$ cluster.

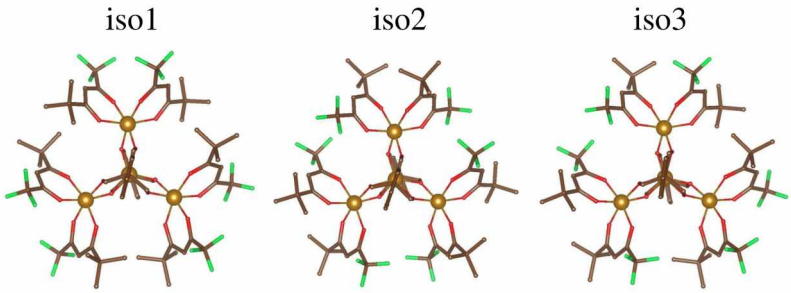

Figure 3.2: Top view of the three possible geometrical isomers of the $Fe_4(pta)_6$ cluster, where Iso1 is the most stable one. Fluorine atoms are in green, carbon atoms - in brown, oxygen atoms - in red, iron atoms - in gold

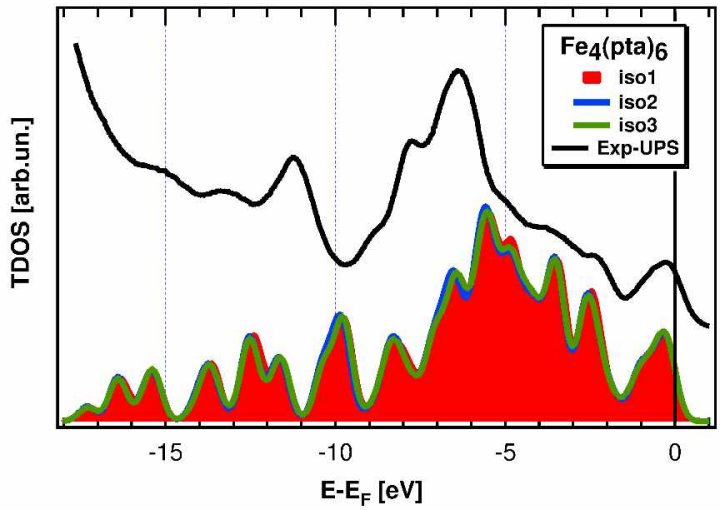

Figure 3.3: TDOS corresponding to the three isomers of the $Fe_4(pta)_6$ cluster

3.2 Geometry

The geometry optimization of the cluster is needed for several reasons. First, it is interesting to evaluate the changes that occur when the cluster is no more in the crystal lattice and it does not feel the interactions with the neighbouring molecules. In addition, the distortions introduced by the theory into the bulk structure must be estimated. This is a way to facilitate the comparison with the geometry of the adsorbed cluster, which can only be hinted by experiments.

The geometry optimization of both clusters tends to elongate the bonds between the iron ions, which is a direct consequence of the use of revPBE functional, known to worsen bond lengths. The C_2 axis passing from Fe_1-Fe_2 is retained also in the optimized structure of $Fe_4(dpm)_6$, as well as in iso1 and iso3 of $Fe_4(pta)_6$ (see Table 3.1). However, the axis is shifted to Fe_1-Fe_3 in iso2. In all models, the Fe ions are co-planar, in agreement with the experimental structure.

An important structural parameter is the angle between the Fe^c and Fe^p, $\langle$Fe-O-Fe$\rangle$. The wider the angle, the larger the J_1 exchange coupling constants are.[56] Its small deviation in the optimized structures from the X-ray value is a sign of similar strength of the magnetic interaction.

The three isomers of $Fe_4(pta)_6$ show significant differences in all important geometry parameters, such as bond lengths and $\langle$Fe-O-Fe$\rangle$ angles. This implies that the disposition of fluorinated ligands considerably affects the geometry of the molecules, due to electronic steric effects, and therefore would strongly influence the electronic properties, through charge distribution.

The resultant optimized structures are very similar, from a geometrical point of view, to the initial X-ray structure. They maintain their integrity and the error with respect to the experimental values is of about 1%. In order to further test the reliability of these structures, studies on their electronic and magnetic properties are necessary.

3.3 Electronic properties

The electronic properties of both clusters have been first studied at PBE0 level of approximation. To check their agreement with the experiment, their TDOS have been compared with the corresponding UPS spectra of thick films. Moreover, in order to gain a deeper insight into the electronic structure of the Fe_4 clusters and to estimate possible differences between them, the DOS projected on the different elements have also been considered (see Figure 3.4).

To facilitate the analysis of Figure 3.4, the experimental curves have been shifted in order to match the barycentre of the first band in region (i) with the corresponding theoretical one. Starting with the comparison between the experimental UPS spectra and the TDOS, the overall good correspondence is clearly appreciable. The first bands (1-4) of the experimental curves match very nicely the computed intensities and energies. However, the energy matching is lost with the fifth band due to the contraction of the theoretical energy scale. This effect strongly depends on the way non-local exchange and correlation effects are included. Indeed, this becomes evident comparing the results computed with a pure DFT functional versus a hybrid one: the use of pure DFT-PBE functional yields much more evident energy shrink than observed in the case of the PBE0 (see below). Moreover, the intensity ratio between the theoretical peaks of region (ii) does not fully reproduce the experimental one for both clusters. Such deviation can be

Table 3.1: Bond lengths and angles of the isolated $Fe_4(dpm)_6$ and $Fe_4(pta)_6$

	X-ray	**$Fe_4(dpm)_6$**	**$Fe_4(pta)_6$**		
			iso1	**iso2**	**iso3**
		Bonds (Å)			
Fe1-Fe2	3.0780(8)	3.139	3.117	3.064	3.136
Fe1-Fe3	3.0726(6)	3.161	3.112	3.096	3.152
Fe1-Fe4	3.0726(6)	3.160	3.110	3.063	3.153
Fe2-Fe3	5.2925(7)	5.402	5.360	5.302	5.392
Fe3-Fe4	5.3880(1)	5.579	5.453	5.396	5.564
Fe2-Fe4	5.2925(7)	5.399	5.360	5.276	5.390
Fe1-O1	1.9801(19)	2.011	2.019	1.999	2.016
Fe1-O2	1.9650(18)	2.005	2.001	1.998	2.002
Fe1-O3	1.9813(19)	2.019	2.002	1.995	2.029
Fe1-O10	1.9801(19)	2.020	2.015	1.999	2.025
Fe1-O11	1.9650(18)	2.004	2.003	1.996	2.001
Fe1-O12	1.9813(19)	2.018	2.004	2.010	2.017
Fe2-O1	1.9718(9)	2.006	1.997	1.987	1.988
Fe2-O4	1.995(2)	2.039	2.047	2.048	2.075
Fe2-O5	2.0321(19)	2.089	2.112	2.109	2.086
Fe2-O10	1.9718(9)	2.009	2.000	1.986	1.997
Fe2-O13	1.995(2)	2.039	2.047	2.062	2.069
Fe2-O14	2.0321(19)	2.090	2.115	2.105	2.083
Fe3-O2	1.9784(19)	2.020	1.999	1.992	2.021
Fe3-O6	1.9853(19)	2.056	2.082	2.079	2.060
Fe3-O7	2.004(2)	2.059	2.072	2.060	2.063
Fe3-O8	1.993(2)	2.036	2.060	2.063	2.056
Fe3-O9	1.9909(19)	2.071	2.079	2.071	2.070
Fe3-O12	1.9718(18)	2.022	1.997	1.993	2.002
Fe4-O3	1.9718(18)	2.018	1.996	1.990	2.003
Fe4-O11	1.9784(19)	2.034	2.002	1.979	2.017
Fe4-O15	1.9853(19)	2.052	2.081	2.073	2.058
Fe4-O16	2.004(2)	2.058	2.065	2.061	2.060
Fe4-O17	1.993(2)	2.035	2.083	2.054	2.045
Fe4-O18	1.9909(19)	2.085	2.063	2.085	2.091
		Angles (°)			
Fe2-Fe1-Fe3	118.74(1)	118.09	118.77	118.76	118.08
Fe2-Fe1-Fe4	118.74(1)	117.98	118.82	118.89	118.00
Fe3-Fe1-Fe4	122.51(2)	123.93	122.42	122.34	123.92
⟨Fe-O-Fe⟩	102.23(17)	102.93	101.98	100.89	103.03
Fe3-Fe1-Fe2-Fe4	180.00	179.90	179.79	179.72	179.80
γ	68.80	70.60	69.4	67.8	71.0

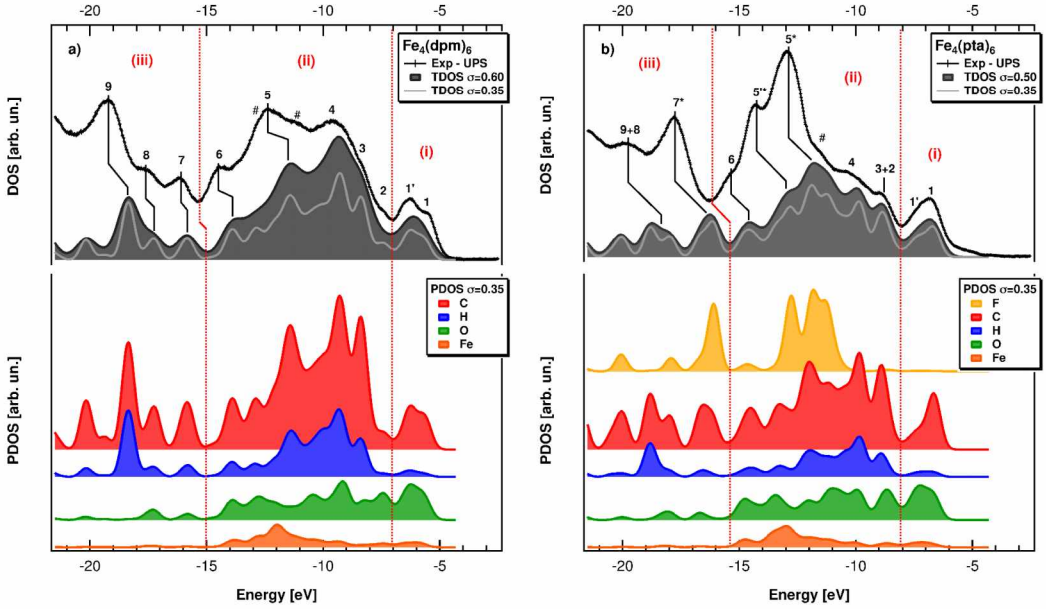

Figure 3.4: Thick film UPS spectra *vs* theoretical TDOS and PDOS for $Fe_4(dpm)_6$ (a) and $Fe_4(pta)_6$ (b). The PDOS are plotted on a different ordinate axis scale with respect to the TDOS in order to better appreciate the small contribution of Fe PDOS.

ascribed to the photoionization cross section which affects differently each element (H, C, O, F, Fe) and state ($1s$, $2s$, $2p$, $3d$) in UPS spectra.[72]

In order to disentangle the contribution of each element to the TDOS, the PDOS have been reported in the bottom part of each graph. In both cases the first band of region (i) is mainly due to states localized on carbon and oxygen atoms. Region (i) represents the case in which the TDOS with a smaller Gaussian width (σ) reproduces better the experimental spectrum. This is particularly evident for $Fe_4(dpm)_6$ where the double structure of the first band is clearly visible in TDOS with $\sigma \leq 0.35$ eV. On the other hand, the TDOS reported with higher σ value already hints the asymmetric shape of the first band of $Fe_4(pta)_6$.

The assignment of the features belonging to region (ii) is more challenging because of the many overlapping states and the aforementioned energy shrink. However a coherent (but arbitrary) numeration of the bands can be attempted for both molecules. Bands indicated with hash marks (#) have not been considered for numeration because of the not clear correspondence with the theoretical ones. In the case of $Fe_4(dpm)_6$, bands 3-6 are mainly due to the carbon and hydrogen states with a non-negligible oxygen contribution. In the same region the iron states are marginally involved compared to the carbon and hydrogen ones. On the other hand, the small band labelled as 2 (see exp. and TDOS σ=0.35 eV) arises mainly from oxygen states with a small contribution from the carbon ones. Region (ii) of $Fe_4(pta)_6$ shows, instead, that the carbon and hydrogen PDOS are significantly reduced due to the substitution of three methyl groups with as many fluorine atoms on each pta^- ligand. At the same time, a new band due to F atoms overlaps with the states wrapping around the peak previously labelled as 5. The new band, consisting of two peaks, is now indicated as 5* and 5'* in order to mark the fluorine contribution. A slighter difference can be also observed in the first part of region (ii): the peak previously labelled as 2 and mainly due to oxygen states is now overlapping

with the carbon and hydrogen states which were responsible, in $Fe_4(dpm)_6$, for peak 3.

The fluorine states strongly affect also the last part of region (iii) of the TDOS. Peak 7 of $Fe_4(dpm)_6$ is not very intense because it arises, almost entirely, from the carbon PDOS. In the fluorinated cluster, the same carbon states are energetically equivalent with the fluorine band, which is responsible for the gained intensity of peak 7*. At the same time the intensity of peaks 9 and 8 of $Fe_4(pta)_6$ decreases making difficult to discriminate them in the experimental curve.

The analysis of region (i) deserves particular attention. As a consequence of the high electronegativity of F atoms, the valence band of $Fe_4(pta)_6$ is shifted towards more negative values as compared to the $Fe_4(dpm)_6$ one. Deconvolution of the experimental curves allows to estimate an energy shift of about 0.8 eV in good accordance with the theoretical value of 1.0 eV (see Figure 3.5). Much more interesting is the shape of the first band, which is quite peculiar for each molecule. For both clusters, the fitting of the experimental curves reveals the presence of two components (1 and 1'), separated by the same amount of energy (0.7 - 0.8 eV). On the other hand, the two peaks show an opposite intensity ratio, responsible for the different shape of the corresponding first band. In the case of $Fe_4(dpm)_6$ the two peaks are clearly resolved, while in $Fe_4(pta)_6$ they result in a slightly asymmetric band. Indeed, in the first case the intensity ratio is unbalanced in favour of one of the two components (0.7 *vs* 0.5). The corresponding region of theoretical TDOS fairly reproduces the fine details found in the experimental curves. The DOS projected on carbon and oxygen atoms allow to understand that the different intensity ratio between peaks 1 and 1' is essentially due to the carbon PDOS, while the oxygen ones remain practically the same for both molecules.

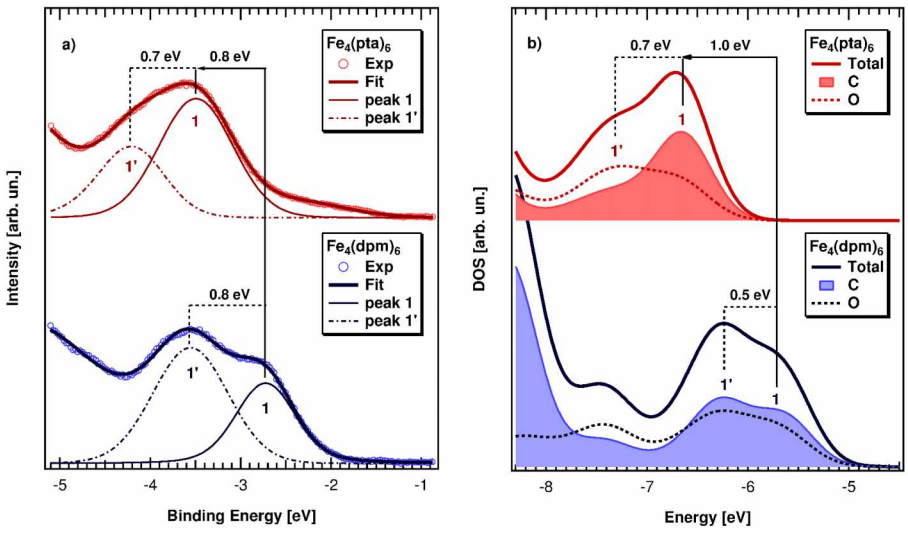

Figure 3.5: Enlarged view of region (i) of $Fe_4(dpm)_6$ and $Fe_4(pta)_6$ for both experimental (a) and theoretical (b) curves. Both curves are displayed with respect to their own energy scale. The experimental data (open circles) are reported along with the fitting curves (bold solid lines) and the corresponding main components (solid and dashed lines). The TDOS are reported together with the carbon and oxygen PDOS.

To have a better understanding, the contributions of the carbon PDOS for the different ligands are presented (see Figure 3.6). With reference to the first peak, we observe that the pta^- PDOS are shifted to lower energies of about 1.0 eV with respect to the

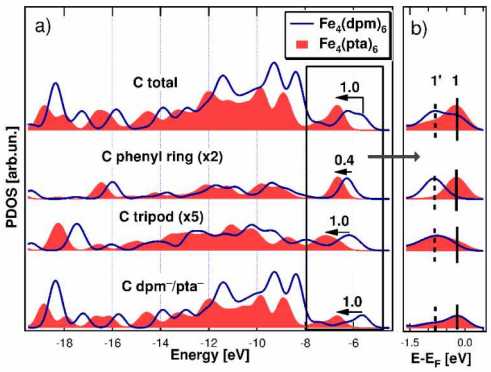

Figure 3.6: a) Carbon PDOS and relative ligand contribution. b) Enlarged view of the energy Fermi region with E_F set to 0 eV.

dpm^- ones. Since the states arising from F atoms are low-lying in energy, the DOS shape close to the Fermi energy is unchanged (see Figure 3.6b, where the DOS have been reported subtracting the molecule Fermi energy, E_F). The contribution of the tripodal ligand can be separated in two components – one coming from the phenyl ring and another one coming from the other carbon atoms, which is called tripod from now on. The latter maintains a shift similar to the PDOS of the dpm^-/pta^- one, while the former moves down in energy by only 0.4 eV. Therefore, the difference in the Fermi region can be ascribed mainly to the energy shift observed for the phenyl ring.

In the case of $Fe_4(dpm)_6$, the first band arising from C-phenyl overlaps with the C-tripod but not with the C-dpm^- one, while in $Fe_4(pta)_6$, the C-phenyl first band overlaps with the C-pta^- but not with the C-tripod one. Therefore, in both cases the peak with the highest intensity rises from the different energy position of the C-phenyl first band.

The overall effect of such relative energy shifts can be observed in the different electron density distribution for one molecular orbital, which is representative of peak 1 of each cluster. In $Fe_4(dpm)_6$ the molecular orbital is mainly localized on the dpm^- ligands, while in the $Fe_4(pta)_6$ it also involves the phenyl rings as it can be seen in Figure 3.7. The presence of phenyl orbitals close to the Fermi level of the molecule makes them ready for a bonding interaction with surfaces, suggesting that the $Fe_4(pta)_6$ could undergo a stronger adsorption process than $Fe_4(dpm)_6$. From Figure 3.7 the contribution of the d orbitals of Fe^c is also evident for both systems. Since one of the most appealing aspects of SMMs is the exploitation of their magnetic properties as quantum electronic devices, the possibility to modulate the easy-axis anisotropy (through gate or bias voltage) is, therefore, mandatory. In this regard, the combination of the phenyl and Fe^c d orbitals in peak 1 makes $Fe_4(pta)_6$ a more suitable spintronic candidate.[73]

In order to give further details about the electronic analysis of the Fe_4 systems we have also focused our attention on the most important electronic part of the clusters: the Fe $3d$ bands (Figure 3.8). As reported before, the substitution of the methyl groups with F atoms downshifts also the $3d$ band associated with the iron ions. However, this shift is not equivalent for the central iron ion and the peripheral ones. This difference is more evident if we plot the $3d$ bands shifted to the respective molecular Fermi energy. From this picture it comes out that the $3d$ bands of Fe^c in $Fe_4(dpm)_6$ result at lower energies than their corresponding ones in $Fe_4(pta)_6$. The opposite trend is observed for Fe^p, clearly showing the fluorination effect. The effect is small, as indeed expected, because of the indirect participation of F atoms in the metal-ligand bond. On the other

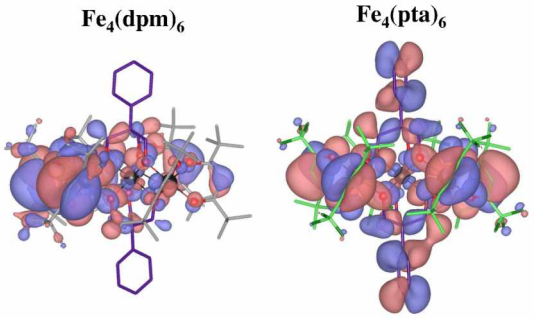

Figure 3.7: Representative molecular orbital for peak 1 of $Fe_4(dpm)_6$ and $Fe_4(pta)_6$ calculated at PBE0 level and visualized with VESTA,[74] contour cut-off 0.01.

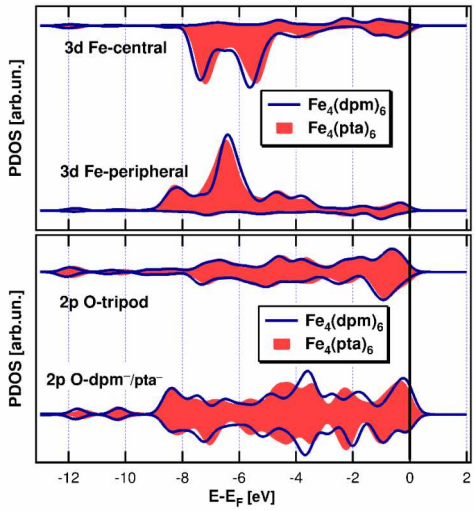

Figure 3.8: Spin-resolved PDOS of the core of the cluster. 3*d*-orbital contributions for the Fe^C and Fe^P (top graph) and oxygen 2*p* states in the different ligands (bottom graph)

hand, the upshift observed for Fe^c in $Fe_4(pta)_6$ can be explained by taking into account the lower steric hindrance with respect to the dpm^- ones. For this reason, the tripodal ligands can interact slightly stronger with Fe^c, shifting the 3*d* orbitals to higher energies. The lower steric hindrance of pta^- directly correlates with the smaller computed helical pitch angle, which stands for the average angle between the mean plane the four iron ions and the Fe_2O_2 planes involving the bridging alkoxides[56] (71.1 ° for $Fe_4(dpm)_6$, 69.3 ° for $Fe_4(pta)_6$): indeed, the $Fe_4(pta)_6$ shows a smaller easy axis anisotropy[57] as expected at both experimental[56] and computational levels.[55]

Few more words can be spent to describe the different band shape observed for Fe^c and Fe^p. First of all, it is worth mentioning that both complexes present the same energy PDOS profiles for the two kinds of iron ions. Their local coordination geometries can be considered as a distorted octahedron. In this framework, a t_{2g}–e_g band splitting is more evident for Fe^c than for Fe^p. Indeed, for the latter the picture is less clear due to the stronger distortions in the local octahedral environment, which lead to the removal of the degeneracy of nominal t_{2g} and e_g orbitals.

To be also stressed is the presence of minority spin states for both kinds of Fe in both systems due to spin delocalization effects through super-exchange interactions via O 2*p*

orbitals. Indeed, as a result of the mixing with the Fe $3d$, spin polarized asymmetric O $2p$ PDOS are observed and reported in the bottom panel of Figure 3.8. Moreover, a spin density reduction from the theoretical value of 5 for five unpaired electrons is observed: 4.37 for Fe^{c} in both clusters, and average values of 4.39 [$Fe_4(dpm)_6$] vs. 4.38 [$Fe_4(pta)_6$] for Fe^{p}. A larger spin delocalization towards the tripod oxygen atoms in the fluorinated version of the cluster is also observed (0.016 vs 0.029 e^-). The opposite trend is observed for the oxygen atoms in the dpm^-/pta^- ligands, where the value goes from 0.080 [$Fe_4(dpm)_6$] to 0.075 [$Fe_4(pta)_6$]. Such results can be also considered as a further support to the d-band analysis proposed above.

The thorough analysis of the electronic properties of $Fe_4(dpm)_6$ and $Fe_4(pta)_6$ confirms the reliability of the hybrid functional approach. However, its inapplicability on adsorbed systems encourages the use of the Hubbard-based approach - DFT+U.

3.4 Determination of the U parameter and DFT+U results

The DFT+U approach has been tested on both $Fe_4(dpm)_6$ and $Fe_4(pta)_6$ clusters. The U parameter stands for the difference between the on-site Coulomb and exchange interaction terms (see Section 2.2). It has been chosen to match the experimental photoemission spectra for the optimized revPBE structures of both clusters. The values for the different elements have been found by choosing selectively one or more characteristic bands related to their sets of orbitals.

In addition, good agreement with the magnetic properties is also required. The main exchange parameters have been estimated for the different U sets using the approach presented in section 2.5.2). An idealized trigonal symmetry was assumed to employ the same spin Hamiltonian used to fit the experimental magnetic data.[56,57]

Initially, the U parameter has been fitted on $Fe_4(dpm)_6$. First, the unpaired electron carriers, the Fe ions, have been considered. A value of 4.1 eV on the iron $3d$ orbitals is widely used for other iron-containing compounds.[67,75] Unfortunately, this U value does not give satisfactory results for the system. Unlike the Fe PDOS, which are very close in energy with respect to the Fermi level and in shape to the one calculated using the hybrid functional (Figure 3.9), the TDOS (Figure 3.10) does not reproduce well region (i). This region has significant contribution coming from the oxygen atoms, so the U parameter has been tuned on the O $2p$ states, keeping the U(Fe) equal to 4.1 eV. The more the U(O) value goes up, the better the agreement with experimental TDOS is. The best agreement has been achieved for U(O)=3.0 eV, where the two peaks in (i) region of the UPS spectrum are hinted.

On the other hand, the poor energy matching obtained with the experimental findings for region (iii) is to be ascribed to the orbital dependence of the on-site Coulomb corrections. Indeed, the region (iii) is mainly characterized by the presence of the C $2s$ states (see Figure 3.11). The application of U also on the C atoms ($2p$), which do not contribute directly to the magnetic interactions, brings along only some small improvements in the TDOS. Therefore, it has not been taken into consideration in the subsequent calculations.

As for $Fe_4(pta)_6$, the same U parameters on Fe and O have led to a fair reproduction of region (i) while region (ii) has been more problematic. There are states at about -3.5 eV with higher intensities which deteriorate the TDOS shape (see Figure 3.12). At those energies there are the fluorine $2p$ states, which are also affected by the U applied on the Fe (Figure 3.13). The tuning of the on-site parameter on the F $2p$ state results

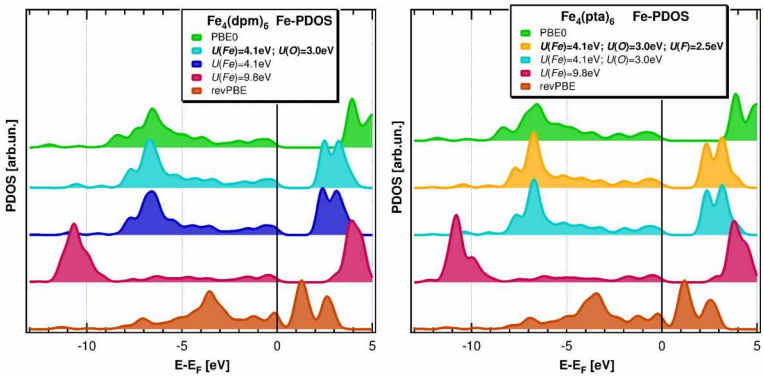

Figure 3.9: Fe-PDOS calculated at different levels of theory for $Fe_4(dpm)_6$ (left panel) $Fe_4(pta)_6$ (right panel).

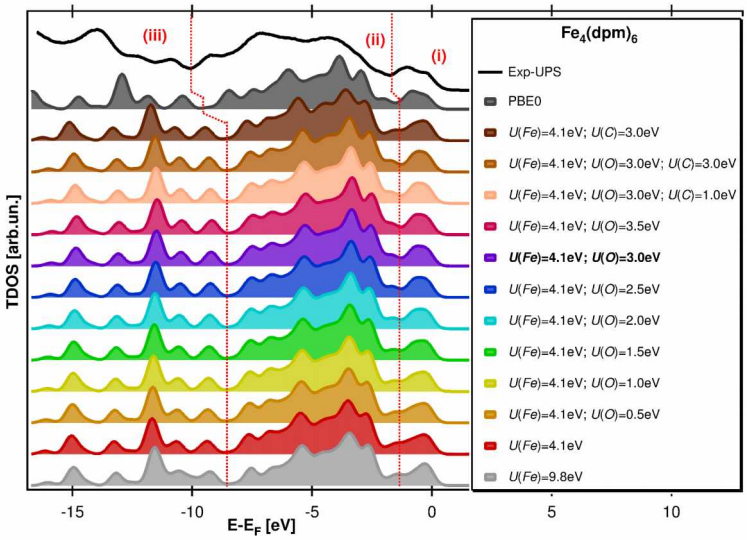

Figure 3.10: TDOS of the $Fe_4(dpm)_6$ cluster calculated with different U values

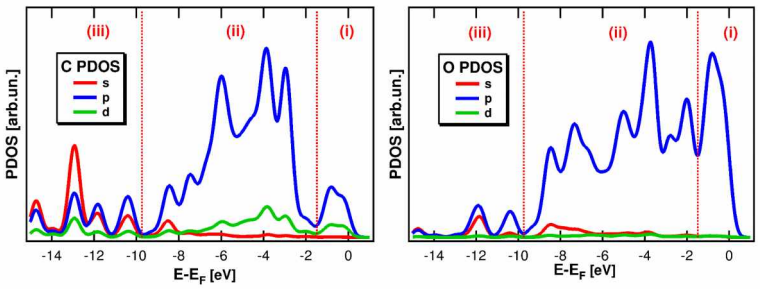

Figure 3.11: PDOS of the O (left) and C (right) for $Fe_4(dpm)_6$ cluster

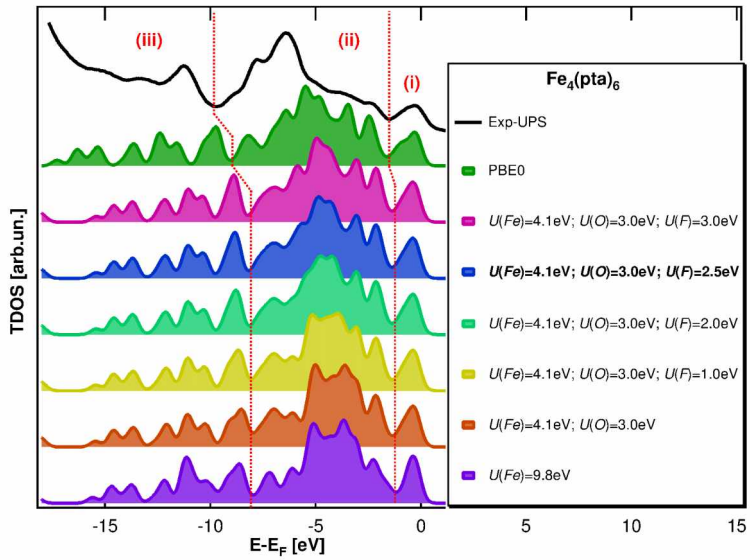

Figure 3.12: TDOS of the $Fe_4(pta)_6$ cluster calculated with different U values

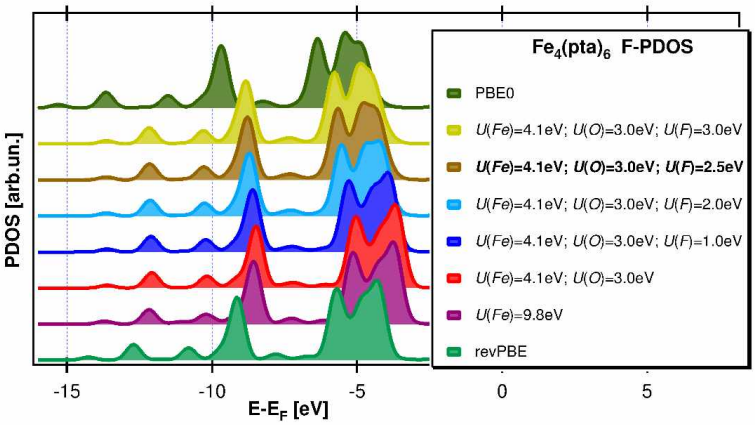

Figure 3.13: F-PDOS calculated at different levels of theory

in achieving the right intensity ratio of the first band and a TDOS very close to the experimental UPS spectrum with best agreement for U(F)=2.5 eV.

The revPBE+U approach shifts the filled spin states down to lower energies, while the opposite trend is observed for the empty spin states.[40,41] The shift is larger, as expected, for the d bands (see Figure 3.9). Therefore, since the first empty bands have a strong d character, this effect becomes also evident looking at the gaps (see Tables 3.2 and 3.3, and Figure 3.9). Dealing with high-spin d^5 ions, a small band gap even at revPBE level is observed. Instead, the calculated revPBE+U gap is closer to the much larger (and overestimated) PBE0 gap values.[76] The overall agreement between the revPBE+U approach and experimental UPS spectra is very satisfactory. A high reliability is, therefore, expected for this approach in the description of the Fe_4 SMM family electronic structure.

As far as magnetic properties are concerned, the computed exchange coupling constants with revPBE+U for both systems are reported in Tables 3.4 and 3.5, together with the PBE0 and experimental ones. In the case of $Fe_4(dpm)_6$, values for the exchange

Table 3.2: LUMO-HOMO gaps calculated upon variation of U for the $Fe_4(dpm)_6$ cluster

U(Fe) (eV)	U(O) (eV)	U(C) (eV)	Gap (eV)
9.8	-	-	3.06
4.1	-	-	2.28
	0.5	-	2.30
	1.0	-	2.31
	1.5	-	2.33
	2.0	-	2.35
	2.5	-	2.36
	3.0	-	2.38
	3.5	-	2.40
	3.0	1.0	2.39
	3.0	3.0	2.42
	-	3.0	2.31
	PBE0		3.75
	revPBE		0.99

Table 3.3: LUMO-HOMO gaps calculated upon variation of U for the $Fe_4(pta)_6$ cluster

U(Fe) (eV)	U(O) (eV)	U(F) (eV)	Gap (eV)
4.1	3.0	2.26	
		1.0	2.26
		2.0	2.25
		2.5	2.24
		3.0	2.24
	PBE0		3.75
	revPBE		0.89

Table 3.4: Results for the exchange coupling constants calculated by revPBE + U for different values of the U parameter on the X-ray and optimized structure of the $Fe_4(dpm)_6$ cluster

U(Fe) (eV)	U(O) (eV)	U(C) (eV)	J_1 (cm^{-1})	J_2 (cm^{-1})	J_1 (cm^{-1})	J_2 (cm^{-1})
			Optimized		X-ray	
9.8	-	-	17.66	-	-	-
	-	-	31.68	-	32.59	-
	0.5	-	28.86	-	-	-
	1.0	-	26.18	-	-	-
	1.5	-	23.62	-	-	-
	2.0	-	21.20	-	-	-
4.1	2.5	-	18.89	-	-	-
	3.0	-	16.70	0.25	16.95	0.38
	3.5	-	14.63	-	14.79	-
	3.0	1.0	16.59	-	-	-
	3.0	3.0	16.37	-	-	-
	-	3.0	31.26	-	-	-
PBE0			13.83	0.16	14.43	0.27
Experimental[56]			16.37(12)	0.29(11)		

Table 3.5: Results for the exchange coupling constants calculated by revPBE + U for different values of the U parameter on the X-ray and optimized structure of the $Fe_4(pta)_6$ cluster

U(Fe) (eV)	U(O) (eV)	U(F) (eV)	J_1 (cm^{-1})	J_2 (cm^{-1})
			Optimized	
		-	15.18	-
		1.0	15.20	-
4.1	3.0	2.0	15.24	-
		2.5	15.28	0.34
		3.0	15.30	-
PBE0			13.39	1.58
Experimental[57]			16.20(6)	0.53(4)

constants calculated on the basis of the X-ray structure[56] are reported as well, in order to evaluate the changes induced upon structural optimization. Such a comparison is not possible for $Fe_4(pta)_6$ due to the lack of X-ray experimental structure. The overall very good agreement between the experimental and computed revPBE+U results, however, could not be taken for granted a priori. Indeed, the agreement comes from the ad hoc choice of the U values for the different elements made on the basis of the photoemission spectra. This result is, therefore, a confirmation that in SMM-like systems, where the magnetic interactions mainly propagate through super-exchange interactions involving the ligands, a properly tuned set of U values for all the atoms involved into the super-exchange mechanism is needed.[77,78] In this framework, the inclusion of the U(O) for a correct description of the electronic and, above all, of the magnetic properties of the systems under study finds its justification in the necessity to accurately tune the amount of delocalization of the electronic densities of the bridging ligands involved in the super-exchange paths. This proves that the doubling of the U on Fe to 9.8 eV gives good results for the magnetic interaction but for the wrong reasons.

It is worthy of notice that the nearest-neighbour exchange coupling constants, U, computed at revPBE+U level, are in better agreement with the experimental ones than those obtained with PBE0. The trend of having a stronger antiferromagnetic interaction in the X-ray structure with respect to the optimized $Fe_4(dpm)_6$ is maintained both at PBE0 and revPBE+U level of theory. In the case of $Fe_4(pta)_6$, the J_1 values obtained with U are both lower than the experimental ones. Regarding the J_2 values, the computed revPBE+U ones are in good agreement with the experiment and, for $Fe_4(pta)_6$, the improvement with respect to the PBE0 values is significant. Larger J_1 and J_2 values for $Fe_4(dpm)_6$ than $Fe_4(pta)_6$ have been properly reproduced, indicating that the revPBE+U approach is sensitive enough to slight differences in the Fe_4 SMM core region. Moreover, the reliability of reproducing the electronic and magnetic features for both systems here studied makes the well-tuned revPBE+U approach suitable for a characterization in silico of adsorbed Fe_4 species on surfaces. It should be stressed out that such approach can be used in adsorbed scenarios only in the presence of slight deformations of the Fe_4 core at least as small as the ones observed passing from $Fe_4(dpm)_6$ to $Fe_4(pta)_6$.

Table 3.6: Spin densities for the four Fe-ions, calculated with the different methods on $Fe_4(dpm)_6$ and $Fe_4(pta)_6$.

$Fe_4(dpm)_6$			**$Fe_4(pta)_6$**	
PBE0	**revPBE+U**	**Atoms**	**PBE0**	**revPBE+U**
-4.37	-4.36	Fe^c	-4.37	-4.37
4.39	4.38	Fe^p	4.38	-4.37
0.016	0.016	O^{tri}	0.029	0.029
0.080	0.080	O^{dpm^-/pta^-}	0.075	0.074

In conclusion, the properties of $Fe_4(dpm)_6$ and $Fe_4(pta)_6$ have been studied at two levels of theory. An overall good agreement has been obtained between the computed PBE0 DOS and the experimental data. The same, since one of the most striking and appealing applications of SMMs is the possibility of adsorbing them on surfaces, a revPBE+U parameterization has also been performed. The correct trend in magnetic interactions and the reproduction of the peculiar features of electronic spectra for both systems has been achieved with a set of U parameters on Fe 3d, O 2p and F 2p, fitted on the electronic and magnetic properties of both clusters. The theoretical approach presented here represents a striking advantage in the overall characterization of such complex systems, allowing the reliable description of their structural and electronic/magnetic properties both in the bulk and when deposited on surfaces.

CHAPTER
FOUR

SURFACES

Surfaces are very important in various fields, such as catalysis and materials science. Lately, they have been used in electronics and spintronics as electrodes in nanojunctions and also for adsorption studies of different molecules. In order to study such systems at a theoretical level, a reliable reproduction of the properties of the surfaces is needed.

Modelling and simulating surfaces can be a tricky and challenging experience, as there are many things to be taken into consideration beforehand, such as periodicity, slab thickness, termination layer etc. One of the reasons to study surfaces is their use in investigation of adsorption processes. There are two theoretical models that describe adsorbed systems - the cluster and the slab model. The cluster model consists of a surface with a limited number of atoms, no periodicity, and it relies on the idea that the surface atoms farther from the adsorbate are not important. Another way to describe surfaces is by using a slab with a certain periodicity. When working with plane-wave basis sets, the slab is placed in a simulation cell where the periodicity is imposed in the three directions. Usually, in the case of a full periodic simulation cell along x, y, z, a sufficiently big vacuum space is introduced in the direction perpendicular to the slab, which serves as a decoupling layer from the periodic image of the surface along that direction. If periodicity is not wanted in one direction, a decoupling along that direction could be introduced with different computational schemes (such as Martyna-Tuckerman,[79] wavelet[80,81]), for which, however, a very big vacuum region is required. In this study, slabs in full periodic simulations cells are used, since these models are needed for subsequent adsorption studies.

Another important issue when modelling a surface is the thickness of the slab. The ideal case would be a slab where the bottom layers reproduce the bulk properties, while the topmost ones - the ones of the surface. Usually, when working with rather large slabs, a compromise between computational cost and accuracy is required.

Last but not least comes the problem with the termination layer. It arises for complex unit cells, in oxide surfaces for instance, where there are more than one possible termination layers. There are two ways to deal with such a surface 1) to use an asymmetric slab and 2) to use a symmetric slab (see Figure 4.1). If the different layers are not charged equally, the first case would be ideal as it guarantees electro-neutrality. However, in the same time such choice would make it more difficult to calculate the surface energy and work function of the system, since both terminations are presented. Moreover, it would create an artificial surface dipole through the slab, which would need a further correction[82] (see *Surface dipole and dipole correction* section below). While these prob-

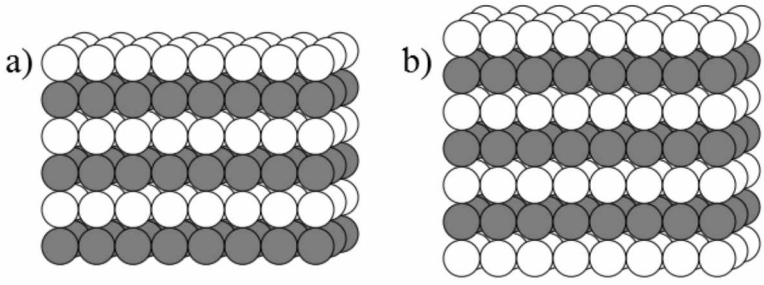

Figure 4.1: The two possible types of slabs are presented - a) asymmetrical, b) symmetrical

lems are not present in the second case, the disadvantage of using a symmetric slab is that the system would be charged. In order to avoid this, defects and/or vacancies are introduced.

There are several ways to estimate the stability of a surface and whether it reproduces the experimental results. One way is by comparison of the DOS with the electronic states obtained by angle-resolved photoemission spectroscopy and STM, which guarantees the probing of surface states only. Other ways are to check the surface energies and work functions of the models. These two approaches will be discussed separately and in a more detailed way below.

Surface energy

The surface energy, is the energy necessary to create a surface per unit area. It is an indicator of the stability of the surfaces. Experimentally, the surface energy is obtained by surface tension measurements made in the liquid phase and extrapolated to zero temperature.[83] Since the experimental values are difficult to get, an accurate theoretical method for the estimation of the surface energy is indispensable. The standard formula is the following:

$$E_{surf} = \frac{1}{2}\frac{(E_{slab} - NE_{bulk})}{A_{surf}} \tag{4.1}$$

where E_{slab} is the energy of the slab, E_{bulk} is the energy of the bulk model, and A_{surf} is the surface area. The parameter $\frac{1}{2}$ stands for the fact that when working with slabs separated from each other by vacuum, inevitably two equivalent layers of surface are created.

This formula, however, is strongly dependent on the way the bulk energy is calculated and the number of layers used. Boettger states that when E_{bulk} is obtained independently, the calculated surface energy deteriorates with increasing the thickness of the slab.[84] He proposes to determine the surface energy only by considering slabs calculations:

$$E_{surf} = \frac{1}{2}\frac{(E^N_{slab} - N\Delta E_N)}{A_{surf}} \tag{4.2}$$

where $\Delta E_N = E^N_{slab} - E^{N-1}_{slab}$ avoids the separate calculation of bulk energies and, thus, there are no divergence problems.

Another method is presented with equation 4.3. The E_{bulk} is obtained from a calculation where the supercell contains the slab and the vacuum is filled with layers. In

order to take account for the different number of atoms, the factor $\frac{N_{slab}}{N_{bulk}}$ is introduced.[85] This method, however, is not practical for very big slabs, where a large vacuum region is considered, due to the computational cost.

$$E_{surf} = \frac{1}{2}\frac{(E^{N}_{slab} - E^{N_B}_{bulk}\frac{N_{slab}}{N_{bulk}})}{A_{surf}} \tag{4.3}$$

Fiorentini and Methfessel suggest to plot the total energies for slabs with different thickness *vs.* the number of layers and to extract E_{bulk} from the slope.[86] In comparison with all methods stated above, the last one results in faster convergence to the correct surface energy. The drawback is that thin slabs are to be avoided, if an accurate value is required.

Work function

Another important characteristic in the surface science is the work function of the surface, which measures the work needed to move an electron from the surface to the vacuum at 0 K. It is calculated according to the following equation:

$$\Phi = V(\infty) - E_F \tag{4.4}$$

where the $V(\infty)$ is the electrostatic potential in the vacuum region and E_F is the Fermi level of the material. For temperatures of 0 K, the work function is the chemical potential, μ. The work function is very useful when studying adsorption. The adsorbed molecules alter the work function of the surface, thus giving important information about the bonding, charge transfer, etc. The electronegative adsorbates increase the work function of the surface, rendering $\Delta\Phi$ positive.

Surface dipole and dipole correction

When working with asymmetric slabs, the periodic boundary conditions give rise to an artificial surface dipole in the simulation cell. It is measured as the difference between the electrostatic potential near the surface, which is the result of the different surface terminations. Bengstson has derived a correction for the dipole field that corrects the potential and the total energy of the system.[82] The dipole correction term introduces a jump in the Hartree potential of the simulation cell, where the discontinuity is placed within the vacuum region. In this way, it is easier to identify the vacuum levels and thus determine the work function of the surface. Such a correction also affects the total energy of the system.

In the present thesis, three surfaces have been studied. The first one is the conducting Au(111). It is well-known and widely used for different deposition processes. The second one is CuN - where above the conducting Cu(100), there is an insulating layer of N atoms at (2×2) positions. It is highly used when a decoupling from the conducting surface is needed in order to study the properties of the molecule itself upon deposition. The last surface to be studied is the $La_{1-x}Sr_xMnO_3$ (LSMO) - a magnetic doped oxide surface. Due to a variety of physical properties, it is highly used in spintronics for different magnetic devices.[11,12,87]

The aim of the surface studies is to present models for all three surfaces, able to reproduce the characteristic structural, electronic, and magnetic (where present) properties of each system. Later, these substrates will be used to study the behaviour and properties of the $Fe_4(dpm)_6$ cluster on each of them. In addition, these models will test the used computational protocol.

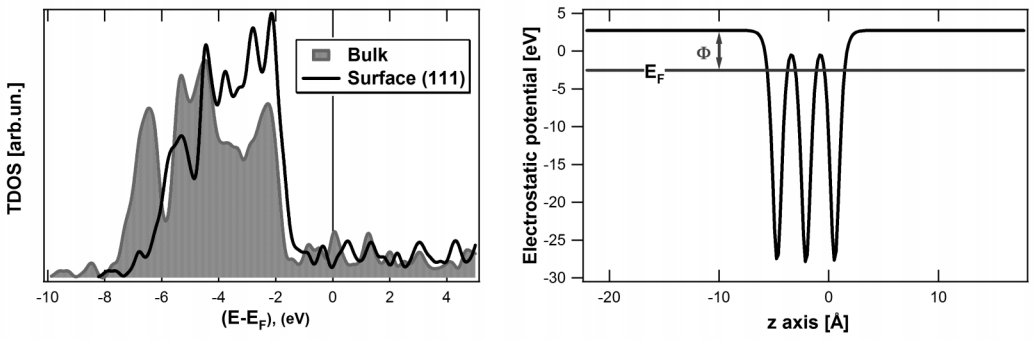

Figure 4.2: On the left are presented the TDOS of the bulk compared with those of the surface; both have been aligned to their own Fermi level; the Gaussian width, σ, is 0.2 eV. On the right, the electrostatic potential of the surface.

4.1 Au(111)

The Au(111) surface is widely used due to its conducting properties (for instance STM, nanojunctions, electrodes).[73,88,89] In this work it is to be used for studies on the adsorption of one Fe_4-cluster. Therefore, the dimensions of the slab have been chosen correspondingly. The dimensions of the surface simulation cell are $(23.09 \times 24.98 \times 40.00)\,\text{Å}^3$. The xy plane is considered large enough to host one Fe_4-cluster, leaving enough space (*ca.* 10 Å) between the molecule and its periodic image. The vacuum zone along z is about 35 Å, which would guarantee the decoupling with its periodic image.

The model slab consists of three layers of 80 atoms each, for a total of 240 gold atoms. Several other studies have used the same thickness of Au(111) slabs for adsorption.[24,90,91] Indeed, Rajaraman et al. used a three-layer model for their study of thiols on gold surface.[91] They calculated the enthalpy of formation of an adatom and a vacancy on the surface (effects which increase the stability between the surface and the adsorbed molecules) on multiple layer slabs. The errors coming from the three-layer model with respect to the five-layer one were considered modest, so the authors concluded that there was more computational gain in the former case.

The distance Au-Au has been chosen to be the experimental one 2.885 Å. During the geometry optimization, the atomic positions of the bottom atomic layer were kept fixed to the experimental distances in order to reproduce a bulk-like behaviour, whereas the other two layers have been left to relax. The characteristic herringbone structure of the Au(111) surface, which appears with a periodicity of 63 Å,[92] has not been taken into consideration since the size of the simulation cell is not large enough to reproduce it properly. However, the properties of the adsorbed molecules are still expected to be reproduced in a proper way.

All calculations have been performed with the revPBE functional.[31] The Norm-conserving Goedecker-Teter-Hutter (GTH) pseudopotential,[28,70] which considers explicitly 11 valence electrons, has been used together with a GTH double-ζ polarized molecularly optimized basis set.[71] An energy cut-off of 400 Ry has been applied to the plane-wave basis set.

The convergence criteria have been fixed at 1×10^{-6} Hartree for the SCF energy and 1×10^{-3} HartreeBohr^{-1} for the atomic forces during the geometry optimization. Working with a metallic surface necessitates the smearing of the occupational numbers around the Fermi level. The Fermi-Dirac distribution has been used with a broadening (electronic

Table 4.1: Interlayer separation along z of the Au(111) surface

Δ z(layers) (Å)	Au(111)
(top-middle)	2.624
(middle-bottom)	2.623
Experimental	2.350

temperature) of 1500 K.

The optimization of the surface structure has led to an increase in the interlayer separation along z of about 11% (see Table 4.1). Such high value is a result of the relaxation of the surface geometry. It compensates for the bond breaking and redistribution of charges in the slab with respect to the bulk phase.

The TDOS for the surface and bulk are presented in Figure 4.2 (left). There is a noticeable shift of the low-lying states until -3 eV due to a contraction of the surface states. The overall shape is maintained, however, the intensity ratio between some of the peaks is changed. At the Fermi level region, the density is strongly reduced.

In order to test the reliability of the model, the work function for this Au surface is calculated (see Figure 4.2 (right)). The value of 5.27 eV that has been found is in agreement with the experimental values of 5.26 ± 0.04 eV[93] and 5.35 eV.[94]

Having these results in mind, it can be concluded that the three-layer Au(111) slab is a reliable model for a gold surface.

4.2 CuN

When a molecule is deposited directly on a conducting surface, changes inevitably occur, such as coupling with the underlying surface electronic states. However, adsorption on an insulating layer above the conducting surface reduces these changes, permitting thus to see the molecular states, similar to the free molecule.[95] Such technique is very useful in case of doubts about the integrity of the molecules after deposition. One surface of this type is CuN, a Cu(100) surface on which lies a monoatomic layer of N atoms.

The atomic structure of the CuN surface has been widely discussed in literature. One of the first Low-Energy Electron Diffraction (LEED) studies shows that the nitrogen atoms adsorb at the fourfold hollow sites of the Cu surface $c(2\times2)$.[96,97] The adsorbed N atoms form islands with roughly square shape with dimensions 5×5 nm^2, separated from one another by patches of clean Cu(100) surface at submonolayer coverages.[98] When a full monolayer of N atoms is deposited, the islands merge and Cu trenches appear. This is considered a way to release the stress, accumulated upon the formation of the Cu_2N, due to the mismatch with the copper lattice constant.[99] Indeed, in an STM-based study Choi *et al.*[100] confirm that the lattice constant of Cu_2N, 3.72±0.01Å, is smaller than the correspondent bulk Cu_3N (3.81Å) and yet bigger than the one for the Cu lattice (3.61Å).

A lot of attention has been given also to the STM images obtained for the CuN surface. All studies confirm the presence of protrusions, but their origin has divided the opinions. Leibsle *et al.*[99] consider them to be N-atoms, Driver and Woodruff[101] suggest they are Cu atoms, and Hirjibehedin *et al.*[102] believe them to be the hollow sites in the last copper layer. Choi *et al.*[100] reconciles all views by stating that the origin of the protrusions depends on the bias applied for the STM experiment. The depressions at positive voltages are assigned to the N atoms, which become protrusions at negative bias. The latter result is reproduced by theoretical calculations.[103,104] However, the N-atoms seen as depression is not confirmed by the theory.

Many efforts have been put in the atomic reconstruction of the surface. Generally, it is believed that the nitrogen atoms are almost coplanar to the topmost copper layer. However, there are also several other models based on experimental studies, which have been tested theoretically. One of them is the rumpled structure, proposed as a result of photoelectron diffraction measurements[105] and STM experiments.[101] It is a symmetry-lowering rumpling of 0.34 Å of the outermost Cu layer, where one of the Cu atoms in the $c(2\times2)$ unit cell moves upwards, and the other one - downwards. This model has been tested by Yoshimoto and Tsuneyuki,[103] Hong et al.,[106] Tao et al.,[107] and in all cases, after optimization, the structure returns to the unrumpled case. Another model is the clock reconstruction model, based on LEED experiments,[108] where the Cu atoms of the topmost layer shift clockwise or counter-clockwise, while the N atoms remain in $c(2\times2)$ positions. The simulated model has resulted unstable and after optimization has again returned to the undistorted structure.[106] Tao et al.[107] have tested also a structure where the N atoms are adsorbed at the atop site, which is, however, a very implausible solution due to lack of dynamical stability. All theoretical studies confirm as most stable one the case where the nitrogen atoms lie slightly above the top copper layer, therefore, this is also the model studied in this thesis.

In the present work, the CuN surface is studied using two functionals - revPBE[31] and PBEsol.[32] The parameters for the D3 correction are revPBE and PBE (due to the lack of parameters for PBEsol), respectively. Also for this system, norm-conserving GTH pseudopotentials are used,[28,70] where 5 and 11 electrons are assumed for N and Cu, respectively. The basis sets are double-ζ polarized and molecularly optimized for both

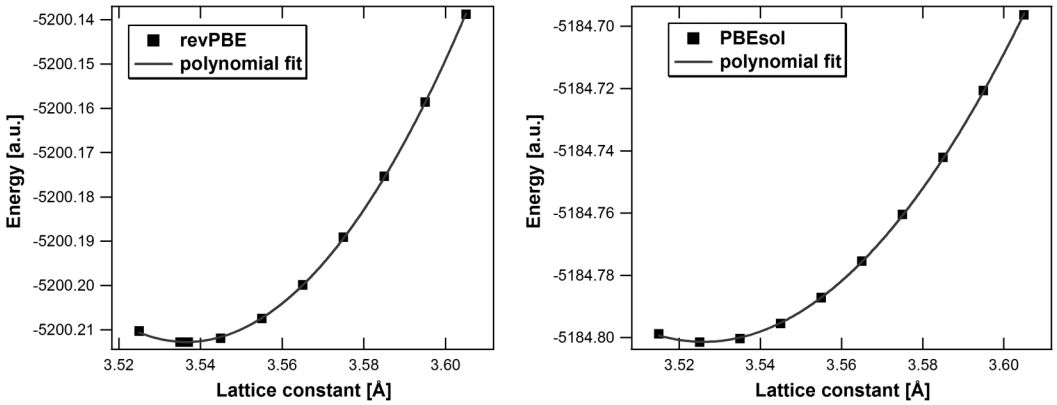

Figure 4.3: Minimum for the lattice constant of Cu bulk, obtained with revPBE (left) and PBEsol (right)

Table 4.2: Lattice constants for the CuN surface, optimized on bulk of Cu(100).

Functional	**Lattice constant (Å)**
revPBE	3.537
PBEsol	3.527
Experimental[110]	3.615

atomic kinds.[71] In agreement with the study of Gomez Diaz et al.,[109] the plane-wave cut-off is set to 500 Ry. In all optimizations of the geometry, the convergence criteria for the SCF energy has been fixed at 1×10^{-6} Hartree and 1×10^{-4} HartreeBohr^{-1} for the atomic forces. The electronic temperature for the Fermi-Dirac ditribution has been set to 300 K.

First, the lattice constant of the bulk copper for both exchange-correlation functionals needs to be determined. Single-point calculations have been performed over different values of the lattice constant. The model that is used for the bulk phase consists of $3\times3\times3$ the Cu(100) unit cell. The results are presented in Figure 4.3 and Table 4.2. The two functionals give relatively close lattice constants and both values are lower than the experimental one by about 2%. As it can be seen in Gomez Diaz *et al.*,[109] a possible explanation can be sought in the use of the D3 parametrization. Their study on the bulk of Cu(100) with revPBE functional showed that the inclusion of the D, and D2 dispersion corrections leads to smaller lattice constants.

In the next step, Cu and CuN surfaces are constructed with the optimum lattice constants for the two functionals found from the Cu(100) bulk calculations. The slabs consist of $8\times8\times2$ unit cells of copper (100) or a total of 512 atoms distributed in 4 atomic layers of Cu. In the case of the CuN, the nitrogen atoms are positioned according to the $c(2\times2)$ pattern, for total of 64 N atoms. The geometry optimization of both Cu and CuN surfaces has been started from the bulk positions of the Cu atoms. Initially, the nitrogen atoms are at 0.3 Å above the plane of the topmost copper layer in agreement with the experimental findings. The simulation cells are with the following dimensions: $(28.296\times28.296\times60.000)$ Å^3 for the revPBE and $(28.216\times28.216\times60.000)$ Å^3 for the PBEsol. Like in the case of the Au surface, the size of the cell in the xy directions is chosen with the idea to fit an $Fe_4(dpm)_6$ in it and the vacuum region is large enough to decouple the periodic image of the slab along z. In all cases, the bottom two atomic

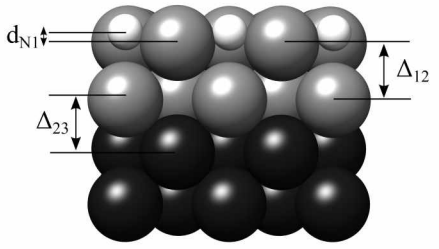

Figure 4.4: A schematic representation of the distances presented in Tables 4.3 and 4.4. The white atoms are nitrogens, the light grey are copper atoms left to relax, and the deep grey are the Cu atoms that are kept fixed to the bulk bond distances.

Table 4.3: Change in the interlayer distances in % for the optimized Cu surface obtained via different functionals.

	Functional	Δ_{12} (%)[a]	Δ_{23} (%)
Cu surface	revPBE	3.49	3.30
	PBEsol	−0.50	2.13

[a] Δ_{ij} are computed as the difference between the height of layers i and j with respect to the bulk value, divided by the latter.

layers of Cu has been kept fixed to the bulk position during the geometry optimization.

The geometry optimization has led to several changes on the surfaces, which are measured according to the parameters in Figure 4.4.

In agreement with the study of the Au(111), the interlayer distances between the top three layers has increased slightly for the revPBE, although not so significantly as for the gold surface. Such difference could be ascribed to the different packing of the two slabs or the different D3 correction that has been used. The results with PBEsol, however, differ from those of revPBE. The Cu^{top-1} layer has separated more from its underlying layer than the topmost, Cu^{top}, which is closer to the bulk value.

The situation with the interlayer distances changes when the N atoms are deposited. The topmost layer for both functionals tend to separate from the underlying one (see Table 4.4). However, the nitrogen atoms have different behaviour for revPBE and PBEsol. While the average values for the displacement of the N atoms are in good agreement with other theoretical and experimental studies, a close look reveals different behaviour. For the revPBE, the N atoms tend to be in a wave-like positions, where one nitrogen moves in between the adjacent Cu atoms, and the neighbouring N atoms are pushed up. This can be clearly seen in Table 4.5 which presents the average position along z with its standard deviation. Such behaviour has not been observed in other theoretical studies and it is not reproduced by the PBEsol, where the N atoms are at almost the same height and slightly above the topmost layer of copper atoms. A possible explanation is that for the revPBE the mismatch between the lattice constants of Cu and Cu_3N plays a major role and leads to such geometrical solution in order to release the surface stress.

The PBEsol, however, does not reproduce correctly the charges distribution. The average Mulliken charge on the nitrogen atoms is positive, unlike the revPBE results and other theoretical studies obtained with Bader analysis.[115,116]

The differences in the DOS between the Cu and CuN surfaces are mainly reproduced

Table 4.4: Geometry of the CuN surface obtained with different methods.

	Method	$dN1$ (Å)	Δ_{12} (%)	Δ_{23} (%)
Experiment	SEXAFS[a] [111]	0.40	4.7	0.3
	Helium-ion channelling [112]	-	15.0	3.0
	X-ray diffraction and molecular dynamics [113]	-	14.0	1.5
	Grazing incidence X-ray diffraction [114]	0.15	14.0	1 \5
Theory	GGA(PBE) [103]	0.21	7.7	0.5
	GGA(PBE) [107]	0.20	9.1	0.9
	GGA(PBE) [106]	0.17	7.8	0.2
This study	revPBE	0.34	10.9	1.2
	PBEsol	0.36	7.5	1.7

[a] Surface extended X-ray absorption fine structure

Table 4.5: Average shift of the corresponding atoms along z (Å) with the error for the optimized Cu(100) and CuN surfaces for the different functionals.

surface	Atomic layer	revPBE	PBEsol
Cu	Cu^{top}	5.427±0.025	5.319±0.000
	Cu^{top-1}	3.596±0.002	3.565±0.019
CuN	N	5.864±0.295	5.810±0.000
	Cu^{top}	5.521±0.009	5.452±0.000
	Cu^{top-1}	3.560±0.037	3.556±0.019

Table 4.6: Mulliken charges for CuN surfaces with the two functionals

Atomic layer	revPBE	PBEsol
N	−0.093	0.011
Cu^{top}	0.017	−0.029
Cu^{top-1}	0.024	0.019

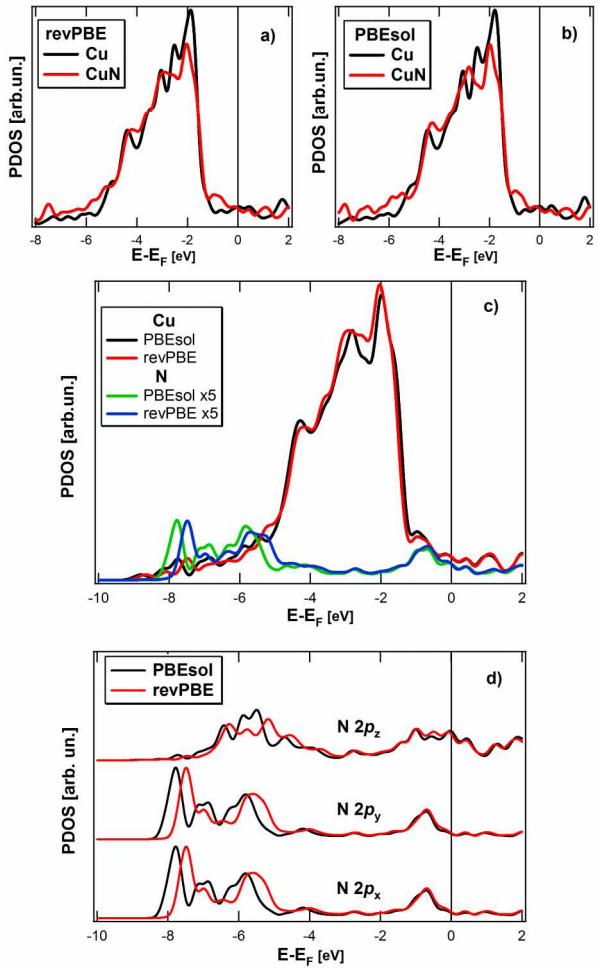

Figure 4.5: Comparison between the PDOS calculated with the two functionals. The N PDOS have been multiplied by 5, in order to be visible; the used Gaussian width, σ, is 0.2 eV.

with the two functionals (see Figure 4.5a and 4.5b). Even though the shape of the DOS in the region -5 ÷ -1 eV is maintained, in the case of CuN, the peaks are with reduced intensity. Moreover, the peak at -3 eV disappears and a shoulder at -2 eV appears. As a result of the N presence, two major changes occur. A peak appears at -1 eV, clearly seen for both functionals. The second one with higher intensity is in the region -8 ÷ -5 eV and there is the main discrepancy between the functionals as shown in Figure 4.5d. The nitrogen PDOS for $2p_x$ and $2p_y$ are identical and the only difference comes from a shift of the PBSsol ones of 0.3 eV to lower energies. On the other hand, the $2p_z$ remain at the same energies, but with different intensities. Since the nitrogen atoms are not positioned in the same way in the two CuN surfaces, they couple differently with the Cu states. Similar DOS for the CuN surfaces have been obtained also by other theoretical studies.[107,117]

Major differences between the two functionals are observed also in the simulated STM images. In the case of PBEsol, all Cu atoms appear to be protrusions, while the N ones remain mainly as depressions at both biases, which is at odds with other theoretical studies, where the nitrogen atoms are observed as protrusions.[103] On the other hand, in the case of revPBE, the STM image is more irregular. Some of the N are seen as

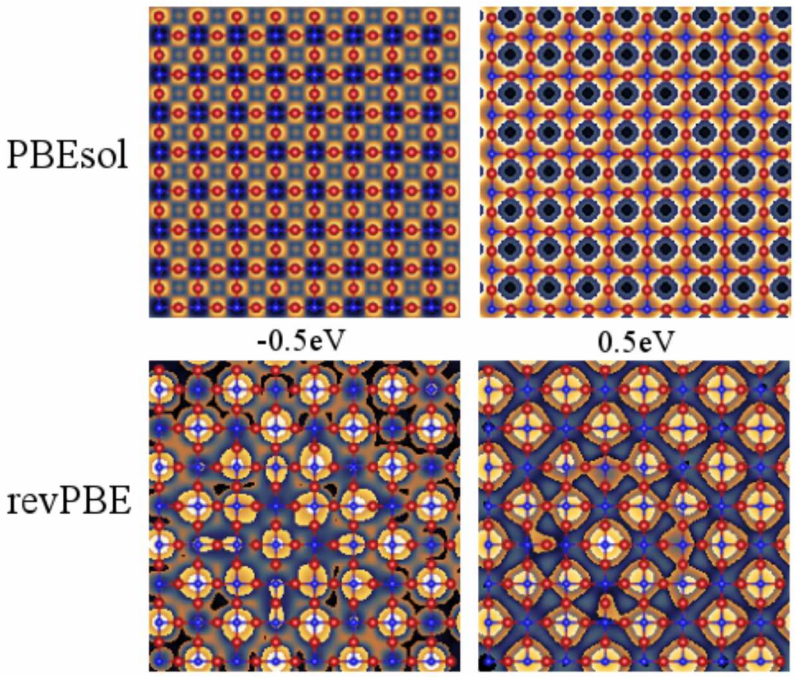

Figure 4.6: Simulated STM images for the PBEsol (top row) and revPBE (bottom row) for occupied states (left column) and empty states (right column); the N atoms are in blue and the Cu ones - in red.

depressions, while others - as protrusions. Such discrepancy is due to their different height with respect to the copper layer.

In order to test the validity of our model, the work functions for both Cu and CuN have been estimated. In the former case the values are 4.76 eV for PBEsol and 4.36 eV for revPBE. The experimental one ranges from 4.59 to 4.83 eV.[118,119] When the N atoms are added, the shape of the potential changes and a surface dipole appears, due to the different termination layers in the slab.(see Figure 4.7) After an applied correction for the surface dipole, the values for the $\Delta\Phi$ are 0.41 eV for PBEsol and 0.55 eV for revPBE. Both values are lower than the experimental one of 0.9 eV.[120]

In conclusion, revPBE functional fails to reproduce the geometry of the surface, while PBEsol does not give satisfactory results regarding the charges. Different STM images with respect to the experimental ones are obtained with both functional. However, the work function is reproduced in the two cases. In order to be in agreement with the experiment, the geometry obtained with the PBEsol is used for the adsorption studies.

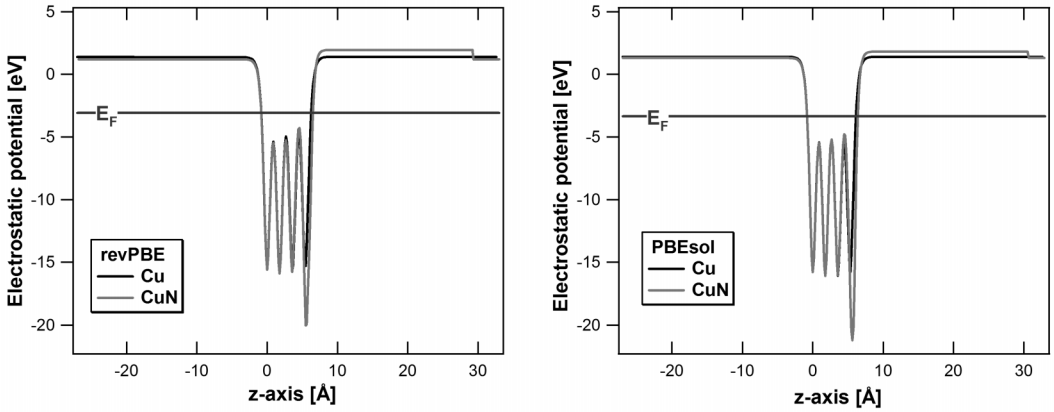

Figure 4.7: The electrostatic potential for the surfaces Cu (black) and CuN (grey) obtained with revPBE (left) and PBEsol (right)

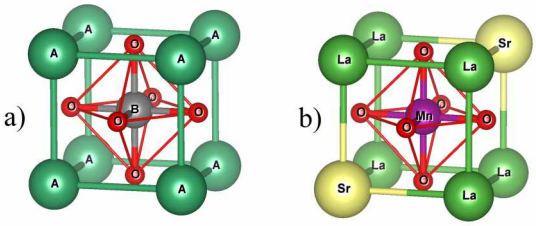

Figure 4.8: The pseudocubic unit cell of the not doped perovskites crystals (a) and the one of $La_{0.67}Sr_{0.33}MnO_3$ (b).

4.3 LSMO

Another material that has been extensively studied at theoretical and experimental level are the doped perovskite manganites. They are known for the variety of properties they possess such as spin polarization at Fermi level, electron transport, colossal magnetoresistance, and ferromagnetic phase transitions, which make them perfect for current injection in spintronic devices,[1] such as magnetic tunneling junctions.[121]

The perovskites represent a group of compounds with a general formula ABO_3, which have similar lattice structure based on double mixed oxides (see Figure 4.8). The unit cell contains two types of metal ions. The A metals are positioned at the edges of the unit cell and they are rare-earth or alkaline earth metals. The metal B is body-centered and it is a transition metal. The oxygen ions are face-centered and they form bonds with B, giving thus rise to an octahedral environment. In the perfect perovskite crystal the radius of A-type is larger than the radius of the B-type metal $r_A > r_B$. Moreover, the B-O-B angle is 180° and the B-O bonds are equally long.

When the B metal is Mn, the compounds are called perovskite manganites. An example of a manganite is $LaMnO_3$ (LMO). The Mn have a non-zero magnetic moment and the LMO is found to be an antiferromagnetic insulator. When the LMO crystal is hole-doped, *i.e.* some of the La cations are substituted with bivalent cations, insulator-metal transition takes place.[122] One of the most famous compounds with such structure is the $La_{1-x}Sr_xMnO_3$ (LSMO), where x indicates the doping level. The doping introduces Mn^{4+}, which plays an important role in the magnetic interactions ad gives rise to a variety of physical properties.

Urushibara et al.[123] have studied LSMO for doping levels between 0 and 0.6 (see Figure 4.9). At low temperatures and low x, the LSMO is an insulator. However, by increasing the doping level, the Curie temperature (T_C) rises and reaches its maximum at about 370 K for x=0.33. The transition from ferromagnetic to paramagnetic material is accompanied by a large drop in resistivity, while maintaining the overall metallic temperature dependence. (see Figure 4.10)

Chmaissem et al.[124] present the electronic phase diagram of LSMO for doping levels up until x=1. They identify four magnetic phases - one ferromagnetic and three antiferromagnetic (see Figure 4.11). The A-type antiferromagnetic phase demonstrates in-plane ferromagnetism and out-of-plane antiferromagnetism; C-type shows out-of-plane ferromagnetism and in-plane antiferromagnetism; G-type represents in-plane and out-of-plane antiferromagnetism. There is a strong competition between the ferromagnetic and A-type states for x≈0.5, and between the C- and G-type states for x≈0.95.

The manganites have been given special attention also because of the colossal magnetoresistance (CMR) they exhibit. This phenomenon consists in a huge resistivity re-

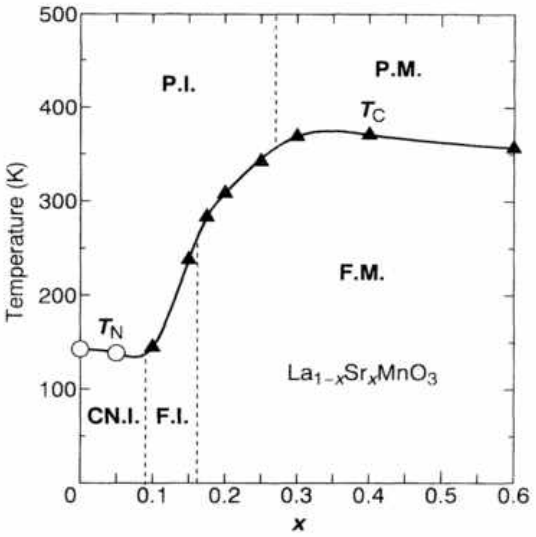

Figure 4.9: Electronic phase diagram of $La_{1-x}Sr_xMnO_3$. Open circles and filled triangles are the Neel (T_N) and Curie (T_C) temperatures, respectively. The abbreviations mean paramagnetic insulator (PI), paramagnetic metal (PM), spin-canted insulator (CNI), ferromagnetic insulator (FI), and ferromagnetic metal (FM)[123]

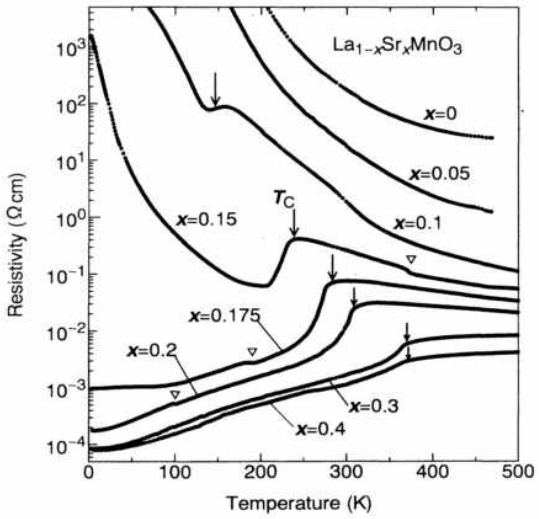

Figure 4.10: Temperature dependence of resistivity for $La_{1-x}Sr_xMnO_3$ crystals. Arrows indicate the critical temperature for the ferromagnetic phase transition. Anomalies indicated by open triangles are due to the structural transition.[123]

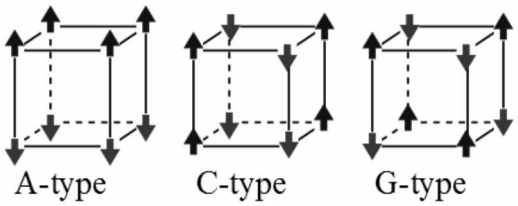

Figure 4.11: The types of magnetism in for the manganite crystal are shown. The A-type demonstrates in-plane ferromagnetism and out-of-plane antiferromagnetism; C-type shows out-of-plane ferromagnetism and in-plane antiferromagnetism; G-type represents in-plane and out-of-plane antiferromagnetism.

duction induced by a magnetic field. The CMR effect is exhibited at room temperature, while the tunnelling magnetoresistance vanishes at much lower temperatures. A magnetoresistance ratio of 1800% in LSMO/STO/LSMO junctions has been attributed to the half-metallicity of the manganites at the interface.[125] Dynamical Jahn-Teller effects or local lattice distortions are also thought to play an important role in CMR.[126,127]

When one material is half-metallic, it means that at Fermi level there are states in the majority spin channel and there are none in the minority, making it thus metallic in spin-up and insulator in spin-down. In this way, the current is conducted only by one channel, so it is 100% spin polarized. However, the opinions regarding the half-metallicity of LSMO are divided. Some recent experiments claim that the LSMO is not a conventional half-metal and that is does have minority spin states at the Fermi level, but it is rather a transport half-metal. This means that the spin polarization of the current in this material is approaching 100% in the high resistivity limit, which is mostly due to the different mobility of the spin-up and spin-down electrons.[128] On the other hand, other studies support the true half-metallicity of LSMO,[129,130] for which Nadgorny blames the different results on the various possible values of spin polarization that depend on the technique that is used.

The ferromagnetic phase of LSMO is explained with the double exchange mechanism, proposed by Zener.[131] The magnetism of LSMO is based on the magnetic properties of the Mn ions. In the LMO, all manganese ions are Mn^{3+}. When Sr ions are introduced, this gives rise to holes or Mn^{4+} in order to maintain the electroneutrality. Therefore, the ratio La^{3+}/Sr^{2+} is equivalent to Mn^{3+}/Mn^{4+}. In the octahedral environment, the d levels of the Mn split and give rise to triply degenerate t_{2g} and doubly degenerate e_g levels. The orbitals are filled according to the Hund's rule, so the spins of the electrons are parallel. Mn^{4+} has all electrons on t_{2g} orbitals, while Mn^{3+} has one more electron on e_g. This extra electron hops from the Mn^{3+} to the adjacent fully filled O $2p$ orbital and simultaneously an electron from that orbital goes to the Mn^{4+}. Anderson and Hasegawa[132] have shown that the electron transfer (t_{ij}) between the neighbouring sites depends on the relative angle (Θ) between the core spins, or $t_{ij} = t_0 cos(\Theta/2)$. The maximum value for the transfer is when the spins are parallel ($\Theta = 0$), thus resulting in ferromagnetic interaction.

Indeed, any structural distortions play an important role in the physical properties of the manganites, since they can change the Mn-O-Mn angle. Therefore the radius of the doped cations should be also taken into consideration. Hwang et al.[133] have demonstrated that by decreasing the radius of the A cations, $<r_A>$, magnetic order and significant magnetoresistance occur at lower temperatures with increasing thermal

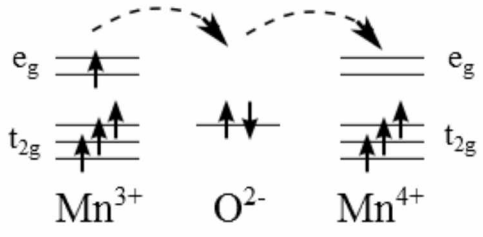

Figure 4.12: A schematic representation of the double exchange mechanism.

hysteresis, and the magnitude of the magnetoresistance increases dramatically. Other distortions come from the fact that the LMO has a distorted structure due to the Mn^{3+} which suffer Jahn-Teller distortions,[134] while the $SrMnO_3$ (SMO) has a cubic structure.

However, the double-exchange model alone cannot account on the CMR effect. Millis et al.[127] extended the double-exchange model and proposed that, in addition to double-exchange physics, a strong electron-phonon interaction arising from the Jahn–Teller splitting of the outer Mn d level plays a crucial role.

Theoretically, it is difficult to reproduce the experimental results, since the experiments are carried out at finite temperature, whereas the theoretical experiments are at 0 K. However, there are various factors that influence the half-metallicity and even though it has been generously claimed in the literature, few studies actually present a 100% spin polarization at the Fermi level. One factor is the functional. The LSMO bulk has been investigated at different levels of theory - LDA and GGA. The former has some limitations for magnetic systems and band gaps. Moreover, it gives different results with respect to the lattice constant that is used. For the pseudocubic experimental value, the approximation reproduces the half-metallicity, however, when an optimized one is used, this property of LSMO is lost.[135,136] On the other hand, GGA calculations for both optimized and experimental cases result in half-metallic LSMO.[136] This would imply that GGA describes better the geometrical structure and resulting properties for LSMO. Indeed, Ferrari et al. have shown that the half-metallicity is strongly related to the lattice constant, so for smaller values it is lost.

Another factor is the construction of the bulk phase. A layered model leads to non half-metallic behaviour, while the homogeneously distribution of the Sr atoms gives rise to half-metallicity.[137] Moreover, the relaxation of the structure increases the spin polarization,[137] which is also favoured when the parameter U for on-site Coulomb interactions is added.[138,139]

In this study, the final goal is to be able to model LSMO surface(s) which reproduce the experimental results and in order to be used as a support for $Fe_4(dpm)_6$ adsorption. First, the phase bulk is studied. Then models for the surface are proposed, simulated and checked for reproduction of the experimental data of their structural, magnetic and electronic properties.

4.3.1 Bulk

In this study, the LSMO bulk have been studied on a GGA level of theory with dispersion corrections D3.[36] The functional that has been used is revPBE.[31] Double-ζ molecularly optimized and polarized basis sets[71,140] have been used for all elements together with GTH norm-conserving pseudopotentials.[28,70] For the oxygen atoms, the $2s$ and $2p$ elec-

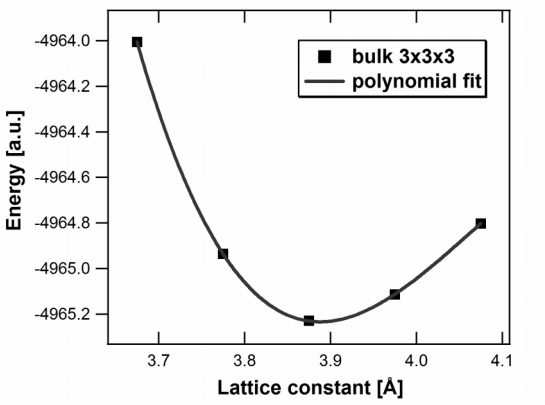

Figure 4.13: The lattice constant with minimum energy for LSMO has been estimated, using a polynominal fit.

trons have been considered explicitly. In the case of Mn the outer 15 electrons (3*s*, 3*p*, 4*s*, 3d), for the Sr the outer 10 (4*s*, 4*p*, 5*s*) and for the La the last 11 (5*s*, 5*p*, 5*d*, 6*s*). The plane-wave cut-off has been set to 400 Ry in agreement with other theoretical studies.[141] The criteria for SCF convergence and forces are 1×10^{-6} Hartree and 1×10^{-3} HartreeBohr^{-1}, respectively.

The doping level x that has been used throughout the study is 0.33. Therefore, 33% of the total number of A sites has been substituted with Sr atoms and the same amount of B sites have been replaced with Mn^{4+} ions. The electroneutrality of the system has been therefore guaranteed. Both Sr and Mn^{4+} have been distributed in a homogeneous random manner in the bulk phase.

In agreement with the experiment at this doping level,[123] the bulk phase has been studied in its ferromagnetic state. Therefore, all manganese ions have been considered in their high spin state.

Several models have been considered for the study of the LSMO bulk. A smaller one, which consists of a simulation cell where the unit cell is repeated 3 times in x, y and z directions, has been used to determine the lattice constant for the bulk LSMO at this level of theory. The cubic cell has been adopted. Five values have been chosen around the experimental one and for each of them the bulk phase has been subjected to geometry optimization. The resultant equilibrium lattice constant for this computational protocol is found to be 3.875 Å (see Figure 4.13) and it reproduces well the experimental one (3.873 Å).[142] Other GGA studies show even worse results for the lattice constant (3.91 Å[136]).

Once the lattice constant has been determined, a larger simulation cell (7×7×3) has been modelled in order to study the geometry and the electronic properties. The dimensions of such cell are (27.125×27.125×11.625) Å^3 and they have been chosen in order to match the size of the surface slab (see the next subsection *Surfaces*).

Geometry

The optimization of the geometry hardly leads to any changes in the positions of the metallic ions. As expected, the largest displacements concern the La-Sr atoms, due to their different size. At the same time, the oxygen atoms in the two planes, (LaSrO) and (MnO_2), behave in a different way. In the former case, they seem to be less mobile with a maximum difference between their positions of 0.02 Å. In the latter, it is estimated to

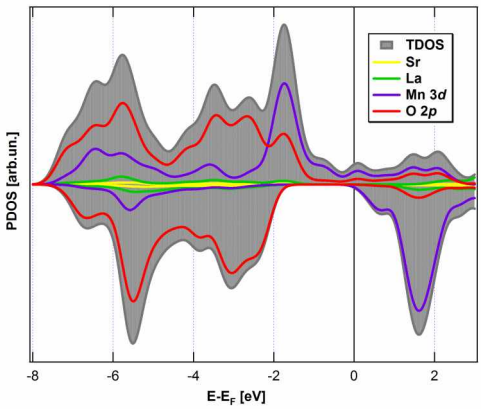

Figure 4.14: The TDOS and PDOS of LSMO bulk for the 7x7x3; the used σ is 0.3 eV.

be about 0.20 Å, even though on average the O atoms remain in the plane of the Mn ions. For these reasons, the Mn-O distance in the direction across the (LaSrO) layer of the slab maintain the bulk value of 1.938, while those in the xy planes fluctuate much more around the average value (from 1.93 to 1.97 Å). The average angle Mn-O-Mn in the (MnO_2) is estimated to be 171.1 °. Being lower than 180 °, a negative effect on the double exchange interactions is therefore expected.

Electronic properties

The density of states for the bulk phase shows that the states in the Fermi region are mainly due to the hybridization between the O 2*p* and Mn 3*d*, while the Sr and La states remain low-lying. The TDOS for the bulk LSMO are in good agreement with several other theoretical studies,[136,138] as well as the Mn 3*d* PDOS.[143] Moreover, the majority spin levels are occupied at the Fermi level, while the minority are not, giving thus rise to a spin polarization of the bulk estimated to be 99% at (0K). This result is in agreement with the experimental value of 95% (at 4K).[125] Considering that the low lying minority spin excited bands lie very close to the Fermi energy, the fully half-metallic character for the bulk would be lost at room temperature.

The gap in minority spin channel is evaluated to be 2.21 eV, which is higher than the experimental one of 1.2 eV,[129] but in line with previous results.[138]

The average magnetic moment of the manganese ions in the bulk phase has been estimated to be 3.56 μ_B, which is in good agreement with the experimental value of 3.7 μ_B.[144]

4.3.2 Surfaces

Studies on the properties of LSMO surfaces are of high importance, since most of the spintronic devices include LSMO thin films or interfaces. Therefore, such systems have been extensively studied at experimental level, but less at the theoretical one. The structure of the LSMO surface strongly depends on the experimental techniques that have been used and its slab thickness is crucial for its physical properties.

When a thin film of LSMO is grown on a substrate (usually $SrTiO_3$ (STO), $NdGaO_3$ (NGO), $LaAlO_3$ (LAO)) strain effects appear due to the different lattice constants. For instance the mismatch between STO and LSMO is of 0.035 Å. This leads to distortions in MnO_6,[145] which could be crucial for the magnetic properties of the system. For instance,

the presence of an electrical "dead layer" at the substrate-film interface boundary is well-known. Its thickness is between 30 and 50 Å for both LSMO on STO and LSMO on NGO and slightly thicker for LSMO on LAO (between 50 and 80 Å).[146] Nonetheless, these films still exhibit magnetoresistive behaviour.[147]

In addition to these problems, there has been discussion over the chemistry of the top layer. It is proven that it depends on the cleaning procedure[148] and on the substrate the LSMO films are grown.[149] There are several studies which suggest the presence of the (MnO_2) termination layer.[150,151] Theoretically, Piskunov et al. demonstrated that in pure LMO, only (MnO_2) is thermodynamically favourable, whereas the Sr doping makes the (LaSrO) termination layer more favourable (x=1/8) for high temperatures (at room T both terminations are stable).[152]

Other more recent experimental studies have proven that the topmost layer is mainly composed of SrO, due to the segregation process of the Sr atoms from the bulk to the surface.[147] The Sr-segregation has been studied at various experimental conditions[141,153–155] and it has been observed with x-ray electron spectroscopy techniques for various stoichiometry ratios[156–158] The reason for the Sr-segregation is due to the size of the Sr-ion with respect to the La one. It is also considered that it is a result of the formation of Ruddlesden Popper phase, i.e. $(La,Sr)_{n+1}Mn_nO_{3n+1}$ with n=1, or for the formation of a uniform strontium oxide (SrO) monolayer.[159,160]

This study aims at presenting a reliable model for the LSMO surface in agreement with the experimental findings. For this reason, the possible composition of the topmost layer is studied through Sr segregation for different model systems. Then, the changes in their electronic structure are investigated. Finally, the most stable surfaces are tested for their magnetic properties.

The same computational protocol for the bulk phase is also used for the surfaces. A slab of 7×7×3 times the unit cell in the three dimensions has been chosen so that the surface can host one $Fe_4(dpm)_6$ cluster and in the same time guarantee enough separation from its periodic images along x, y and z. Another reference slab, 5×5×5, has also been modelled in order to verify the reliability of the thinner model. Similar thickness of the slabs have been used in other theoretical simulations.[141,143,152,161] The use of the bulk lattice constant can be considered a good approximation since the strain effects have minor influence on the half-metallic gap and magnetic moments.[138] In order to reduce significantly the surface dipole generated by the asymmetric slabs, an empty space of about 50 Å was used. The simulation cells are (19.375×19.375×60.000) $Å^3$ and (27.125×27.125×60.000) $Å^3$ for the 5×5×5 and 7×7×3, respectively.

A difficulty in the LSMO models is that each layer is formally charged. In order to avoid the problem of charged systems in periodic approximations, extra approximations should be introduced such as Mn^{3+}/Mn^{4+} ratio and/or oxygen vacancies. However, the oxygen vacancies are unwanted, since they break the stoichiometry of the systems and the essential for the conductivity bridges between the Mn ions. In addition to that, they go in hand with the presence of Mn^{2+} ions.[162,163] Since they are strongly localized in character, they do not contribute directly to the charge injection across the interface.[162] Picozzi et al. have pointed out that oxygen vacancies destroy half-metallicity, leading to possible consequences on the LSMO spin injection efficiency.[164] To avoid such spurious choices, asymmetric simulation cells have been used, unlike previous theoretical studies.[141,152] However, apart from the appearance of a surface dipole, both symmetric and asymmetric slabs give similar geometrical and electronic results.[161]

The surface models take into consideration both [MnO_2] and [LaSrO] termination layers (see Figure 4.15), where the use of square brackets indicates the topmost layer.

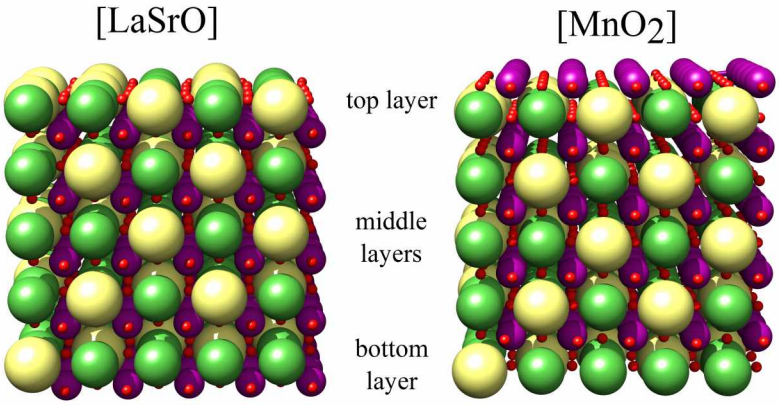

Figure 4.15: The 5×5×5 $La_{0.67}Sr_{0.33}MnO_3$ models presenting the two termination layers are pictured.

During all geometry optimizations, the bottom atomic layer has been kept to the bulk positions. In that way a bulk-like behaviour is induced on the bottom layers and surface-like for the top ones, which could enable in a way discern the two termination layers.

The Sr ion concentration has been chosen to be 33% (experimental). The 7×7×3 model has a total of 49 Sr ions and 98 La ions, which would mean formally 49 Mn^{4+} and 98 Mn^{3+}, in agreement with the doping level and charges neutrality conditions. In comparison, 5×5×5 has 125 Mn-ions, 41 of which are Mn^{4+} and 84 are Mn^{3+}. Various distributions of the strontium atoms have been assumed in order to take into account the Sr segregation and they are discussed in the next section.

Surface segregation and surface energy

In literature, there are several theoretical studies on the Sr segregation, however, none of them treats explicitly the way that the Sr atoms are distributed in the slab.[141,152] In this work, different models have been examined (see Figure 4.16). The bulk-like distribution is represented by the homogeneous models, [LaSrO-hg], both 5×5×5 and 7×7×3 slabs. Due to the greater thickness of 5×5×5 surface, it has been possible to distribute the Sr ions in more different ways. The first is the gradient one, where at the top layer the Sr/La is inverted with respect to the bulk (1:2) and gradually the quantity of Sr diminishes until reaching 16% for 5×5×5. Next, three similar models have been adopted, where the gradient distribution is present for four layers, while the bottom one is kept at the bulk La/Sr ratio. Moreover, the percentage of Sr in the topmost layer increases from distribution 1 (distr1) to distribution 3 (distr3). In this way, it can be evaluated whether it is more important to have more Sr at the surface or also their distribution in the underlying layers. Similar, yet more limited models have been prepared for the thinner slab 7×7×3. The [LaSrO-grad] is assumed to have a similar behaviour to the [LaSrO-grad] in 5×5×5, since the Sr are distributed in a gradient manner. In addition, they both have 67% of Sr at the top layer, even though the percentages are not exact for the underlying layers (12% vs. 16% for the bottom). However, the allocation of [LaSrO-nograd] to some of the 5×5×5 models in not easy. It tries to mimic the segregation as a massive Sr migration from the middle layers to the topmost one, keeping the bottom one

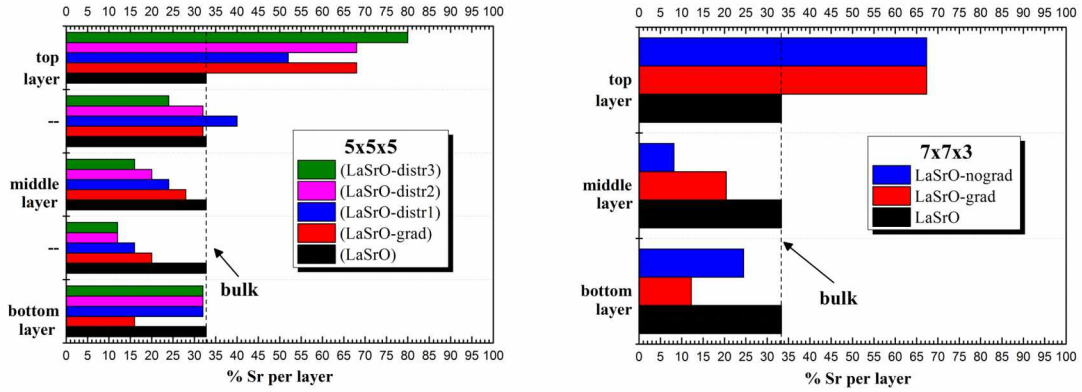

Figure 4.16: Distribution of the Sr atoms according to the layer they are in for the different models and slabs - 5×5×5 (left), 7×7×3 (right)of $La_{0.67}Sr_{0.33}MnO_3$.

close to the bulk La/Sr ratio. Similar pattern is found in [LaSrO-distr3], where however, the ratio of Sr atoms in the topmost layer is higher.

The so called surface energy, E_{bulk}, has been used as a criterion to give an estimation of the surface stability between the different termination layers and Sr segregation models. In this study, the surface energies have been computed for all the different surface models according to a modified version of equation 4.1:

$$E_{surf} = \frac{(E_{slab} - E_{bulk})}{A_{surf}} \tag{4.5}$$

where A_{surf} is the surface area and for E_{bulk} we considered the energy computed for a homogeneous Sr bulk distribution in a 7×7×3 periodic supercell. It is evident that such definition of E_{surf} takes with it the composition issues coming from the asymmetry of the surface models. Indeed, both top and bottom layer energy contributions are present in the E_{surf} term. However, even if a direct comparison between [MnO_2] and [LaSrO] energy surfaces is not possible for the reasons mentioned before, a qualitative indication which suggests the [LaSrO] surfaces to be more stable than the [MnO_2] can be extrapolated. On the other hand, the direct and quantitative comparison among the [LaSrO] models is possible. The results for surface energy are presented in tables 4.7 and 4.9.

In the case of 5×5×5, two more models with 50 and 67% of Sr have been simulated in order to evaluate the effect on the stability of the presence of more Sr atoms in the bulk. For both, gradient and homogeneous distributions have been considered. A corresponding bulk with the same slab size has been optimized in order to obtain the E_{bulk} for the calculation of E_{surf}. The displacement of the Sr ions towards the surface lowers the E_{surf} term for all models. This is clearly seen for the three distributions - [LaSrO-distr1], [LaSrO-distr2] and [LaSrO-distr3], where the surface energy gradually decreases when passing from 52% to 80% Sr at the topmost layer.

The rise in the doping level confirms that the more Sr there is in the bulk, the less stable the surface is. However, there is no linear effect on the surface energy. While at 50% E_{surf} increases drastically, the 67% value is lower, yet higher than the 33% one.

As it has been discussed before, this calculation of the surface energies has its limitations. The simulation cell of the bulk has not been the same as for the slab. Therefore, in order to get the right surface energy, geometry optimization of surfaces with different

Table 4.7: Surface energies , E_{surf}, for the LSMO 5×5×5 surfaces.

	x(Sr) in %	Surface model	Distribution	E_{surf} (Jm^{-2})
5×5×5	33	[MnO_2]	homogeneous	2.548
		[LaSrO-hg]	homogeneous	2.390
		[LaSrO-grad]	gradient	1.992
		[LaSrO-distr1]	mixed	2.160
		[LaSrO-distr2]	mixed	2.064
		[LaSrO-distr3]	mixed	1.986
	50	[LaSrO]	homogeneous	2.723
		[LaSrO]	gradient	2.443
	67	[LaSrO]	homogeneous	2.530
		[LaSr]	gradient	2.248

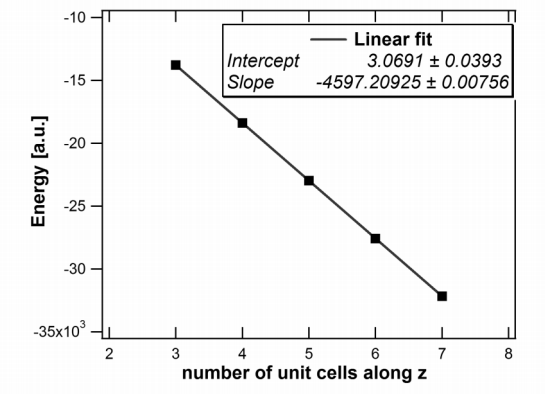

Figure 4.17: The energy versus the number of layers gives as slope the bulk energy for the system homogeneous distribution of the Sr atoms.

number of layers should be performed. The reformulation of equation 4.1 gives equation 4.6, from the slope of which the new E_{bulk} is extracted.[86]

$$E_{slab}^{N} \approx 2\sigma + NE_{bulk} \tag{4.6}$$

Geometry optimizations of five 5×5 surfaces have been performed with doping level of 33%, where the number of unit cells along z goes from 3 to 7. All atoms have been relaxed in agreement with other theoretical calculations.[86] The resultant E_{bulk} is obtained according to Figure 4.17 and the new surface energies are presented in Table 4.8. They are significantly higher than the ones obtained with a separate bulk calculation. However, this approach is too expensive from a computational point of view for such big systems. Since the surface energy serves to discern the stability of the different models, the equation 4.5 will be used for the larger slab models.

Once the tendencies for the Sr distributions in 5×5×5 have been obtained, similar models have been used also for the thinner slab 7×7×3 in order to check the reliability of the model (see Figures 4.16 and 4.18 and Tables 4.7 and 4.9). Even if the limited thickness of this slab model does not allow for an almost total concentration of Sr ions on the outermost layer, as suggested by LEIS experiments,[155] the reported computed energy undoubtedly reproduces the observed experimental trend and also in this case,

Table 4.8: Surface energies , E_{surf}, for the LSMO 5×5×5 surfaces with the new bulk energy

	x(Sr) in %	Surface model	Distribution	E_{surf} (Jm^{-2})
5×5×5	33	[MnO_2]	homogeneous	3.829
		[LaSrO-hg]	homogeneous	3.671
		[LaSrO-grad]	gradient	3.273
		[LaSrO-distr1]	mixed	3.442
		[LaSrO-distr2]	mixed	3.345
		[LaSrO-distr3]	mixed	3.267

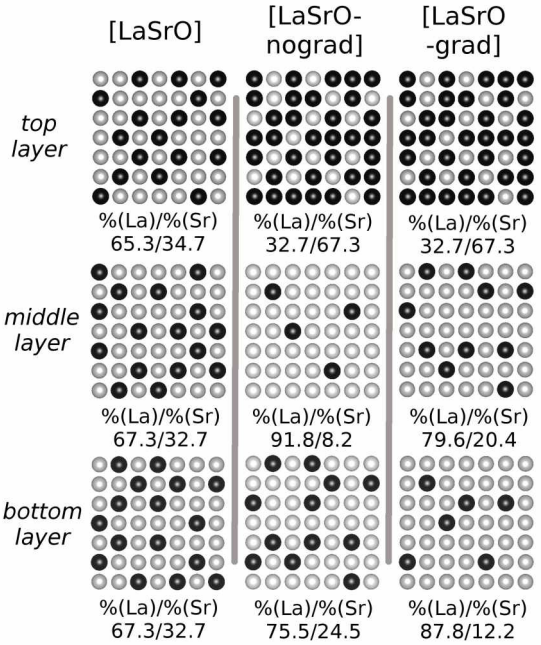

Figure 4.18: Distribution of the Sr atoms in the [LaSrO] surfaces. The total ratio between Sr:La is 1:2 for all surfaces, even though the ration changes for the different layers.The Sr-ions are in light grey, and the La-ions in black.

the segregated surfaces are more stable. However, compared with the 5×5×5, the lowest surface energy is for the gradient distribution, [LaSrO-grad], and not for the [LaSrO-nograd], which is supposed to mimic the [LaSrO-distr3]. As a whole, the E_{surf} values for the similar models are lower for the thicker model than for the 7×7×3. This could be assigned to the larger surfaces that are being created and to the thinness of the slabs.

Working with asymmetric slabs gives rise to surface dipole in the vacuum layer due to the differently charged termination layer. In order to estimate its effect, single point dipole corrected[82] runs on non-corrected optimized structures have been performed. A comparison of the electrostatic potentials along z (corrected, non-corrected) are reported in Figure 4.19. Noteworthy, the small and practically constant bias, about -0.01 J/m2, introduced by non-considering the surface dipole corrections along z, confirms the soundness of the cell dimension adopted in our computations. Moreover, the electric fields inside the slab has been calculated using the following formula:

$$E_{depol} = -\delta(\Delta V_{es})/z_{simulationcell} \tag{4.7}$$

Table 4.9: Surface energies , E_{surf}, for the LSMO 7×7×3 surfaces

	x(Sr) in %	Surface model	Distribution	E_{surf} (Jm^{-2})[a]	E_{surf} (Jm^{-2})[b]
7×7×3	33	[MnO_2]	homogeneous	2.853	2.861
		[LaSrO]	homogeneous	2.633	2.644
		[LaSrO-nograd]	mixed	2.369	2.379
		[LaSrO-grad]	gradient	2.334	2.344
	37	[LaSrO]	homogeneous	2.723	-
		[LaSrO]	gradient	2.443	-
	41	[LaSrO]	homogeneous	2.530	-
		[LaSrO]	gradient	2.248	-
	45	[LaSrO]	homogeneous	2.530	-
		[LaSrO]	gradient	2.248	-

[a] computed without surface dipole correction
[b] computed with surface dipole correction

where $\delta(\Delta V_{es})$ is the surface dipole that appear as a result of the asymmetric slab. The low values are in agreement with values for other perovskite structures[165] and confirm that the reliability of the geometries obtained for the asymmetric slabs.

In conclusion, both slab models confirm that the Sr segregation is more favourable for the [LaSrO] termination layer where the Sr atoms are distributed in a gradient manner. Moreover, both [MnO_2] slabs exhibit surface energy higher than the [LaSrO] ones in agreement with the experimental findings.

Electronic properties

The validity of the 7×7×3 models at 33% has been tested by studying their density of states. (see Figure 4.20 and 4.21). The most stable models of the two kinds of slab for the [LaSrO] termination layer have been compared in Figure 4.20a. Since the number of atoms in the simulation cells differ, the TDOS for the 5×5×5 have been multiplied by a factor in order to match those of 7×7×3. The general shape of the TDOS is maintained, even though a slight shift to lower energies of the 5×5×5 states in the region -3 ÷ -6 eV is observed. Moreover, the same slab shows a reduced density of states at the Fermi level. Similar comparison has been made also for the [MnO_2] termination layer, where no major differences have been found between the two slabs.

The segregation does not induce significant changes in the TDOS (see Figure 4.20b and d). For the segregated 5×5×5 model, a subtle shift of the peak at -2 eV in the top layer 3*d* Mn PDOS is observed with respect to the homogeneous distribution, which is not present for the 7×7×3 slab. This could be due to the different spin densities on the top Mn ions that appear with the Sr-segregation. Indeed, in the 5×5×5 slab difference between the values in [LaSrO-distr3] e [LaSrO-hg] is 0.22, while for the 7×7×3 slab it is 0.08 (see Tables 4.10 and 4.11). This would mean slightly more Mn^{3+} and therefore, the more high-lying e_g orbitals are filled, giving rise to the shift.

Useful information about the changes that occur on the Mn ions in the surface slab can be extracted from the 3*d* PDOS per layer (see Figure 4.22 and 4.23). The two slabs have been compared by termination layer in order to study the differences induced by the thickness. In the case of [LaSrO], all layers tend to have the form of the bulk PDOS,

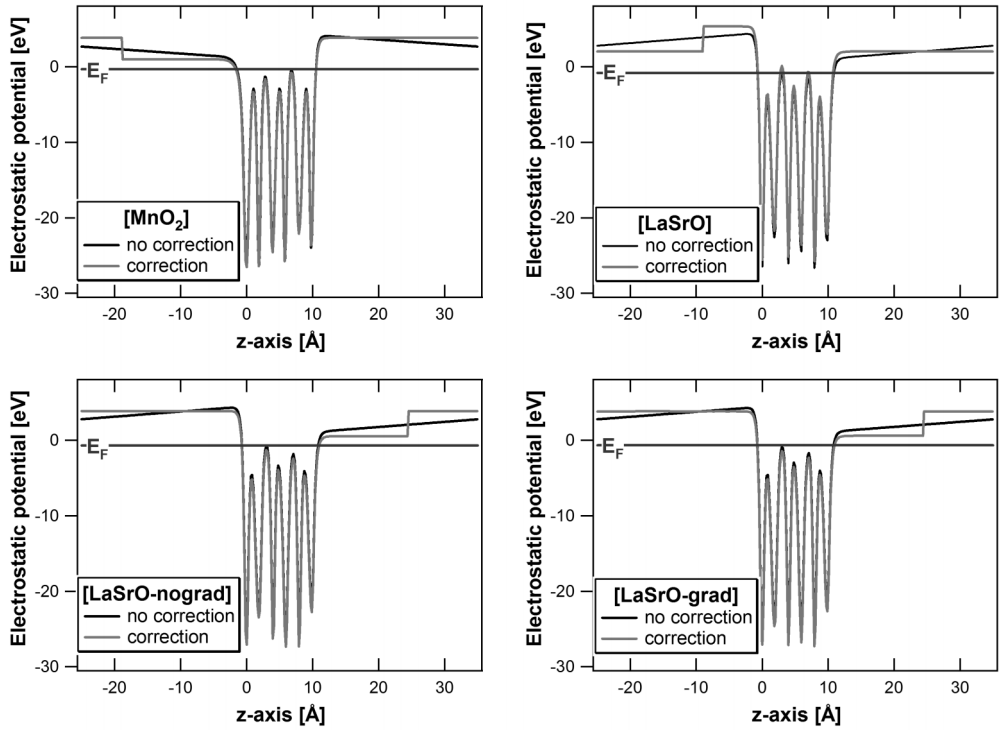

Figure 4.19: The electrostatic potential along the z axis is plotted for the four 7×7×3 surfaces with 33% Sr with (grey) and without (black) correction of the surface dipole.

except for the bottom one, which is totally different. This is ascribed to the fact that in all previous cases, the Mn ions are in octahedral environment, while in the bottom layer the Mn ions are penta-coordinated. This seriously affects surface states. Indeed, $[MnO_2]$ slabs, in the top layer, the peak at about -2 eV transforms into a group of peaks. Similar PDOS for $[MnO_2]$-terminating surfaces have been also observed with other theoretical calculations.[143]

Moreover, the characteristic peak at about -2 eV shift towards the Fermi level going from bottom to top layer for both $[MnO_2]$ slabs, while the opposite behaviour is observed for [LaSrO] ones. Such energy shift was also found for $[MnO_2]$ in the recent literature.[136]

In addition, a comparison with the bulk PDOS confirms the middle layers have a bulk-like behaviour for both slab thicknesses. The general shape is maintained, even though in the case of 5×5×5 $[MnO_2]$, the peaks at -6 eV are inverted with respect to the bulk ones. This confirms the validity of both 5×5×5 and 7×7×3 slabs.

The distribution of spin densities is clearly different for the two termination layers. In the case of $[MnO_2]$, the top layer is mainly occupied by Mn^{3+} ions. A penta-coordination is more favourable in the case of d^4, due to the presence of one electron on the e_g orbitals, which in this case are lowered in energy. Indeed, the values are practically identical for both slabs. Such results are in agreement with some theoretical studies (Pruneda et al. find 3.66 spin density for $[MnO_2]$-termination layer, with respect to 3.53 for the corresponding bulk[143]), and at odds with others, where it is thought that the top layer brings contamination of the spin polarization, the magnetic moments are reduced near the surface to 3.4.[136]

As a compensation, the underlying layers show more presence of Mn^{4+} and the bottom layers are more similar to the bulk value, even though they do not reproduce it perfectly.

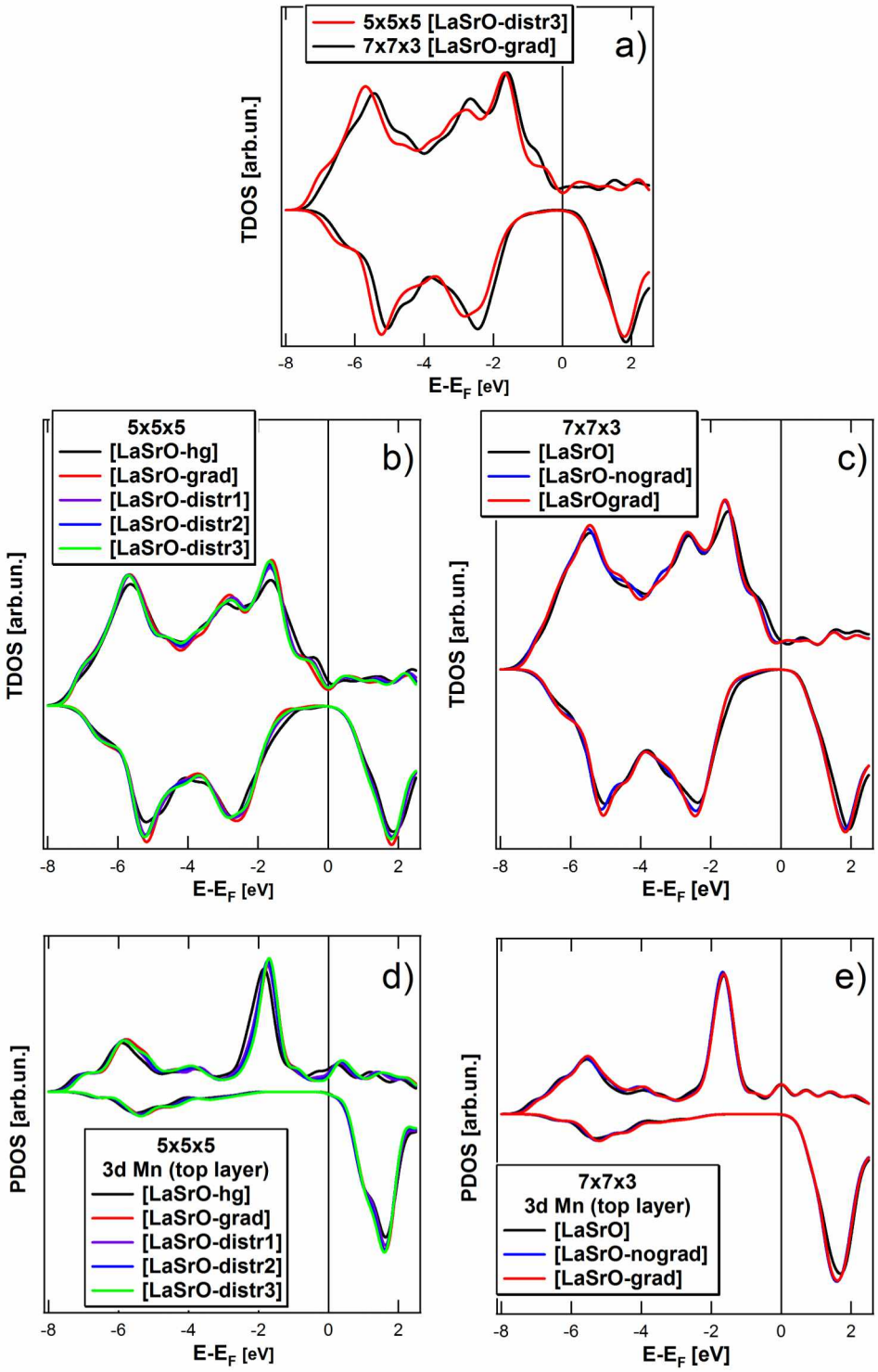

Figure 4.20: Density of states for the different models of [LaSrO]-terminating layers; a) comparison between the most stable models for 5×5×5 and 7×7×3 slabs, where the TDOS of the former has been scaled with respect to the ones of the latter; b) TDOS for all models of the 5×5×5 slab; c) TDOS for all models of the 7×7×3 slab; d) and e) present the DOS projected on the Mn 3*d* of the top layer for model of 5×5×5 and 7×7×3 slabs, respectively. The σ in all cases is 0.3eV.

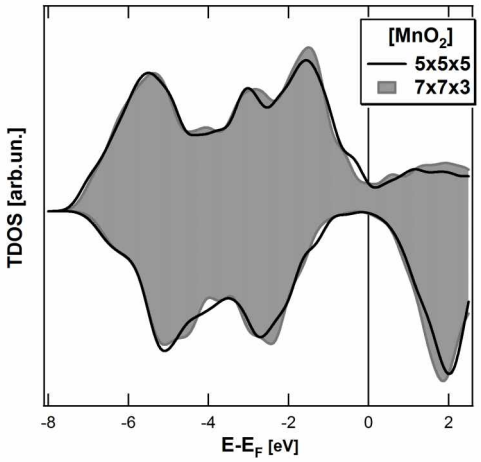

Figure 4.21: Comparison between the TDOS of 5×5×5 and 7×7×3 slabs for [MnO_2]-termiantion slab, the TDOS of the former has been scaled with respect to the ones of the latter. The σ is 0.3 eV.

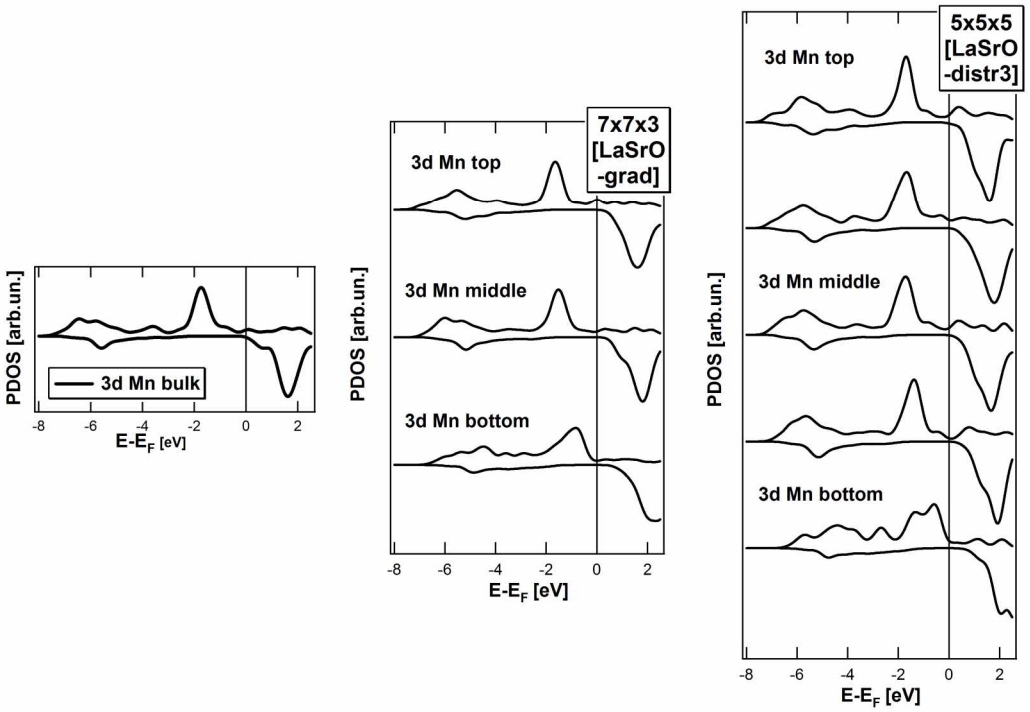

Figure 4.22: The density of states projected on the 3d orbitals of the Mn ions for the bulk (left) and by layer for 7×7×3 (middle) and 5×5×5 (right) for the [LaSrO]-termination layer. The σ is 0.3 eV.

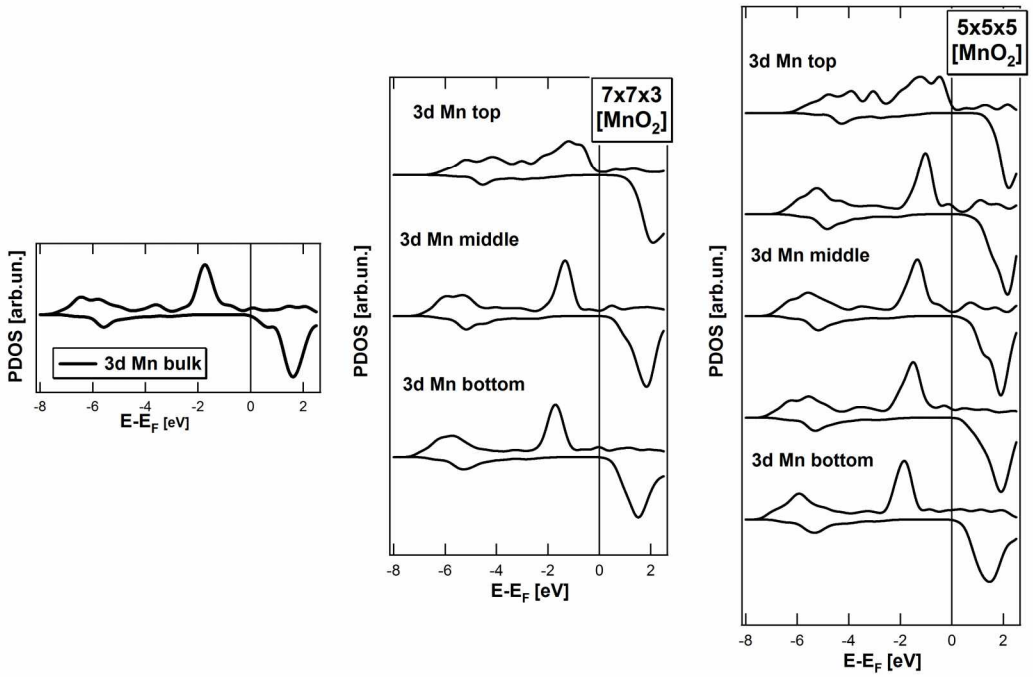

Figure 4.23: The density of states projected on the $3d$ orbitals of the Mn ions for the bulk (left) and by layer for $7\times7\times3$ (middle) and $5\times5\times5$ (right) for the $[MnO_2]$-termination layer. The σ is 0.3 eV.

In the case of $5\times5\times5$, a fluctuation between high and low values is present until the bulk one is reproduced. It is due to the redistribution of the spin densities within the slab as result of the imbalance induced from the topmost layers. Such fluctuation is not observed in the $7\times7\times3$ slabs due to their limited thickness.

The [LaSrO]-termination induces different rearrangement of the spin densities, even though the general trend of having similar values in reversed order is maintained. The fixed bottom layer is a not-relaxed penta-coordinated and, therefore, in agreement with the results for the top $[MnO_2]$ more Mn^{3+} spin density is observed. Quite interestingly, there is no sharply pronounced presence of Mn^{4+} in the top layer of both segregated models as expected, due to the higher Sr concentration. The spin density is decreased with respect to the homogeneous slabs in a more pronounced way in the case of $5\times5\times5$.

Contrary to the bulk, it is accepted to think that the LSMO surfaces are indeed half-metallic.[166] To check this, the spin polarization for the different models has been calculated according to the equation:

$$P = \frac{(N_{up} - N_{down})}{(N_{up} + N_{down})} 100 \tag{4.8}$$

and presented in Table 4.12. The decrease in the spin polarisation for $[MnO_2]$ is in agreement previous DFT studies.[136] On the other hand, for all [LaSrO] terminating surfaces, the values are very close to the bulk ones, with almost no differences between them. There are no significant differences between the differently segregated and homogeneous surfaces.

The minority-spin band gaps computed between the occupied O $2p$ orbitals and the unoccupied Mn $3d$ are reported in Table 4.13. Even though the values for the $7\times7\times3$

Table 4.10: Distribution of the Mn spin densities for the different models of 5×5×5 (see Figure 4.16).

[MnO_2]	Layer	[LaSrO]	[LaSrO-distr3]
3.89	Top	3.68	3.46
3.33		3.64	3.70
3.40	Middle	3.41	3.51
3.64		3.46	3.48
3.55	Bottom	3.69	3.75
3.56	Average	3.58	3.58
Bulk		3.56	

Table 4.11: Distribution of the Mn spin densities for the different models of 7×7×3 (see Figure 4.16).

[MnO_2]	Layer	[LaSrO]	[LaSrO-grad]
3.88	Top	3.53	3.48
3.32	Middle	3.47	3.49
3.44	Bottom	3.73	3.77
3.54	Average	3.58	3.58
Bulk		3.56	

Table 4.12: Spin polarization in% for all models considered, calculated as the difference between the density at Fermi level in the majority and minority spin channels divided by their sum.

	x(Sr) in %	Surface model	Distribution	Spin polarization (%)
5×5×5	33	[MnO_2]	homogeneous	87.8
		[LaSrO-hg]	homogeneous	94.4
		[LaSrO-grad]	gradient	92.8
		[LaSrO-distr1]	mixed	92.8
		[LaSrO-distr2]	mixed	92.4
		[LaSrO-distr3]	mixed	93.0
		bulk		59.1
7×7×3	33	[MnO_2]	homogeneous	98.3
		[LaSrO]	homogeneous	99.3
		[LaSrO-nograd]	mixed	99.1
		[LaSrO-grad]	gradient	99.1
		bulk		99.1

Table 4.13: Gap in the minority spin channel for all models of LSMO considered in this study.

	x(Sr) in %	Surface model	Distribution	Gap (eV)
5×5×5	33	[MnO_2]	homogeneous	0.65
		[LaSrO-hg]	homogeneous	0.71
		[LaSrO-grad]	gradient	1.06
		[LaSrO-distr1]	mixed	0.77
		[LaSrO-distr2]	mixed	0.79
		[LaSrO-distr3]	mixed	0.82
		bulk		2.14
7×7×3	33	[MnO_2]	homogeneous	0.82
		[LaSrO]	homogeneous	0.96
		[LaSrO-nograd]	mixed	1.15
		[LaSrO-grad]	gradient	1.20
		bulk		2.21

Table 4.14: Rumpling parameters r for the most stable surfaces, calculated as $r = z(O) - z(Mn)$

5×5×5	**[MnO_2]**	**[LaSrO-hg]**	**[LaSrO-distr3]**
r_{top} (Å)	−0.18	0.04	−0.09
	−0.15	0.06	−0.01
r_{middle} (Å)	−0.08	0.08	0.04
	−0.06	0.13	−0.14
r_{bottom} (Å)	−0.06	0.00	−0.01
7×7×3	**[MnO_2]**	**[LaSrO-hg]**	**[LaSrO-grad]**
r_{top} (Å)	−0.17	0.05	−0.05
r_{middle} (Å)	−0.14	0.12	0.06
r_{bottom} (Å)	−0.08	0.00	0.00

slabs are slightly higher than those of 5×5×5, the same tendencies are reproduced by both of them. For all the surface models a narrowed band gap is observed with respect to value computed for the corresponding bulk. Therefore, the striking property of LSMOs, i.e. the half-metallic character, is shown to be maintained for all surface models, independently from the termination layer. However, slightly larger minority-spin band gaps have been found for the [LaSrO]-like termination surface unit cells. Moreover, the gap tends to open with a more pronounced Sr-segregation, which could mean the half-metallicity would be maintained to higher temperatures.

Geometry

The electron-lattice interactions play an important role in the electronic properties of LSMO.[167] Therefore, finding the right geometry of the system is mandatory.

Several parameters have been checked for the [MnO_2] and [LaSrO] termination layers. The effects induced upon segregation have also been accounted for. Since the Mn-O distances are very important for the magnetic properties, special attention has been dedicated to them.

Table 4.15: Average interlayer separation in Å, calculated as the average between the planes of the Mn atoms and that of the axial oxygen atoms in the successive [LaSrO]-planes.

5×5×5	**[MnO_2]**		**[LaSrO-hg]**	**[LaSrO-distr3]**
Δ_{Mn5-O5}	2.200	Δ_{O5-Mn5}	2.122	1.965
Δ_{O5-Mn4}	1.842	Δ_{Mn5-O4}	1.982	2.016
Δ_{Mn4-O3}	2.074	Δ_{O4-Mn4}	2.055	2.026
Δ_{O3-Mn2}	1.904	Δ_{Mn4-O3}	1.979	2.023
Δ_{Mn3-O3}	1.992	Δ_{O3-Mn3}	1.997	1.980
Δ_{O3-Mn2}	1.975	Δ_{Mn3-O2}	1.900	1.945
Δ_{Mn2-O2}	2.050	Δ_{O2-Mn2}	2.069	2.066
Δ_{O2-Mn1}	1.931	Δ_{Mn2-O1}	1.879	1.880
Δ_{Mn1-O1}	1.940	Δ_{O1-Mn1}	2.011	2.046
7×7×3	**[MnO_2]**		**[LaSrO-hg]**	**[LaSrO-grad]**
Δ_{Mn3-O3}	2.174	Δ_{O3-Mn3}	2.064	1.974
Δ_{O3-Mn2}	1.838	Δ_{Mn3-O2}	1.933	1.998
Δ_{Mn2-O2}	2.064	Δ_{O2-Mn2}	2.088	2.028
Δ_{O2-Mn1}	1.908	Δ_{Mn2-O1}	1.884	1.915
Δ_{Mn1-O1}	1.907	Δ_{O1-Mn1}	2.018	2.029

The first parameter to be checked is the rumpling of the oxygen atoms with respect to the Mn ones (see Table 4.14). The metal ions relax more than the oxygen ones, and this leads to the rumpling. In the case of [MnO_2] termination, the O stay below the plane formed by the Mn atoms. Such behaviour is observed also by Pruneda et al.[143] As they also point out, it is triggered by the surface chemistry, and it later propagates to the bulk phase, where it is not observed. The origin is suggested to be a polar, ferroelastic instability.[143 *and references therein*] Such effect leads to significant distortion of the Mn-O-Mn angle in the top atomic layer (the average value for 7×7×3 is ten degrees lower than the ideal 180 °). Similar value is observed also for the underlying layer, while the bottom layers show significantly lower rumpling.

The opposite trend and in reversed order is noticed for the homogeneous [LaSrO] surface, where the oxygen atoms are directed inward the bulk phase. This is not surprising, since the structure of this model is the one of [MnO_2] turned upside down, where, however, the bottom (MnO_2) plane is kept fixed. Interestingly enough, this changes when the Sr segregation is introduced. The oxygen atoms remain in the Mn plane with very small changes in their position along z.

The in-plane Mn-O bonds remain slightly changed (*i.e.* 1.946±0.017 Å for [LaSrO-grad]), unlike the out-of-plane ones (see Table 4.15). The reason for such discrepancies is to be searched in the distribution of the spin densities in the surface layers. Indeed, for the case of interfaces, it has been found that the elongation of the out-of-plane is not due only to the strain, but also to the presence of ions in lower oxidation states.[147]

The geometry changes in 5×5×5 and 7×7×3 are consistent between each other.

Magnetic properties

Generally, there are two approaches that can be followed for studying the magnetic properties of surface slabs (such as LSMO) - the cluster and the periodic approaches. In the former, the magnetic interactions between neighbouring Mn ions are evaluated

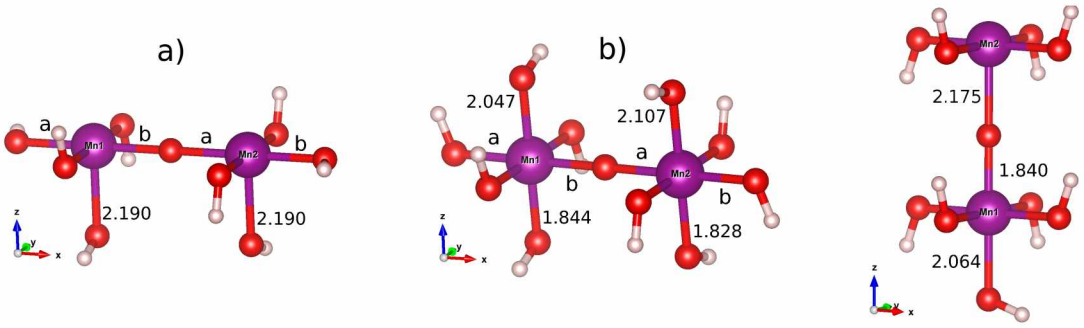

Figure 4.24: a) model for the top-layer dimers, the Mn-O bonds in the xy-plane ana perpendicular to the Mn-Mn axis are kept 1.950 Å; b) model for the middle-layer dimers, the Mn-O bonds in the xy-plane are kept 1.945 Å; c) model for the interlayer interaction (top and middle), the Mn-O bonds in the xy-plane are kept 1.950 Å.

through manganese dimers, where only the Mn ions and the oxygen atoms with which it forms bonds are taken into consideration. The geometry is maintained as the one obtained after optimization and the oxygen atoms are saturated to OH^- groups. Such approach can give a detailed picture of how the different geometry values affect the exchange between the Mn ions. On the other hand, the periodic approach takes into consideration the magnetic interactions in the crystal phase.[168] It is useful to determine the magnetic state of the surface phase as a whole. In this work, only the [MnO_2] 7×7×3 has been studied by means of simplified dimer models according to the cluster approach and the results are presented in the following section.

In order to verify the superexchange magnetic contributions arising from the different Mn^{n+}/Mn^{m+} couples in the [MnO_2] 7×7×3 surface model where there is a sort of Mn^{3+} segregation in the top layer with a correspondent Mn^{4+} accumulation in the layer below, several Mn dimers structures have been extrapolated and for them the Js have been computed through the Broken Symmetry approach. The basis sets and functional are the same used for the surface models. A more precise SCF convergence criterion of 1×10^{-7} Hartree has been used. The considered dimers are taken to mimic both intra- and inter-layers exchange interactions (top and middle). In the former case, there are essentially three dimers for the top layer and two – for the middle layer, where the two Mn ions are penta-coordinated (hexa-coordinated) by one bridging O^{2-} and 8 OH^- groups (one bridging O^{2-} and 10 OH^-), for the top and middle layers, respectively. These models differ in the lengths of the Mn-O bonds marked as a and b, whose values are reported in Table 4.16 and Table 4.17. To mimic the exchange interactions in the interlayer, a dimer geometry has been adopted as well, where one Mn ion, belonging to the top layer, is penta-coordinated while the other (inner layer) is hexa-coordinated. The Mn-O-Mn angle has been considered to be 180 °. The real ones for this model surface are 169.7 ° for the top layer, 171.0 ° for the middle one, and 177.4 ° between the top and bottom Mn planes.

The J values obtained (see Tables 4.16, 4.17 and 4.18), computed with a pure density functional with no addition Hartee-Fock exchange correction, are overestimated but all are antiferromagnetic. Positive J values stand for antiferromagnetic interaction, while negative – for ferromagnetic one.

Taking into consideration the results obtained for the exchange interactions in the top

Table 4.16: Values for the exchange interaction J (cm^{-1}) for the dimers of the top layer of the optimized [MnO_2]-surface

a (Å)	b (Å)	Mn^{3+}-Mn^{3+}	Mn^{3+}-Mn^{4+}	Mn^{4+}-Mn^{4+}
1.950	1.950	107	−269	−139
1.940	1.960	107	−257	−139
1.930	1.970	107	−182	−136

Table 4.17: Values for the exchange interaction J (cm^{-1}) for the dimers of the middle layer of the optimized [MnO_2]-surface

a (Å)	b (Å)	Mn^{3+}-Mn^{3+}	Mn^{4+}-Mn^{3+}	Mn^{3+}-Mn^{4+}	Mn^{4+}-Mn^{4+}
1.950	1.950	−370	−361	−346	142
1.925	1.935	−301	−296	−277	159

Table 4.18: Values for the exchange interaction J (cm^{-1}) for the dimers, measuring the exchange interaction between the top and the middle layers of the optimized [MnO_2]-surface

Mn1-Mn2	J (cm^{-1})
Mn^{3+}-Mn^{3+}	226
Mn^{4+}-Mn^{3+}	−138
Mn^{3+}-Mn^{4+}	−1277
Mn^{4+}-Mn^{4+}	−796

and middle layer and the calculated spin densities, we can expect that, there will be a prevailing intralayer antiferromagnetic behavior in both layers. This is due to the larger concentration of Mn^{3+}-Mn^{3+} (Mn^{4+}-Mn^{4+}) possible interactions in the top (middle) layer. The predominant interlayer interaction, however, is expected to be ferromagnetic, as the dimers Mn^{4+}-Mn^{3+} would be much more than the Mn^{3+}-Mn^{3+} ones.

4.3.3 Studies of possible contaminants of the surface

When LSMO surfaces are grown experimentally, they are subjected to an annealing or chemical cleaning procedure. The goal is to dispose of any possible contaminations. However, even after these procedures, some residual contaminants could remain. For this reason, several model structures for contaminants on the LSMO surfaces have been tested with the idea to construct surfaces afterwards and to evaluate their eventual influence on the properties of the surfaces.

Several other studies have been also dedicated to different kind of contamination. The most favourable sites for the (MnO_2)-termination layer are found to be atop the Mn ions for oxygen[169,170] and the surface oxygen for CO_2 adsorption.[171] However, Hammami et al. suggest that this termination layer is more stable, due to the larger rumpling and thus it is less reactive.[171] Indeed, they suggest that the CO_2 is more strongly adsorbed on the (LaO) termination layer, since it is more basic. This is supported by infrared studies on $LaMnO_3$ showing bands, corresponding to free carbonate ions and bidentate carbonate weakly bonded to the surface, which also ascribe the strong interaction of $LaMnO_3$ with CO_2 to the high basicity of La^{3+}.[172] In addition, in the (LaSrO) termination layer, the best sites for oxygen adsorption are found to be the hollow cites[170] and also the bridge

site between two La atoms.[169]

Adsorption studies on $SrTiO_3$ can be useful to predict the behaviour of contaminants on a Sr-segregated surface. It is shown that the SrO in reaction with the air forms $SrCO_3$.[173] Indeed, for low coverages (below 0.2), the CO_2 bonds strongly to the (SrO) layer.[174] However, Baniecki et al. claim that the resulting structure is more similar to that of CO_2^- in C_{2v} symmetry, than the CO_3^{2-} one in D_{3h}.[174] Also a weakly bond structure is present where the CO_2 molecule binds two Sr atoms.[174] Alexandrov et al. suggest the adsorption of an oxygen adatom in bridge position between surface oxygen ions and adjacent metallic one. This strong chemisorption is caused by the formation of a surface molecular peroxide ion. They also claim a weak adsorption on a defect-free case.[175]

In this theoretical study, more attention is given to the adsorption of different contaminants with respect to the spin density of the underlying Mn ions. The two termination layers have been studied separately.

In the case of [LaSrO] termination layer, only the possibility of CO_2 adsorption on the surface oxygen has been evaluated. A 3×3×3 [LaSrO] slabs have been studied in agreement with the computational protocol for the surfaces. First, it has been worked with a homogeneous distribution of the Sr atoms, and then with segregated slabs.

The most stable structures are found to be at low coverage. In the case of 0.3 (see Figure 4.25a)), the CO_2 forms a CO_3^{2-}-like group, where the surface oxygen has been extracted from the (LaSrO) layer. In order to discriminate between the different models, the energy of formation for each one has been calculated according to equation 4.9. This structure is very favourable since it shows an energy gain of 54.3 kcal/mol per CO_2 molecule. Such geometry is not stable for a full coverage, so in that case some of the CO_2 molecules disorb from the surface, leaving others chemisorbed. However, the star-like shape is hinted, but the surface oxygen does not leave the (LaSrO) layer (see Figure 4.25b)). When such "middle shape" is tried on full coverage, no disorption takes place, but the formation energy per molecule remains low - 8.97 kcal/mol. On the other hand, the 0.7 coverage, results in more stability since the energy gain goes to 24.4 and 29.3 kcal/mol for the structures in Figure 4.25 d) and e).

$$E_{form} = \frac{(E_{ads} - E_{slab} - N_{CO_2} * E_{CO_2})}{N_{CO_2}} \tag{4.9}$$

The segregated surface gives similar results, where at the adsorption of only 3 molecules is more energetically favourable (formation energy 62.5 kcal/mol) that the full coverage (formation energy 24.3 kcal/mol). Moreover, the latter does not guarantee the lack of disorption, as it can be observed in Figure 4.26.

At this moment of the study, no definite model has been proposed and investigated for a contaminated [LaSrO] and [LaSrO-grad].

For the study of [MnO_2]-termination, in agreement with previous studies, two atop sites for adsorption are considered - the Mn and O ions. The surfaces slab has been approximated to simple model monomers and dimers, respectively (see Figure 4.27), where the Mn-O bond lengths have been fixed to the average ones, found in the [MnO_2] surface, or 1.950 Å for the equatorial ones and 2.190 Å for the axial one.

Since the presence of carbon is expected to be found, the main contaminants studied comprise CO and CO_2 molecules adsorbed on the Mn ions. In the latter, the C-atom is on the metal ion, while the CO_2 is positioned vertically with an oxygen atom atop the Mn ion. In addition, the possibility of adsorbing a H_2O molecule or O atom have also been considered. All possible oxidation numbers have been taken into consideration, since on

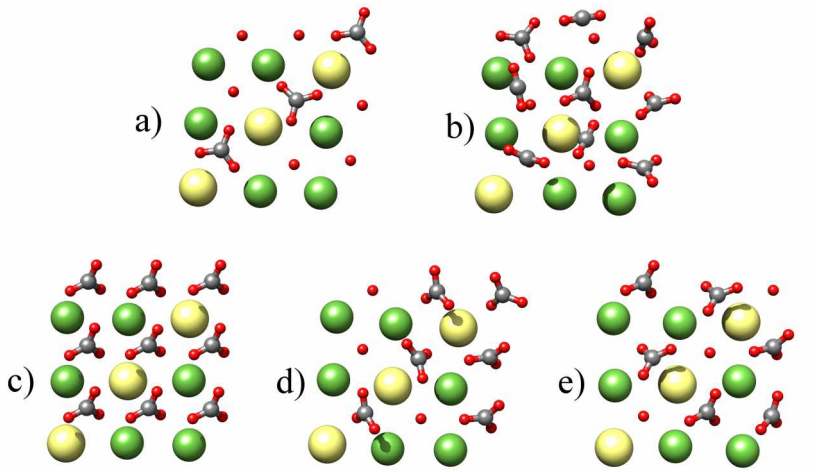

Figure 4.25: (LaSrO)-termination slabs with different levels of contamination with CO_2 with the following E_{form}: a) 54.3 kcal/mol; b) 20.7 kcal/mol; c) 8.97 kcal/mol; d) 24.4 kcal/mol, and e) 29.3 kcal/mol; the legend of the colours is the following - Sr (yellow), La (green), O (red), C (grey).

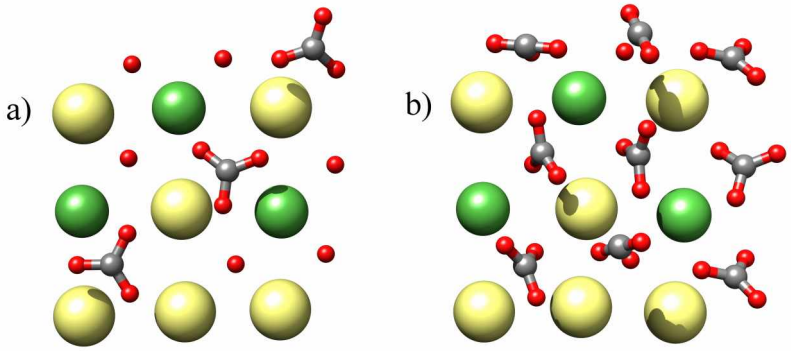

Figure 4.26: Sr segregated (LaSrO)-termination slabs with different levels of contamination with CO_2 with the following E_{form}: a) 62.5 kcal/mol; b) 24.3 kcal/mol; the legend of the colours is the following - Sr (yellow), La (green), O (red), C (grey).

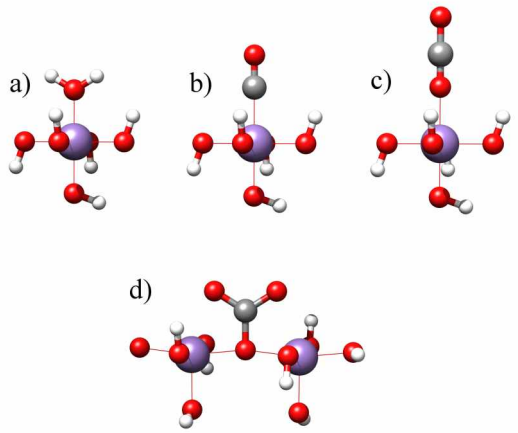

Figure 4.27: Initial geometry for the monomers with a) H_2O, b) CO, and c) CO_2 adsorbed on the Mn ions; d) The dimer with CO_2 adsorbed on the oxygen of the (MnO_2) layer after the geometry optimization.

the top layer are present both Mn^{3+} and Mn^{4+}. The Mn^{3+} and Mn^{4+} are in their high spin state. The presence of Mn^{2+} on the surface has been proven experimentally,[162,163] so the effect on the contaminants of having it is something not to underestimate. Therefore, also the presence of Mn^{2+}, both in low and high spin state, in the top layer has been considered. The model monomers and dimers have been subjected to geometry optimization, where all atoms have been kept fixed apart, from the contaminant ones.

The results regarding the monomers reveal that only the CO molecule remains attached to the majority of the Mn ions, while all the other dissociate (see Table 4.19). The oxygen atom on the Mn ion has been studied only for the case of Mn^{4+}.

On the other hand, the CO_2 is also adsorbed on the surface oxygen in a dimer. The initial structure of linear molecule fast transforms into a CO_3^{2-}-like group, in agreement with other studies and irrespective of the oxidation state of the Mn ions.

Transferring this result on a slab, a 7×7×3 [MnO_2] surface has been modelled and optimized geometrically with 24 CO_2 molecules attached by the C-atoms to the oxygen in the top layer, in a similar manner as the test dimer. The optimization of the geometry follows the same computational protocol as the one without any contamination. In the resultant structure, the rumpling of the oxygen atoms is even more highlighted with the adding of the CO_2 molecules (see Table 4.20), which leads to even lower Mn-O-Mn angle, the average value is 162.9 ° (with variations between 147 to 179 °) against 169.7 °. Slight changes are also noticed in the out-of-plane Mn-O distances (see Table 4.21). The average C-O bond with the oxygen atom of the (MnO_2) layer is found to be 1.38 Å, in agreement with the theoretical 1.41 Å[171] and the experimental one, 1.29 Å, for the CO_3^{2-}-group.

4.3.4 Conclusion

In conclusion, the theoretical protocol gives satisfactory results regarding the properties of the LSMO surface independently from the slab thickness. Therefore, it is acceptable to assume that the 7×7×3 slab is a reliable model for the study of $Fe_4(dpm)_6$ adsorption. At this level of study, the surfaces will be considered as clean with no contaminations. Studies on the influence of the contaminations on the adsorption properties of SMM

Table 4.19: The different contaminants that have been presented with respect to the oxidation number of the Mn ions. The + sign means that after the geometry optimization, the correspondent group has remained attached, while the − sign means it has not.

Monomers						
	Mn spin	**O**	**OH**	**H_2O**	**CO**	**CO_2**
Mn^{2+}	5/2		−	−	−	−
	1/2		−	−	+	−
Mn^{3+}	4/2		−	−	+	−
Mn^{4+}	3/2	+			+	−
Dimers						
	Mn spin			**CO_2**		
Mn^{2+}-Mn^{2+}	5/2			+		
	1/2			+		
Mn^{3+}-Mn^{3+}	4/2			+		
Mn^{4+}-Mn^{4+}	3/2			+		

Table 4.20: Rumpling parameters r, calculated as $r = z(O) - z(Mn)$.

	[MnO_2]	**[MnO_2-CO_2]**
r_{top} (Å)	−0.17	−0.27
r_{middle} (Å)	−0.14	−0.1
r_{bottom} (Å)	−0.08	−0.7

Table 4.21: Average interlayer separation in Å, calculated as the average between the planes of the Mn atoms and that of the axial oxygen atoms in the successive [LaSr]-planes.

	[MnO_2]	**[MnO_2-CO_2]**
Δ_{Mn3-O3}	2.174	2.218
Δ_{O3-Mn2}	1.838	1.866
Δ_{Mn2-O2}	2.064	2.055
Δ_{O2-Mn1}	1.908	1.924
Δ_{Mn1-O1}	1.907	1.921

Table 4.22: Distribution of the Mn spin densities for the [MnO_2] 7×7×3 slabs with and without CO_2.

Layer	**[MnO_2]**	**[MnO_2-CO_2]**
Top	3.88	3.76
Middle	3.32	3.41
Bottom	3.44	3.52
Average	3.54	3.56
Bulk	3.56	

cluster will be considered in future plans.

CHAPTER

FIVE

MAGNETIC MOLECULES ON SURFACES

In the perspective to check if they are suited for building blocks in spintronic devices, it is very important to understand the SMM behaviour on substrates. For this reason, a reliable computational approach for the study of hybrid systems, such as molecules on surfaces, is of great importance. However, it is not straightforward, since the reproduction of the properties of both structures is required. In the previous chapters, it has been shown that good agreement is achieved between the theoretical results and the experimental data both for isolated magnetic clusters and different kind of surfaces. In this chapter will be shown the results obtained by applying the computational protocols presented in the previous part of this thesis on hybrid systems.

The simulation of an adsorbed system has also its own further challenges, so there are some things to be considered beforehand. First, the way the molecules are deposited on the surface should be considered. For atoms and small molecules, the site preference is of great importance. This is not the case for larger clusters, where a preferred adsorption site can be hardly identified if present. The major factor is the way the cluster leans on the surface and whether the hydrogen atoms and π-systems can at their best efficiently interact with the surface. Moreover, working with smaller adsorbates permits to vary the coverage percentage, since it is not excessively expensive to simulate such systems. The SMM clusters are usually too big, so a simulation of more than one molecule would be computationally unaffordable at DFT level. Therefore, the coverage of the surface can be dealt with by varying the size of the slab, where the smaller the slab, the closer the adsorbed molecule is to its periodic image.

In addition, a consistent method of comparison between the isolated and adsorbed structures is necessary in order to take into account the differences that occur upon adsorption. The geometry changes in the structure on the surface are considered through the so-called extrapolated cluster. It stands for the optimized adsorbed system, treated as isolated, i.e. without the underlying surface. In order to evaluate the electronic effects that arise from the substrate, a direct comparison between the bulk and adsorbed system is needed. In such cases, the DFT+U method is necessary, due to its accuracy and transferability, as verified and discussed in the previous chapters.

Few papers are appeared so far about the characterization both at experimental and theoretical level of different single-molecule magnets deposited on non-magnetic surfaces.[20,21,24,176–179] For instance, Barraza-Lopez et al. have studied the adsorption of Mn_{12} SMM on Au(111) surface at two levels of theory - DFT[180] and DFT+U.[181] In both cases, they have found that the molecule weakly couples with the surface and the charge

transfer occurs from the surface to the molecule mainly through linker molecules.[180]

There are also studies of SMMs on magnetic surfaces.[182] For instance Park studied the Mn_{12} on Ni(111) at DFT and DFT+U level and found that the molecule prefers antiferromagnetic coupling with the surface.[178] In a recent experimental study[16] of a double-decker molecule ($TbPc_2$) on a ferromagnetic surface, it is suggested that the magnetic exchange coupling parameters describing the molecule-substrate magnetic interaction can vary depending on the amount of charge density transferred at the molecule-surface interface.

However, the few theoretical studies appeared up to now of adsorbed SMM confine themselves to relatively easy cases of metallic surface models.

This work is concentrated on the study of $Fe_4(dpm)_6$ on three different surfaces - two non-magnetic Au(111) and CuN; and one magnetic LSMO, where two termination layers are considered. There are two aims set - the first one is to confirm the reliability of computational protocol for the description of SMMs on various surfaces, and the second is to discriminate any different behaviour and dependencies on the substrate.

5.1 $Fe_4(dpm)_6$@Au(111)

The theoretical model used for the simulation consists of one $Fe_4(dpm)_6$ cluster deposited on Au(111) surface (see Figure 5.1). An orthorhombic periodic simulation cell with dimensions (23.09×24.98×40.00) Å^3 has been chosen, guaranteeing a distance between the periodic replica of the cluster along x and y of about 7 and 9 Å, respectively. In order to avoid any possible interaction with the periodic image along the z direction, an empty space of about 20 Å has been introduced.

The same computational protocol for the geometry optimization and study of the properties of the two systems, when investigated separately, has been followed (see Chaprter 3 and 4). For this hybrid system, smearing of the occupational numbers around the Fermi level by the Fermi-Dirac distribution has been used with a broadening (electronic temperature) of 1500 K to account for the metallicity of the surface and to significantly improve the convergence.

The optimized geometries have been assembled together and let further relax. A critical point remains the disposition of the cluster upon adsorption. One of the presumably most stable geometries as a starting point for the optimization has been chosen. In details, the cluster leans on the surface with one of its benzene rings and two *t*Bu-groups coming from two dpm^- ligands, thus providing a large number of interactions between the hydrogen atoms of the ligands with the underlying gold atoms.

The changes in geometry, magnetic and electronic properties will be discussed in the following subsections.

Geometry

The geometry optimization has led to very small changes in the structure of the Au surface, which include only slight increase in the inter-plane separation (see Table 5.1). Similarly, the molecule has revealed to be rigid enough to keep its core geometry almost unchanged (see Table 5.2). Upon deposition and after optimization, the $Fe_4(dpm)_6$ maintains its integrity and does not exhibit severe distortions at this level of theory. Its optimized structure on Au(111) is reported in Figure 5.1.

In detail, the symmetry of the cluster is maintained to a great extent, as it could be noted from the Fe1-Fe3 and Fe1-Fe4 distances. The average ⟨Fe-O-Fe⟩ bridging angle

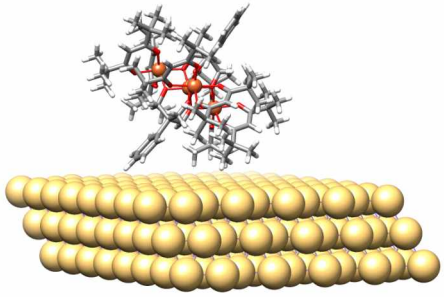

Figure 5.1: A side view of the simulation model $Fe_4(dpm)_6$ on Au(111).

Table 5.1: Interlayer separation along z of the Au(111) surface.

Δz(layers) (Å)	Au(111)	$Fe_4(dpm)_6$@Au(111)
(top-middle)	2.624	2.627
(middle-bottom)	2.623	2.624

also remains almost unchanged, which is an indicator for similar magnetic properties with respect to the isolated $Fe_4(dpm)_6$.[56]

The easy axis of the magnetization, taken as the normal to the plane containing the four iron ions, has been evaluated to form an angle of 34.4° with the normal to the surface. This value is close to the one found for a thioacetyl functionalized analogue, chemically grafted to the Au(111) surface[20] and is strongly due to the structure of the cluster.

The physisorption energy of $Fe_4(dpm)_6$ ($-40.3\,\mathrm{kcal\,mol^{-1}}$), where distance between the molecules and the slab is 2.475 Å, is due mainly to the large number of favourable Au-H and π interactions of one phenyl group, whose contribution is however expected to be overestimated by the employed D3 energy dispersion corrections.[36]

Magnetic properties

The evaluation of the changes in the $Fe_4(dpm)_6$ magnetic structure upon adsorption have been performed using the Broken Symmetry (BS) formalism (see Chapter 2) in agreement with the studies of the isolated cluster. Again, threefold symmetry is assumed, where the J_1 and J_2 account for nearest-neighbour and next-nearest neighbour interactions, respectively (see equation 2.26).

Two approaches have been used to evaluate the exchange coupling constants. The first one is by using a hybrid functional. It is well known that the inclusion of HF exchange is necessary to accurately evaluate magnetic interactions, so PBE0 functional[37] has been applied to the optimized with revPBE geometries of $Fe_4(dpm)_6$ structures in the gas phase and adsorbed on gold. However, in the latter case the entire system is computationally too demanding at this level of approach. The exchange coupling constants for the adsorbed scenario have been thus computed only on the geometry of the cluster already optimized on the gold surface at the revPBE level on the extrapolated geometry, i.e. removing the gold surface without any further relaxation.

The second approach includes the use of the DFT+U. As already stated in Chapter

Table 5.2: Bond lengths and angles of the isolated $Fe_4(dpm)_6$ and the one deposited on Au(111).

	X-ray	**$Fe_4(dpm)_6$**	**$Fe_4(dpm)_6$@Au(111)**
		Bonds (Å)	
Fe1-Fe2	3.0780(8)	3.139	3.134
Fe1-Fe3	3.0726(6)	3.161	3.171
Fe1-Fe4	3.0726(6)	3.160	3.172
Fe2-Fe3	5.2925(7)	5.402	5.399
Fe3-Fe4	5.3880(1)	5.579	5.591
Fe2-Fe4	5.2925(7)	5.399	5.420
Fe1-O1'	1.9801(19)	2.011	1.994
Fe1-O2'	1.9650(18)	2.005	1.979
Fe1-O3'	1.9813(19)	2.019	2.014
Fe1-O1	1.9801(19)	2.020	2.017
Fe1-O3	1.9650(18)	2.004	1.982
Fe1-O2	1.9813(19)	2.018	2.024
Fe2-O1'	1.9718(9)	2.006	2.039
Fe2-O4	1.995(2)	2.039	2.031
Fe2-O4'	2.0321(19)	2.089	2.070
Fe2-O1	1.9718(9)	2.009	2.002
Fe2-O5'	1.995(2)	2.039	2.045
Fe2-O5	2.0321(19)	2.090	2.073
Fe3-O2'	1.9784(19)	2.020	2.048
Fe3-O6	1.9853(19)	2.056	2.025
Fe3-O6'	2.004(2)	2.059	2.060
Fe3-O7	1.993(2)	2.036	2.002
Fe3-O7'	1.9909(19)	2.071	2.073
Fe3-O2	1.9718(18)	2.022	2.027
Fe4-O3'	1.9718(18)	2.018	2.035
Fe4-O3	1.9784(19)	2.034	2.055
Fe4-O9'	1.9853(19)	2.052	2.031
Fe4-O9	2.004(2)	2.058	2.058
Fe4-O8'	1.993(2)	2.035	2.022
Fe4-O8	1.9909(19)	2.085	2.062
		Angles (°)	
Fe2-Fe1-Fe3	118.74(1)	118.09	117.83
Fe2-Fe1-Fe4	118.74(1)	117.98	118.52
Fe3-Fe1-Fe4	122.51(2)	123.93	123.64
⟨Fe-O-Fe⟩	102.23(17)	102.93	103.02
Fe3-Fe1-Fe2-Fe4	180.00	179.90	178.57
γ	68.80	70.60	69.80

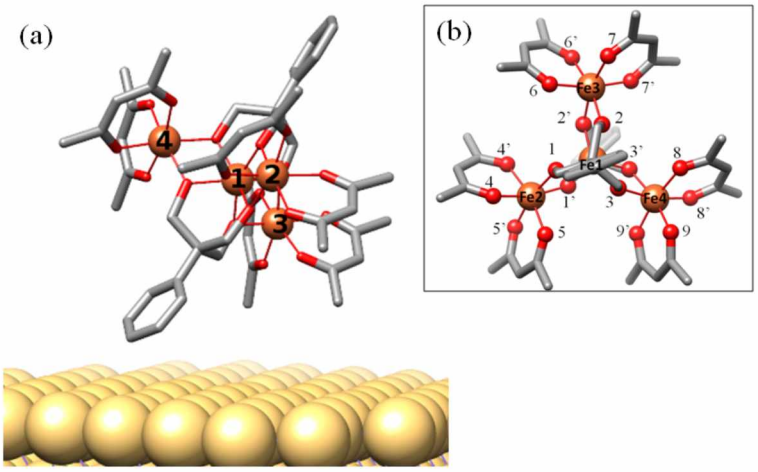

Figure 5.2: A visual representation of the bonds presented in Table 5.2.

2, it is less demanding, maintains the accuracy of the hybrid approach and allows the investigation of the whole molecule-plus-substrate system. However, being a parametric approach, the choice of the U parameters is critical for a correct description of the electronic structure. The best set of values have been found to be U(Fe)=4.1 eV and U(O)=3.0 eV (see Chapter 3). In addition and in agreement with previous studies,[181] the U parameter has been also used for gold atoms ($5d$ orbitals). It has been varied in order to get the best agreement between the computed TDOS for the gold slab and the clean gold surface UPS (HeII)[183] experimental spectrum (see Figure 5.3). The computed spectra from 0.2 up to 0.6 eV are substantially equivalent and are in a relatively good agreement with the experiment. For this reason they have been considered in the calculations of the magnetic properties.

The exchange coupling constants evaluated with the two approaches are presented in Table 5.3. As already evident from the geometrical data, the J values support the evidences of a strong rigidity of the magnetic core upon adsorption at both levels of theory.

As far as the cluster on the surface is concerned, the revPBE+U results confirm that the overall scenario of a dominant antiferromagnetic J_1 interaction is preserved, with a spin ground state S=5 separated by $35 \div 56$ cm^{-1} from the excited S=4 states, depending on the chosen U(Au) parameter. Such results for the complex $Fe_4(dpm)_6$@Au(111) system indicate only minor effects induced by the interaction with the substrate. Interestingly, both approaches employed here (the extrapolated molecule from the surface and the full system treated at DFT+U level) confirm substantial conservation of intramolecular antiferromagnetic coupling upon grafting. In details, a slight increase of the ΔE is expected when larger U(Au) values are considered. These results are in agreement with the experimental findings, which testify of maintenance of the magnetic properties upon deposition.[184]

The magnetic anisotropy, not included in this treatment, is also not expected to vary significantly due to the minor geometrical modifications and almost negligible electronic effects arising from the proximity of the metallic substrate.

In addition, no significant changes are observed in the spin densities on the four Fe ions, when they are in the isolated cluster, as well as in the adsorbed one on Au(111), which once more confirm the weak interaction with the Au(111) surface (see Table 5.4).

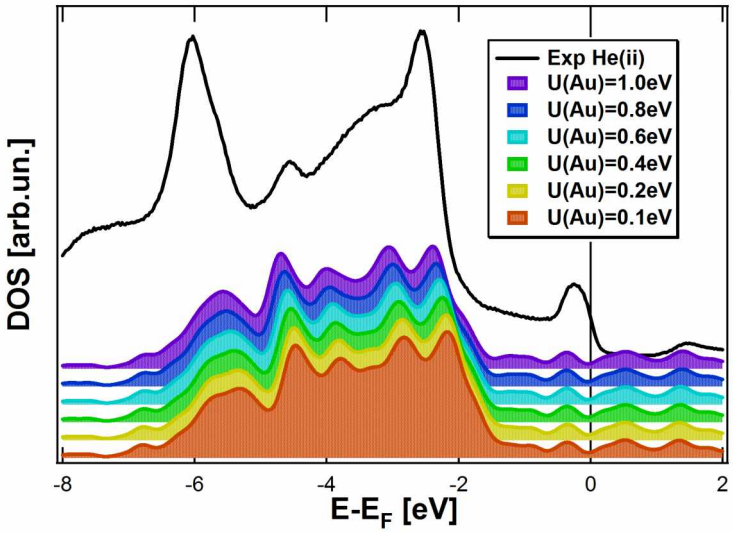

Figure 5.3: Experimental UPS spectrum of Au(111) compared with the computed TDOS of the gold slab with several U values

Table 5.3: Exchange coupling constants (reported in cm^{-1}) for the $Fe_4(dpm)_6$ on the Au(111) surface. The U parameters are in eV.

	PBE0			J_1	J_2	$\Delta E_{5,4}$*
X-ray				14.4	0.3	34
Optimized				13.8	0.2	33
Extrapolated				14.7	0.1	36
	U(Fe)	**U(O)**	**U(Au)**			
X-ray	4.1	3.0	-	17.0	0.4	40
Optimized	4.1	3.0	-	16.7	0.3	40
Extrapolated	4.1	3.0	-	17.9	0.2	43
	Experiment			16.37(12)	0.29(11)	42
@Au(111)	4.1	3.0	-	15.0	0.4	35
	4.1	3.0	0.2	15.3	0.3	36
	4.1	3.0	0.4	15.5	0.4	36
	4.1	3.0	0.6	18.7	-1.2	56

* Energy gap between the ground S=5 and the two first excited states S=4 states.

Table 5.4: Spin densities for the four Fe-ions in $Fe_4(dpm)_6$ on the Au(111) surface, calculated with revPBE+U method. The U parameters are in eV.

$Fe_4(dpm)_6$	**U(Fe)**	**U(O)**	**U(Au)**	**Fe1**	**Fe2**	**Fe3**	**Fe4**
X-ray	4.1	3.0	-	-4.35	4.37	4.38	4.38
Optimized	4.1	3.0	-	-4.36	4.38	4.38	4.38
Extrapolated	4.1	3.0	-	-4.36	4.38	4.38	4.38
@Au(111)	4.1	3.0	-	-4.36	4.38	4.38	4.38
	4.1	3.0	0.2	-4.36	4.38	4.38	4.38
	4.1	3.0	0.4	-4.36	4.38	4.38	4.38
	4.1	3.0	0.6	-4.36	4.38	4.38	4.38

Electronic properties and STM images

The DOS of the isolated and extrapolated clusters present the same contour lines both at PBE0 and revPBE+U levels of theory in agreement with the small changes that occur upon optimization of the SMM on Au(111) surface (see Figure 5.4). The PDOS maintain the characteristic shape even on the surface. An insignificant rigid TDOS shift of 0.06 eV of the extrapolated cluster with respect to the one that accounts for the surface as well is observed, which can be considered as the fingerprint for weak adsorption and evidence for the interaction with the Au states (see Figure 5.5 (right)). The addition of U parameter on the Au atoms does not change the shape of the TDOS, although a further shift of 0.06 eV to the lower-lying energies with respect to U(Au)=0 eV is present due to the inclusion of the on-site correction (see Figure 5.5).

On the basis of the optimized structure it has been possible to simulate an STM image of the $Fe_4(dpm)_6$ molecule on Au(111). Due to the low conductivity of the ligand shell a quasi-spherical multi-lobed structure is visible in line with the experiment, though the sub-molecular resolution is much poorer than for flat and/or with more symmetry elements molecules like $TbPc_2$. An average diameter of ca. 1.9 nm can be estimated from the computed image, in agreement with the experimental STM values.[184] However, along with spherical objects, the sample shows domains with rather different appearance whose internal structure could not be resolved (see Figure 5.6). Their height (0.30±0.05 nm) suggests that they cannot be associated with $Fe_4(dpm)_6$ molecules but rather with smaller units, either contaminants or fragments. A partial decomposition of the cluster during the sublimation process cannot be ruled out. Possible hints about the structure of these fragments will be investigated through a study of $Fe(dpm)_3$ evaporated on Au(111). Indeed, this molecule is suggested to be contaminant in thin films of $Fe_4(dpm)_6$,[58] therefore, its deposition will be investigated in the next subsection.

5.1.1 Contaminants

The $Fe(dpm)_3$ has been evaporated on Au(111) experimentally. The STM images along with spherical objects similar to the molecule, confirm the presence of contaminants also in this system, which seem to be similar to those observed in the case of $Fe_4(dpm)_6$. These objects are highly symmetric building-blocks, characterized by a four-fold symmetry (see Figure 5.7 (right)). Moreover, both islands and isolated objects are 0.29±0.02 nm high, therefore confirming the common nature of their building-blocks.

First, the $Fe(dpm)_3$ has been simulated on Au(111) in a (17.3×15.0×40.0) $Å^3$ simula-

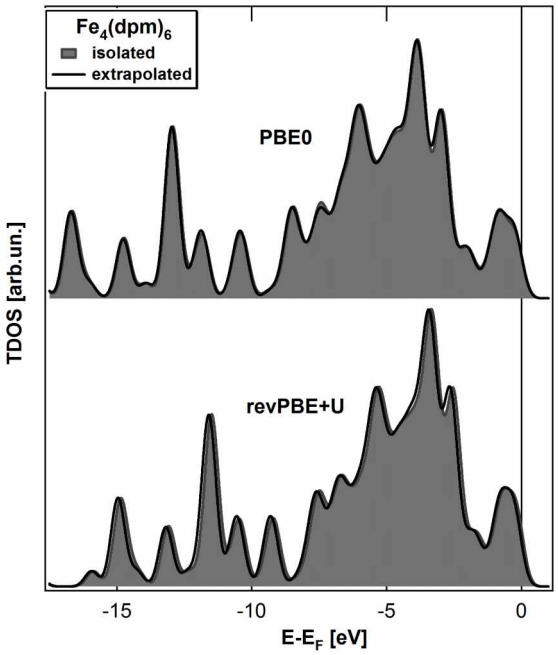

Figure 5.4: Comparison between the density of states of the isolated cluster and the extrapolated one at PBE0 (top) and revPBE+U (bottom) levels of theory. The Gaussian width, σ, is 0.35 eV.

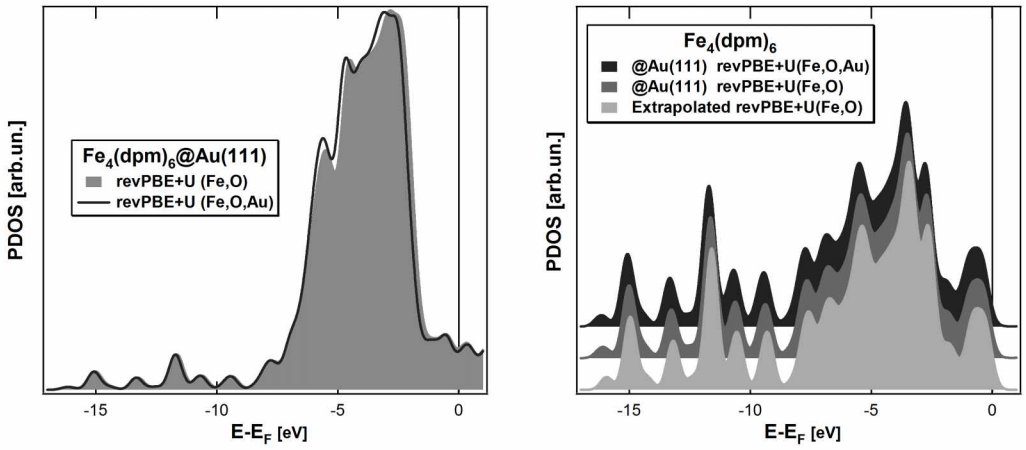

Figure 5.5: TDOS of the $Fe_4(dpm)_6$@Au(111) calculated with U(Au)=0.6 eV and without U parameter on Au (left), the σ is 0.2 eV; comparison between the PDOS of $Fe_4(dpm)_6$ on Au(111) and the extrapolated one (right), the σ is 0.35 eV.

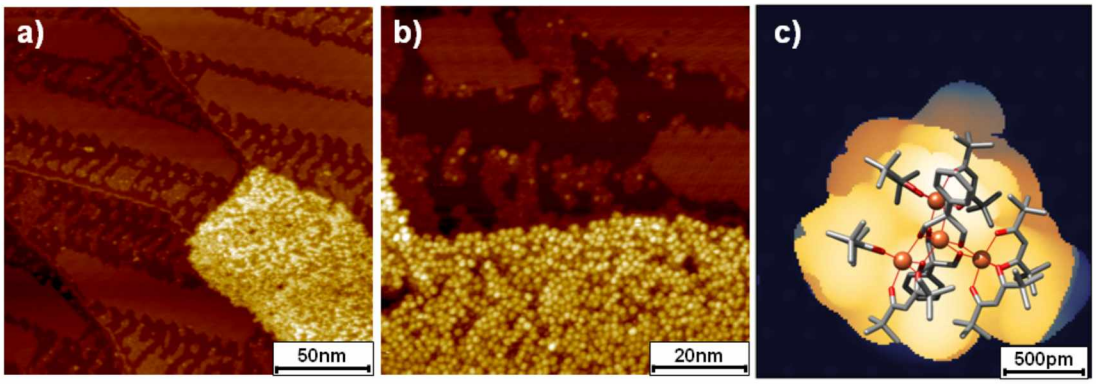

Figure 5.6: STM images acquired at 30 K for $Fe_4(dpm)_6$ sublimated on Au(111) single crystal. (a) Large scale image of the 0.2 ML sample (135×135) nm^2, 3 pA, 2.5 V). (b) Same sample investigated at higher magnification ($80\times80\,nm^2$, 10 pA, 2.0 V). (c) Calculated STM image of $Fe_4(dpm)_6$ adsorbed on Au(111) with a 2 V bias (occupied states). The $Fe_4(dpm)_6$ has been superimposed to be more informative on the different shiny parts of the image.[184]

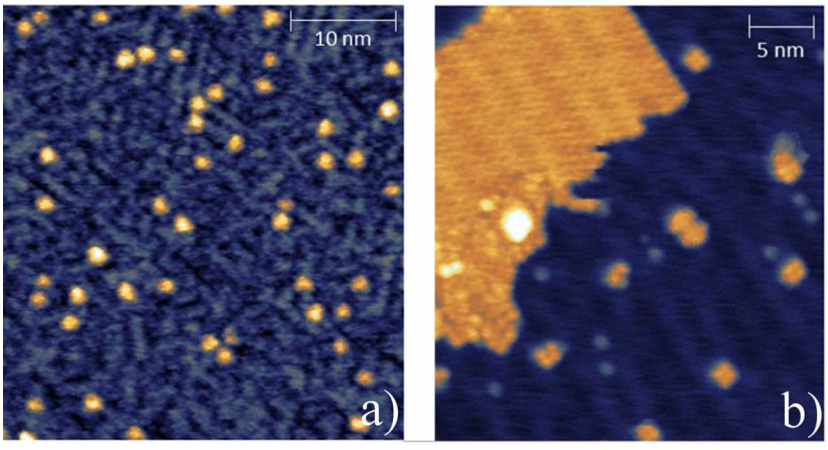

Figure 5.7: STM image of Au(111) surface after exposure to $Fe(dpm)_3$: (a)Size = $45\times45\,nm^2$, Bias=1.5 V (occupied states), I=10 pA. (b) Size=$34\times34\,nm^2$, Bias=-2 V (empty states), I=5 pA.[185]

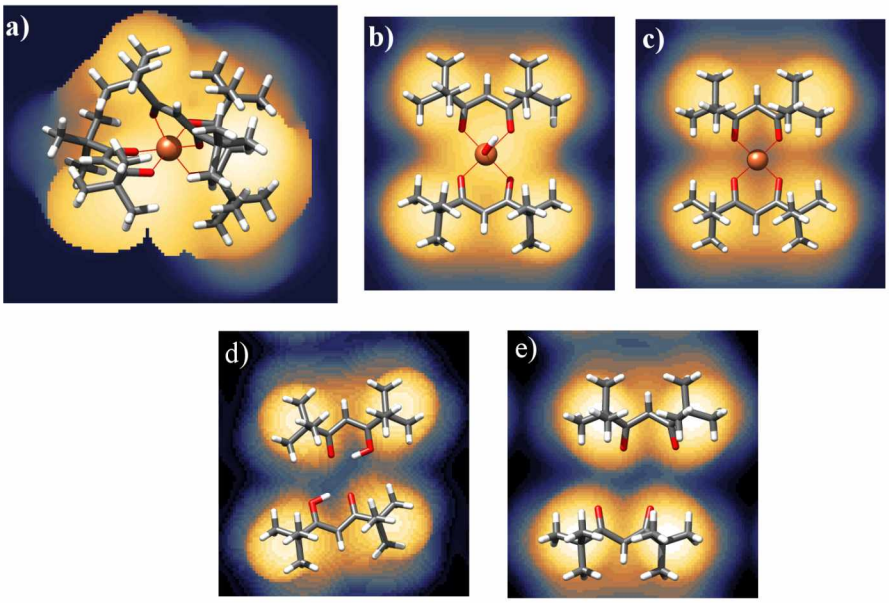

Figure 5.8: STM images of the simulated models for contaminants at the experimental biases: a) $Fe(dpm)_3$; b) $FeOH(dpm)_3$, c) $Fe(dpm)_2$, d) $(Hdpm)_2$, and e) $(dpm)_2^{2-}$.

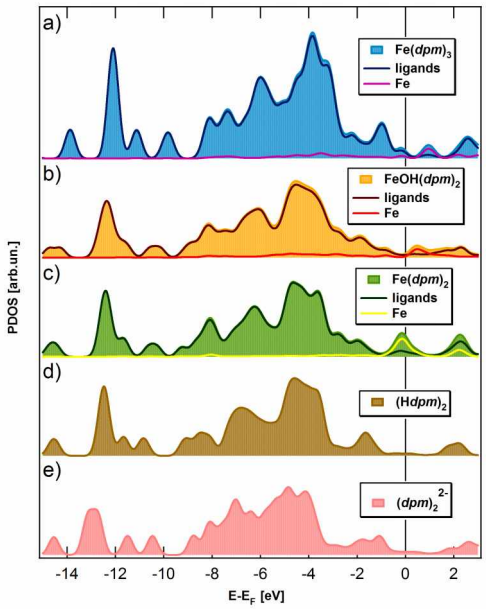

Figure 5.9: PDOS of the different fragments on Au(111): a) $Fe(dpm)_3$; b) $FeOH(dpm)_3$, c) $Fe(dpm)_2$, d) $(Hdpm)_2$, and e) $(dpm)_2^{2-}$. The σ is 0.3 eV.

tion cell. The same computational protocol as for $Fe_4(dpm)_6$ has been used with different functional (PBEsol) due to convergence problems. The comparison of the experimental topography with DFT-simulated STM images of the pristine $Fe(dpm)_3$ complex suggest some resemblance with the spherical spots visible in Figure fig:STM-Fe-dpm3. As for the tetra-lobed features (and probably the flat domains), these are not compatible with the calculated aspect for intact $Fe(dpm)_3$ molecules, suggesting that major structural changes occur on the gold substrate, i. e. decomposition.

To shed light on the unknown features, several molecular fragments have been theoretically investigated as possible intermediate or end products in the $Fe(dpm)_3$ decomposition process in the same simulation cell ($14.4\times15.0\times40.0$) $Å^3$): $(Hdpm)_2$, $(dpm)_2^{2-}$, $FeOH(dpm)_2$@Au(111), and $Fe(dpm)_2$@Au(111). Indeed, the high-spin (HS) Fe^{3+} ion in $FeOH(dpm)_2$ can undergo reduction to HS Fe^{2+} in $Fe(dpm)_2$ via $Fe(d^{z^2})$-Au(s) interaction and end up as low-spin (LS) Fe^{2+} with concurrent release of the OH^- group. $FeOH(dpm)_2$ considers a penta coordinated complex of HS Fe^{3+}, with two dpm ligands forming the basis of a square pyramid and the OH^- group acting as an apical ligand. $Fe(dpm)_2$ corresponds to a LS Fe^{2+} square planar complex. The optimized geometries and computed STM images are reported in Figure 5.8. The computed STM image of $Fe(dpm)_2$@Au(111) matches very closely the observed tetra-lobed units, with no detectable contribution from the iron d^{z^2} orbital. $FeOH(dpm)_2$@Au(111) also affords a tetra-lobed pattern, but with an extra spot in the middle. This shows that $FeOH(dpm)_2$ is unlikely to be the end product of $Fe(dpm)_3$ decomposition. On the other hand, the metal-less fragments are still tetra-lobed, but shifted one with respect to the other, which is not in agreement with the observed STM images.

Another method to determine the composition of the fragments is to study their electronic structure. The TDOS and PDOS for the fragments have been also computed and compared to the ones of pristine $Fe(dpm)_3$ in Figure 5.9. The largest differences are expected in the valence band region involving the coordination site (i.e. molecular Fermi region). Unfortunately, these features are hidden by the gold contribution in the experiment[185] and the inners level corresponding to the dpm ligands show minor differences. Therefore, a definitive assessment of decomposition products in terms of redox and spin state could only be achievable through a detailed synchrotron investigation on in-situ prepared samples.

In conclusion, the proposed computational protocol is found to be reliable and to give satisfactory results in agreement with the experimental ones. Therefore, it will be applied also in the study of the two other surfaces.

5.2 $Fe_4(dpm)_6$@CuN

The second studied surface is the CuN. Recently, there have been several studies of different metal atoms embedded in the structure of the surface, showing interesting properties.[102,186,187] In this framework, the deposition of a SMM as $Fe_4(dpm)_6$ on this surface is worth being investigated.

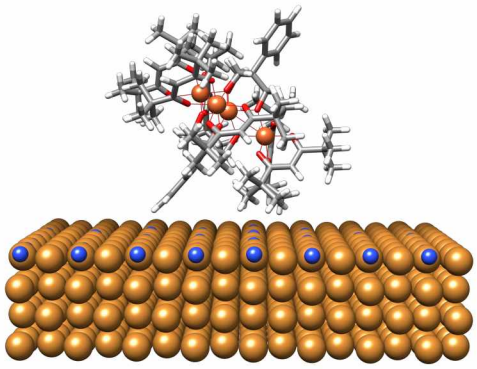

Figure 5.10: The optimized geometry of $Fe_4(dpm)_6$ on CuN.

The established general computational protocol from the previous section has been followed with some changes. As a result of the better reproduction of the surface geometrical experimental findings, the PBEsol functional has been used throughout the study of the $Fe_4(dpm)_6$ on CuN. In addition, the artificial mixing of states of the molecule and the surface at the Fermi level has led to convergence problems. Therefore, the DFT+U approach has been used to better reproduce the gap between the mixed states at E_F. As a result, the geometry optimization has been carried out at PBEsol+U level, unlike the previous case, where the approach is used on completely optimized structure. The same values of the U parameters, U(Fe)=4.1 eV and U(O)=3.0 eV, have been used as in Chapter 3. Such a choice has been done considering the robustness of the $Fe_4(dpm)_6$ upon adsorption and the transferable properties of the approach (see $Fe_4(dpm)_6$ and $Fe_4(pta)_6$).

The cluster has been positioned on the CuN surface by taking into consideration the relaxed geometry obtained for the Au(111) surface, i.e. leaning against the surface on two *t*Bu groups and the phenyl ring. It has been separated from its periodic images along x and y by 13 and 14 Å, respectively, while the vacuum region along z is 38 Å.

5.2.1 Geometry

Similarly to the Au(111) surface, the geometry optimization of the CuN with an adsorbed cluster has not led to significant changes in the inter-layer distances (Table 5.5). However, even though the average values remain almost constant, the deviation in the average shift along z (Table 5.6) has doubled for the N atomic layer and the topmost Cu one. Indeed, while the average distance between the hydrogen atoms and the surface is about 1.89 Å, the nitrogen atoms in close proximity to the ligand hydrogen atoms have moved inward with respect to the surface, thus increasing the distance to about 2.2 Å. Since the other

Table 5.5: Comparison between the geometry of the CuN surface with and without the $Fe_4(dpm)_6$.

Method	$dN1$ **(Å)**	Δ_{12} **(%)**	Δ_{23} **(%)**
CuN	0.27	6.70	1.75
$Fe_4(dpm)_6$@CuN	0.28	6.73	1.75

Table 5.6: Average shift of the corresponding atoms along z (Å) with the error for CuN surface with and without the $Fe_4(dpm)_6$.

Atomic layer	**CuN**	**$Fe_4(dpm)_6$@CuN**
N	5.707 ± 0.026	5.719 ± 0.058
Cu^{top}	5.439 ± 0.007	5.437 ± 0.014
Cu^{top-1}	3.558 ± 0.025	3.555 ± 0.023

N atoms have mainly remained in the same position, the observed fluctuation around the average value along z is mainly due to the N-H interactions.

The geometry of the $Fe_4(dpm)_6$ upon optimization with the functional PBEsol gives very good results with respect to the revPBE functional, which tends to lengthen the bonds. The addition of the U parameter in the optimization slightly worsens the geometry by shrinking the bonds even more and decreasing the angle ⟨Fe-O-Fe⟩, which is critical for the magnetic properties. However, the structural differences of the cluster on CuN with respect to the optimized isolated one remain small (1.4%). Therefore, the surface does not seem to significantly alter the core structure of the cluster. Similarly to the results found for the $Fe_4(dpm)_6$ deposited on Au(111), the angle between the easy axis of magnetization and the normal to the surface in the optimized structure is found to be 33.3 °.

5.2.2 Magnetic properties

The calculation of the magnetic properties has been done only at $+U$ level, since in the previous section its reliability has been proved. Indeed, within such framework the computed J values on the optimized structure are in good agreement with the experimental values (see Table 5.8). Differently from what observed for $Fe_4(dpm)_6$@Au(111) case, the distortions occurred to the Fe_4 core upon adsorption (see ⟨Fe-O-Fe⟩ in Table 5.7) induced a sizeable decrease of about 2 and 5 cm^{-1} in the J_1 and $\Delta E_{5,4}$ values, respectively.

Such trend has been also observed when the electronic effects of CuN are taken into account ($Fe_4(dpm)_6$@CuN). In such a case the effect is even stronger leading to a change in the ground state from S=5 to S=1. However, in order to verify the effect of the introduction of the U parameter also for Cu atoms, we perfomed two calculations with two sets of U values. Since the interacting topmost layers can be approximated essentially to Cu_3N, U(Cu)=5 eV[188,189] is applied to all Cu atoms in one case and in the other only to the two top atomic layers, while on the bottom two layers a U(Cu)=1 eV has been used.

The application of a uniform U across the slab gives the right ground state, even though the interaction with the surface remains strong. Indeed, the energy separation from the first excited state (S=4) is reduced up to about 23 cm^{-1}. The application of different U values on copper atoms depending on the different layer depth gives similar

Table 5.7: Bond lengths and angles of the isolated $Fe_4(dpm)_6$ and the one deposited on CuN.

$Fe_4(dpm)_6$	**X-ray**	**PBEsol**	**PBEsol+U**	**@CuN**
		Bonds (Å)		
Fe1-Fe2	3.0780(8)	3.078	3.029	3.000
Fe1-Fe3	3.0726(6)	3.076	3.052	3.041
Fe1-Fe4	3.0726(6)	3.096	3.006	3.004
Fe2-Fe3	5.2925(7)	5.316	5.297	5.063
Fe3-Fe4	5.3880(1)	5.367	5.262	5.529
Fe2-Fe4	5.2925(7)	5.337	5.177	5.028
Fe1-O1'	1.9801(19)	1.989	1.959	1.966
Fe1-O2'	1.9650(18)	1.963	1.951	1.969
Fe1-O3'	1.9813(19)	1.974	1.950	1.942
Fe1-O1	1.9801(19)	2.001	1.949	1.946
Fe1-O3	1.9650(18)	1.965	1.946	1.958
Fe1-O2	1.9813(19)	1.981	1.975	1.956
Fe2-O1'	1.9718(9)	1.976	1.962	1.934
Fe2-O4	1.995(2)	2.013	1.981	1.957
Fe2-O4'	2.0321(19)	2.036	1.988	1.982
Fe2-O1	1.9718(9)	1.974	1.946	1.952
Fe2-O5'	1.995(2)	2.012	1.956	1.957
Fe2-O5	2.0321(19)	2.035	1.985	1.993
Fe3-O2'	1.9784(19)	2.005	1.947	1.958
Fe3-O6	1.9853(19)	1.995	1.972	1.989
Fe3-O6'	2.004(2)	2.006	1.979	1.972
Fe3-O7	1.993(2)	1.992	1.976	1.978
Fe3-O7'	1.9909(19)	2.007	1.977	1.972
Fe3-O2	1.9718(18)	1.988	1.943	1.971
Fe4-O3'	1.9718(18)	1.996	1.970	1.985
Fe4-O3	1.9784(19)	1.993	1.974	1.933
Fe4-O9'	1.9853(19)	1.990	1.974	1.966
Fe4-O9	2.004(2)	2.010	1.975	1.968
Fe4-O8'	1.993(2)	1.996	1.955	1.956
Fe4-O8	1.9909(19)	2.004	1.973	1.976
		Angles, °		
Fe2-Fe1-Fe3	118.74(1)	119.53	121.18	113.88
Fe2-Fe1-Fe4	118.74(1)	119.63	118.18	113.72
Fe3-Fe1-Fe4	122.51(2)	120.83	120.59	132.32
⟨Fe-O-Fe⟩	102.23(17)	101.99	101.48	100.85
Fe3-Fe1-Fe2-Fe4	180.00	178.85	177.85	177.13
γ	68.80	68.0	67.9	67.0

Table 5.8: Exchange coupling constants (reported in cm^{-1}) for the $Fe_4(dpm)_6$ on the CuN surface. The U parameters are in eV.

	U(Fe)	**U(O)**	**U(Cu)**	$\boldsymbol{J}_1$	$\boldsymbol{J}_2$	$\Delta E_{5,4}$
X-ray	4.1	3.0	-	16.8	0.5	38
Optimized	4.1	3.0	-	15.4	0.5	35
Extrapolated	4.1	3.0	-	13.6	0.5	30
Experiment				16.37(12)	0.29(11)	42
	4.1	3.0	-	5.5	3.3	1*
@CuN	4.1	3.0	5	8.8	-0.2	23
	4.1	3.0	5; 1**	8.5	5.2	2*

* The ground state is no more S=5, but S=1.
** It has been chosen to use a U value of 1 eV for the bottom two atomic layers, and 5 eV for the top two ones.

Table 5.9: The spin densities on the four Fe ions in the isolated and adsorbed on CuN $Fe_4(dpm)_6$ calculated with PBEsol+U method. The U parameters are in eV. Small differences are noticeable in the isolated clusters, unlike the adsorbed ones, where the values generally remain almost unchanged.

$Fe_4(dpm)_6$	**U(Fe)**	**U(O)**	**U(Cu)**	**Fe1**	**Fe2**	**Fe3**	**Fe4**
X-ray	4.1	3.0	-	-4.33	4.35	4.35	4.35
Optimized	4.1	3.0	-	-4.39	4.37	4.38	4.37
Extrapolated	4.1	3.0	-	-4.32	4.34	4.34	4.34
	4.1	3.0	-	-4.31	4.34	4.33	4.34
@CuN	4.1	3.0	5	-4.32	4.34	4.33	4.34
	4.1	3.0	5; 1*	-4.32	4.34	4.33	4.34

* It has been chosen to use a U value of 1 eV for the bottom two atomic layers, and 5 eV for the top two ones.

results to the case for U = 0, with a S =1 as a ground state. Possible explanation to the reason why the behaviour of the $Fe_4(dpm)_6$@CuN is so much different, is to be searched in the electronic structure of the hybrid system.

5.2.3 Electronic properties

The electronic structure of the isolated and extrapolated clusters is almost indistinguishable from one another, which confirms the small geometry changes, even if significant from the magnetic point of view, upon optimization on the CuN surface (see Figure 5.11). The PDOS shape is maintained also when the surface is considered. Similarly to the case of Au(111) the lack of significant shift towards low energies is an indication of weak physisorption process.

More interesting are the PDOS of the CuN surface within the hybrid system (see Figure 5.12). The application of the on-site correction is crucial to the position of the copper states. In that case, the peak at about -2 eV given by $3d$ Cu and $2p$ N states becomes visible and no more hidden as previously. In presence of Fe_4 states, such a peak mixes with characteristic O states of the cluster. Therefore, with U_{Cu}=0 eV,

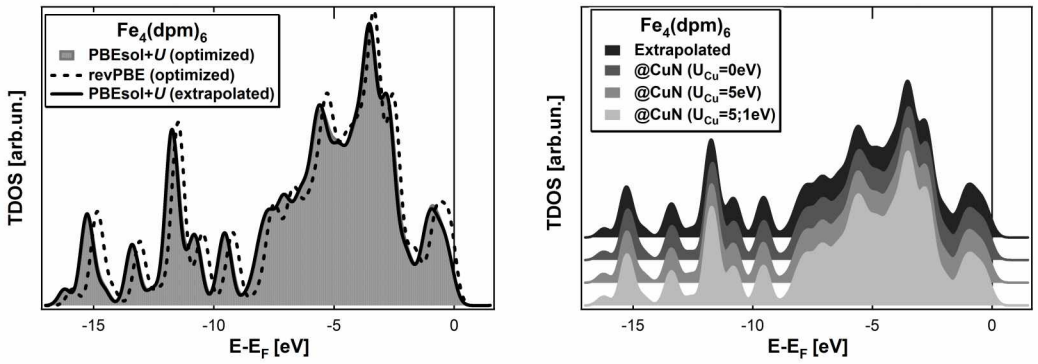

Figure 5.11: Comparison between the TDOS of $Fe_4(dpm)_6$ (left) and between the extrapolated structure and the one on CuN (right), all calculated at DFT+U level of theory. The σ is 0.35 eV.

these states can interact with the more bulk Cu ones inducing a strong Fe_4 core-surface interaction leading to a more antiferromagnetic behavior. In the case of U_{Cu}=5 eV, the mixing between cluster and CuN happens only for the topmost layers and therefore the interactions that occur, while still present, are smaller (see Figures 5.12 and 5.13). The DOS coming out from the case where two U values are used suggest that this is not a proper representation for the CuN surface since the bottom layers contribute to the strong band observed at -1 eV and not at -2 eV as observed in the experiment (see Figure 5.13). Such results confirm the soundness of the magnetic results obtained for U(Cu)=5 eV for all the layers.

In addition, an STM image has been simulated -2 eV (occupied states) in agreement with the bias used for the cluster on Au(111). The general shape and height are maintained similar to the one on gold, since the electronic density included in this energy window is similar in both hybrid systems due to the small rigid shifts to lower energies that take place.

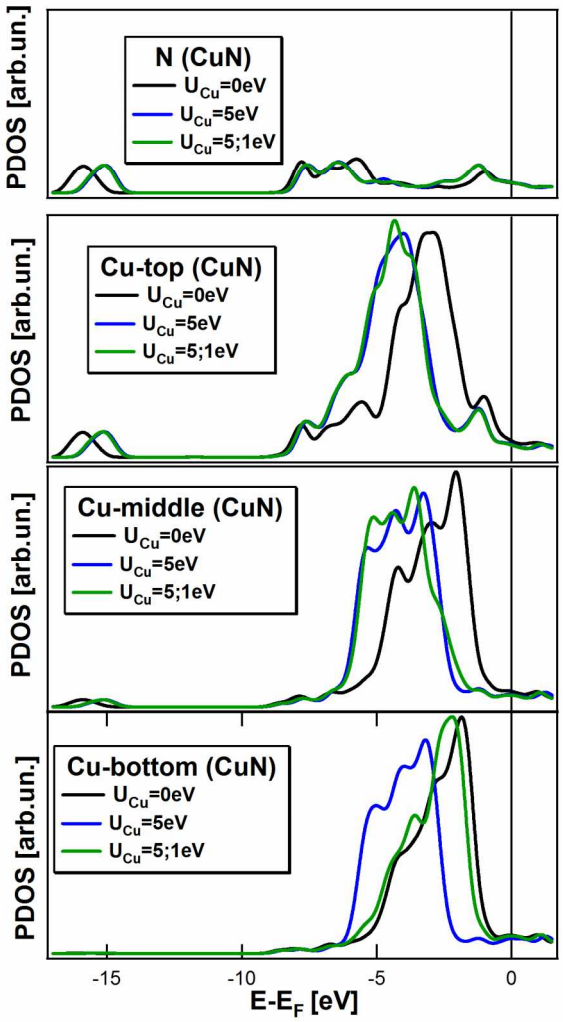

Figure 5.12: PDOS of the different atomic layers of the surface in the $Fe_4(dpm)_6$@CuN, where the Cu-bottom accounts for the two fixed atomic layers. The σ is 0.35eV.

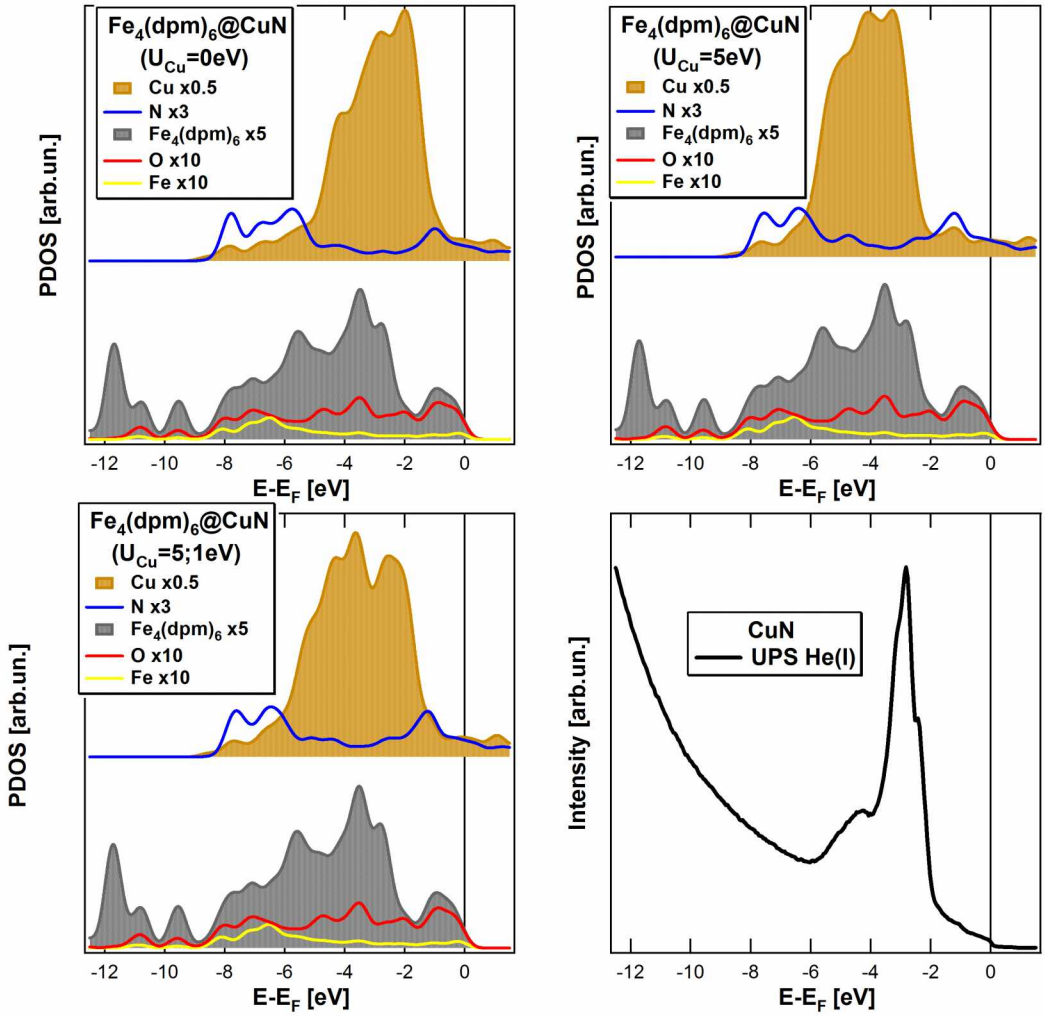

Figure 5.13: PDOS of the $Fe_4(dpm)_6$@CuN for U_{Cu} equal to 0 eV (top,left), 5 eV (top,right), and where the two top layers have U_{Cu}=5 eV and the bottom two have 1 eV (bottom, left), the σ is 0.35 eV. On the right bottom is presented the experimental UPS (He(I)) spectra of CuN. Some contributions have been enhanced in order to render them more easily visible.

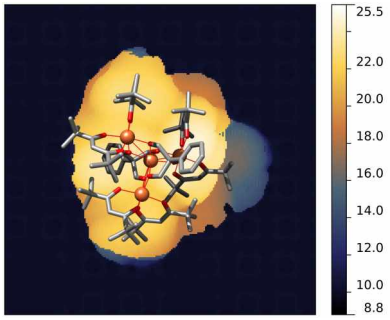

Figure 5.14: STM image simulated at 2 eV (occupied states) $Fe_4(dpm)_6$@CuN.

5.3 $Fe_4(dpm)_6$@LSMO

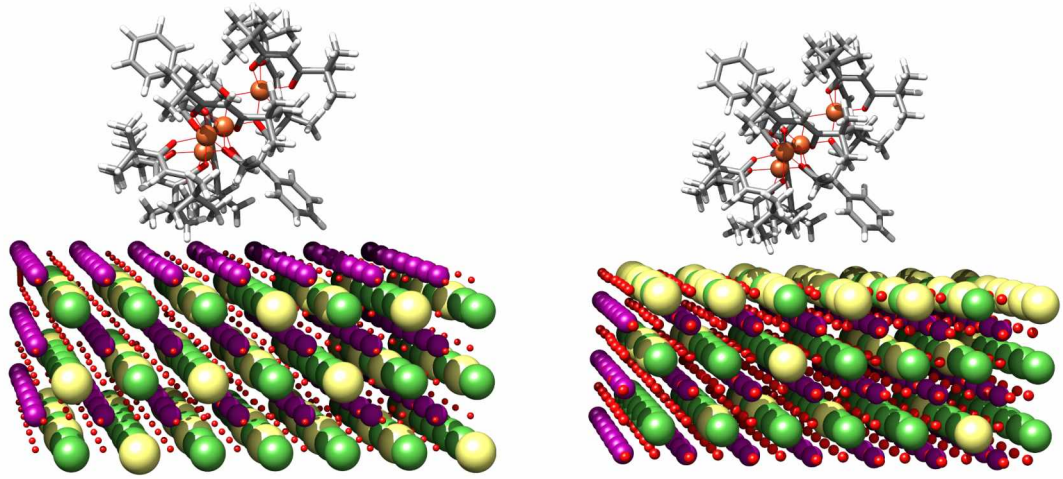

Figure 5.15: The optimized geometry of $Fe_4(dpm)_6$ on [MnO_2] (left) and [LaSrO-grad] (right).

In the previous sections, the properties and behaviour of $Fe_4(dpm)_6$ on non-magnetic surfaces has been described. It has been found that the type of substrate can strongly influence the magnetic properties of the cluster or leave them unaltered. In this section, special attention is given to the study of the $Fe_4(dpm)_6$ on the magnetic LSMO surface. Such hybrid system is a real challenge from computational point of view, since the magnetic properties of both the cluster and the substrate are to be considered. In addition, as already evidenced in Chapter 4 the termination layer is not univocally determined. The most energetically stable surface is the [LaSrO] one, where segregation of the Sr atoms to the surface is observed. For this reason, the 7×7×3 [LaSrO-grad] model is used, from now on called for simplicity [LaSrO]. In addition, the [MnO_2] termination layer is also considered, since it can be obtained when LSMO is grown on some substrates.[149]

The work on this hybrid system is in progress, therefore preliminary results only at hybrid functional level will be described below. They are expected to give an idea of the geometry changes that occur upon optimization and some indication of the interaction with the surfaces. The adsorbed cluster is a conformer of the $Fe_4(dpm)_6$ used in the previous studies. The small discrepancies in geometry and the practically identical DOS between the two structures imply similar results (see Figure 5.16), therefore it can still be considered a reliable approximation.

The computational protocol is the one used for both the isolated and the surface systems, already described in Chapters 3 and 4. The cluster leans on three *t*Bu-groups in both termination layers. The benzene rings points to the surface, however, unlike on Au(111) and CuN, it is slightly tilted to one side (see Figure 5.17). For both surfaces, a space of 12 Å both along x and y between the cluster and its periodic image is introduced.

5.3.1 Geometry

The surfaces barely change upon the deposition and optimization of $Fe_4(dpm)_6$, similarly to Au(111) and CuN. Indeed, the disposition of the oxygen atoms along z with respect to the Mn ones is maintained (see Table 5.11), differently from what observed with the N

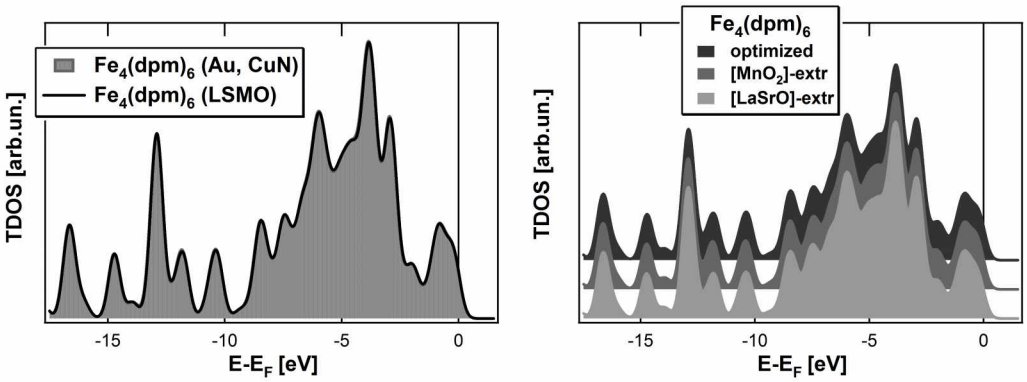

Figure 5.16: Comparison between the two $Fe_4(dpm)_6$ clusters used on Au,CuN and on LSMO (left); PDOS of the isolated and extrapolated clusters on [MnO_2] and [LaSrO] (right). The σ is 0.35eV.

for CuN. On the other hand, the interlayer separation between the planes of the oxygen atoms in (LaSrO) layers and the Mn ones slightly increases in the case of [MnO_2] slab, while for [LaSrO] they remain unchanged. This implied that the interlayer magnetic interaction in the former case is changed to small extent.

As far as the cluster is concerned, the geometry of the magnetic core in the extrapolated structures remains similar to the bulk phase with average differences estimated to be 0.7 and 1.1% for [MnO_2] and [LaSrO], respectively. Indeed, the shape and main characteristics of the DOS are maintained in both cases (see Figure 5.16). The Fe-Fe bonds tend to be longer upon adsorption in agreement with the other two hybrid systems. In addition, the ⟨Fe-O-Fe⟩ has higher values, therefore stronger magnetic interactions are expected for the adsorbed clusters.[56]

The $Fe_4(dpm)_6$ is positioned closer (≈1.74 Å) to the [MnO_2] surface, compared to ≈2.05 Å for [LaSrO]. The approximate adsorption energy in the former case is higher, E_{ads}=-52 kcal/mol and E_{ads}=-61 kcal/mol in the latter. Such behaviour can be explained considering that the negatively charged (MnO_2) is expected to be more chemically active due to the unsaturated coordination sphere of the Mn ions and the presence of a larger number of oxygen atoms ready to interact with the cluster protons.

One of the main differences between this hybrid system and the previously studies is the way the cluster is adsorbed on the surface. On Au(111) and CuN, the $Fe_4(dpm)_6$ uses two dpm ligands to lean on the surfaces and on the LSMO, they are three. In this way, the closer to the substrate is not only one, but two Fe ions (See Figure 5.17). Such a different adsorption structure results in the easy axis of magnetization angles with respect to the normal vector of the surface of about 45 °, approximately 10 ° higher than the other two hybrid systems.

5.3.2 Magnetic properties

Working with magnetic cluster on magnetic surface requires the study of three different magnetic properties. The first two consider the changes in the cluster and in the surface that occur upon adsorption. The third one estimates the magnetic interaction between the two systems.

The magnetic exchange coupling constants of the isolated $Fe_4(dpm)_6$ are in good agreement with the X-ray results, which confirms the reliability of the structure of the

Table 5.10: Bond lengths and angles of the isolated $Fe_4(dpm)_6$ and the one deposited on [LaSrO] and [MnO_2] surfaces.

$Fe_4(dpm)_6$	**X-ray**	**$Fe_4(dpm)_6$**	**@[MnO_2]**	**@[LaSrO]**
		Bonds (Å)		
Fe1-Fe2	3.0780(8)	3.129	3.177	3.182
Fe1-Fe3	3.0726(6)	3.162	3.159	3.183
Fe1-Fe4	3.0726(6)	3.110	3.140	3.159
Fe2-Fe3	5.2925(7)	5.466	5.482	5.530
Fe3-Fe4	5.3880(1)	5.430	5.492	5.480
Fe2-Fe4	5.2925(7)	5.385	5.437	5.483
Fe1-O1'	1.9801(19)	2.023	2.013	2.016
Fe1-O2'	1.9650(18)	2.001	2.015	2.024
Fe1-O3'	1.9813(19)	2.015	2.034	2.027
Fe1-O1	1.9801(19)	2.010	2.008	2.004
Fe1-O3	1.9650(18)	2.003	2.002	2.027
Fe1-O2	1.9813(19)	2.007	2.020	2.023
Fe2-O1'	1.9718(9)	2.001	2.002	2.009
Fe2-O4	1.995(2)	2.017	2.046	2.059
Fe2-O4'	2.0321(19)	2.085	2.098	2.098
Fe2-O1	1.9718(9)	2.043	2.032	2.034
Fe2-O5'	1.995(2)	2.062	2.089	2.087
Fe2-O5	2.0321(19)	2.059	2.041	2.065
Fe3-O2'	1.9784(19)	2.024	2.022	2.022
Fe3-O6	1.9853(19)	2.036	2.021	2.063
Fe3-O6'	2.004(2)	2.052	2.061	2.055
Fe3-O7	1.993(2)	2.067	2.069	2.050
Fe3-O7'	1.9909(19)	2.073	2.060	2.078
Fe3-O2	1.9718(18)	2.048	2.054	2.146
Fe4-O3'	1.9718(18)	2.005	2.012	1.997
Fe4-O3	1.9784(19)	2.021	2.028	2.053
Fe4-O9'	1.9853(19)	2.064	2.060	2.048
Fe4-O9	2.004(2)	2.035	2.020	2.095
Fe4-O8'	1.993(2)	2.100	2.041	2.073
Fe4-O8	1.9909(19)	2.048	2.066	2.110
		Angles (°)		
Fe2-Fe1-Fe3	118.74(1)	120.66	119.83	120.63
Fe2-Fe1-Fe4	118.74(1)	119.32	118.79	119.69
Fe3-Fe1-Fe4	122.51(2)	119.94	121.33	119.55
⟨Fe-O-Fe⟩	102.23(17)	102.18	102.97	103.10
Fe3-Fe1-Fe2-Fe4	180.00	176.7	177.6	175.9
γ	68.80	69.9	71.6	71.2

conformer. The extrapolated structures exhibit stronger antiferromagnetic behaviour, in line with the geometry results discussed above. It is interesting to notice that the resultant clusters after the optimization on both termination layers are identical from

Table 5.11: Rumpling parameters r for both surfaces before and after the adsorption of $Fe_4(dpm)_6$, calculated as $r = z(O) - z(Mn)$.

	$[MnO_2]$	Fe_4@$[MnO_2]$	[LaSrO-grad]	Fe_4@[LaSrO-grad]
r_{top} (Å)	−0.17	−0.18	−0.05	−0.05
r_{middle} (Å)	−0.14	−0.14	0.06	0.06
r_{bottom} (Å)	−0.08	−0.08	0.00	0.00

Table 5.12: Average interlayer separation in Å, calculated as the average between the planes of the Mn atoms and that of the axial oxygen atoms in the successive [LaSrO]-planes.

	$[MnO_2]$	Fe_4@$[MnO_2]$		[LaSrO-grad]	Fe_4@[LaSrO-grad]
Δ_{Mn3-O3}	2.174	2.186	Δ_{O3-Mn3}	1.974	1.967
Δ_{O3-Mn2}	1.838	1.841	Δ_{Mn3-O2}	1.998	1.995
Δ_{Mn2-O2}	2.064	2.090	Δ_{O2-Mn2}	2.028	2.029
Δ_{O2-Mn1}	1.908	1.911	Δ_{Mn2-O1}	1.915	1.915
Δ_{Mn1-O1}	1.907	1.923	Δ_{O1-Mn1}	2.029	2.030

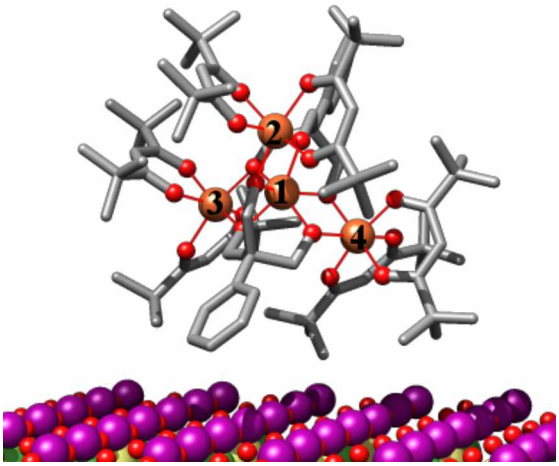

Figure 5.17: A side view of the $Fe_4(dpm)_6$ deposited on $[MnO_2]$. Similar is the disposition on [LaSrO] surface.

magnetic point of view (see Table 5.13).

Since the evaluation of the magnetic properties has been done only at hybrid (PBE0) level, it has not been possible to establish the electronic effects the surfaces have on the magnetic state of the cluster. However, a simple comparison between the values obtained at revPBE level show that much stronger interactions are expected on LSMO than on Au(111). In addition, the strength of interaction between the two termination layers varies - on [LaSrO] the J values evidence for less antiferromagnetic coupling.

As far as the magnetic properties of the LSMO surfaces are concerned, the geometry changes and the spin densities on the Mn ions with respect to the layer (see Table 5.14) remain similar to the bare surfaces. Therefore, no significant variations in the interlayer interactions is expected.

Table 5.13: Exchange coupling constants (reported in cm_1) for the $Fe_4(dpm)_6$ on the LSMO surfaces, calculated with PBE0 for the cluster structures and revPBE when the surface is included.

	J_1	J_2	$\Delta E_{5,4}$
X-ray	14.4	0.3	34
Optimized	11.8	0.1	29
Extrapolated [MnO_2]	13.8	0.2	33
Extrapolated [LaSrO]	13.9	0.2	33
Experiment	16.37(12)	0.29(11)	42
@[MnO_2]	56.3	3.3	116
@[LaSrO]	43.9	1.2	96
@Au(111)	15.7	2.1	24

Table 5.14: Distribution of the Mn spin densities in the two surfaces with and without $Fe_4(dpm)_6$.

[MnO_2]	**Fe_4@[MnO_2]**	**Layer**	**[LaSrO-grad]**	**Fe_4@[LaSrO-grad]**
3.88	3.89	Top	3.48	3.47
3.32	3.32	Middle	3.49	3.48
3.44	3.45	Bottom	3.77	3.77
3.54	3.56	Average	3.58	3.57

The magnetic interaction between the cluster and the surface has been evaluated as the difference between two states - ferromagnetic one (FM) and antiferromagnetic one (AFM). In the first case, the spins on the Fe are parallel to those on the Mn ions, while in the second case, they have opposite signs. Both termination layers prefer the AFM alignment, even though the interaction is stronger in the case of [MnO_2] (see Table 5.15). Such results can be crucial for the future use of $Fe_4(dpm)_6$ as spin filter on the LSMO surface.

5.3.3 Electronic properties

Unlike in the case of the hybrid Au(111) and CuN systems, the cluster experiences strong physisoprtion on the LSMO surfaces. In Figure 5.18 it can be seen that in the case of [MnO_2] termination layer, there is a rigid shift of 0.5 eV towards lower energies of the DOS. The interaction between the cluster and [LaSrO] appears to be even stronger, since the shift in this case is of 1.3 eV towards lower energies. Moreover, the shape of the central broad region changes and this is not due to any significant geometry distortions as it can be seen in Figure 5.16, but mainly to the enhanced electronic contributions of

Table 5.15: The preference of spin orientation in the cluster with respect to the surface is estimated *via* the energy difference ΔE(FM-AFM).

$Fe_4(dpm)_6$	ΔE(FM-AFM) (cm^{-1})
@[MnO_2]	6.60
@[LaSrO]	1.25

the segregated [LaSrO].

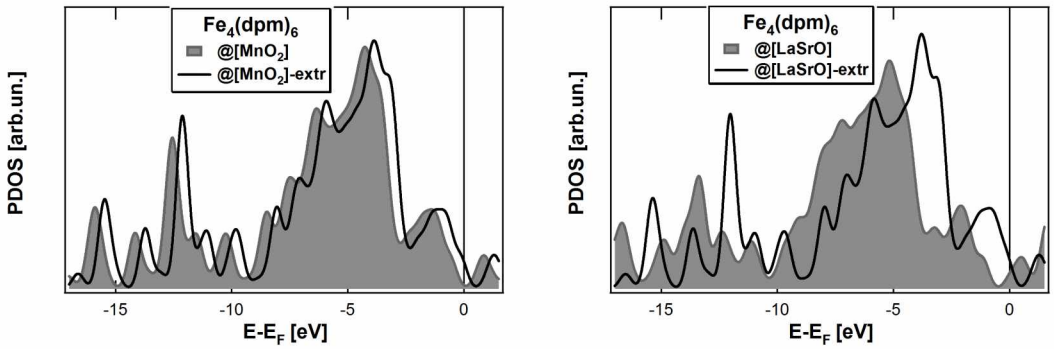

Figure 5.18: Comparison at revPBE level of theory between the DOS of the extrapolated $Fe_4(dpm)_6$ and on [MnO_2] (left) and [LaSrO-grad] (right). The σ is 0.35 eV.

It appears that no such changes take place on the surfaces, since their DOS remain unchanged with respect to their correspondent bare ones. Even so, the presence of the $Fe_4(dpm)_6$ induces a reduction of the minority spin gap from 1.20 to 0.80 eV for [LaSrO] and from 0.82 to 0.58 eV. In line with this, the spin polarization at Fermi level is strongly reduced in the latter case, since it decreases from 99 to 73%. Such a decrease is to be mainly attributed to the shift of cluster bands near the Fermi region. However, before drawing any conclusions, it is important to check whether this is due to the theoretical setbacks of using pure functional which tend to underestimate the gap or this has a physical meaning.

As far as the STM images are regarded, the whole image shape of the cluster is maintained, even though it is slightly different from the ones observed for Au(111) and CuN due to the different way it is positioned on the surface. The change in termination layer does not imply severe discrepancies.

In conclusion, it has been proven that even though no significant geometry changes are induced on both cluster and surface upon adsorption, strong magnetic interaction takes place between them, which depends on the termination layer. Further studies would be mandatory to elucidate the behaviour of the cluster and the LSMO.

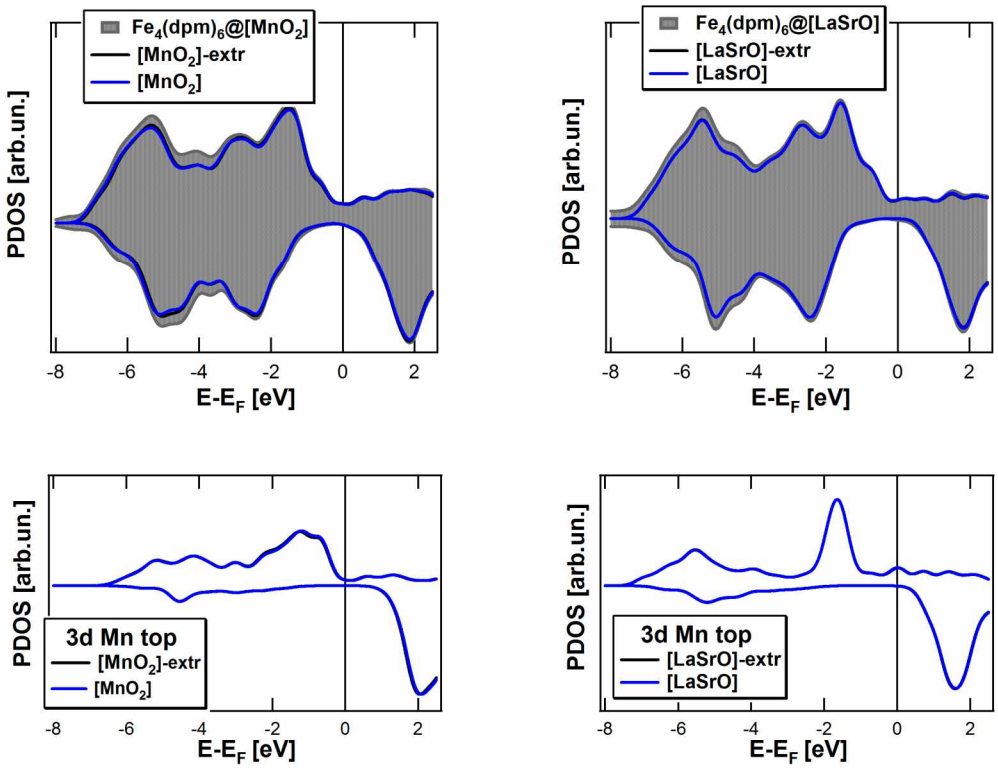

Figure 5.19: Comparison between the DOS of the surfaces with respect to their bare correspondents and the TDOS of the hybrid systems, $[MnO_2]$ (top, left) and [LaSrO-grad] (top, right); comparison between the $3d$ states of the Mn top ions fore bare and adsorbed surface. The σ is 0.3 eV.

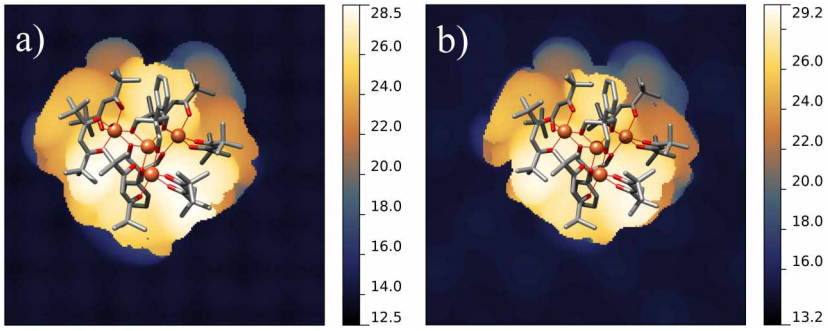

Figure 5.20: Simulated STM images of the $Fe_4(dpm)_6$ on a) $[MnO_2]$ and b) [LaSrO-grad].

CHAPTER

SIX

CONCLUSIONS

The present thesis studies single-molecule magnets, surfaces and their properties before and after adsorption at DFT level. The main goals focus on the elucidation and evaluation of the interactions in such hybrid systems and the set-up of a reliable and flexible computational protocol, in the framework of the Gaussian and plane wave (GPW) method, able to reproduce the structural, magnetic and electronic properties of the SMMs and surfaces as isolated and hybrid systems.

The constituting parts of the hybrid systems have been studied separately, and only then together in order to evaluate any possible changes that occur upon adsorption.

First, the study has been concentrated on two SMMs of the family Fe_4, investigated in their bulk phase. The computed results of their magnetic and electronic properties with hybrid functional are in good agreement with the experimental ones. However, one of the main setbacks of such approach, despite the good results for isolated and small systems, is the fact that it is computationally too expensive for adsorbed systems. Therefore, the parametrized DFT+U approach has been exploited for its cheapness and transferability. A couple of parameters, U(Fe)=4.1 eV and U(O)=3.0 eV, have been fitted on the experimental UPS spectra and magnetic exchange coupling constants. Due to the same magnetic core within the Fe_4 family, these U value are expected to give reliable results also for the properties of the other members. The set up of such an approach has paved the possibility to study the electronic effects that the substrate has on the SMM upon deposition and vice versa.

Before doing it, the next step has been to model and reproduce the main characteristic properties of the bare surfaces. Three different substrates have been chosen, based on their use in spintronic devices, namely Au(111), CuN, LSMO. The structural properties of all surfaces have been reproduced as well as the characteristic half-metallicity of the LSMO. Two termination layers have been considered in the case of LSMO. In addition, the experimentally observed Sr segregation towards the surface is confirmed by testing various models. Such results prove the reliability of the computational protocol to study surface systems.

The last step consists of deposition of the Fe_4 cluster on the three surfaces and study the changes that occur upon adsorption. The Fe_4@Au(111) weakly interacts with the surface, which results in small alternations in the geometry of both cluster and surface. The cluster maintains its ground spin state (S=5) within the hybrid system, which is supported by experimental XMCD studies. In addition, good agreement is observed between the experimental and simulated STM images. Such results prove

suitability of the computational protocol and give the confidence to try it on the other substrates. The behaviour of the cluster on the CuN is found to be different. The SMM interacts in a stronger way the surface, which has consequences on its magnetic properties. The most challenging case is the LSMO one, where the magnetic properties of both cluster and surface are to be accounted for. The Fe_4 has been deposited on the two possible termination layers of the LSMO surface. The preliminary results show that stronger physisorption takes place for both termination layers, where more stable is the antiferromagnetic alignment of the spins of the surface and cluster. Such results are promising for eventual use of such hybrid systems in spintronic devices. However, further studies would be necessary to completely describe the system.

In conclusion the computational protocol developed in this thesis has shown to be a reliable tool for the study of complex systems as SMMs on surfaces. For such a reason it can be considered as a useful hint for future experiments and calculations to better understand the interactions between surfaces and magnetic molecules.

BIBLIOGRAPHY

[1] S. A. Wolf, D. D. Awschalom, R. A. Buhrman, J. M. Daughton, S. von Molnár, M. L. Roukes, A. Y. Chtchelkanova and D. M. Treger, *Science*, 2001, **294**, 1488–1495.

[2] S. Sanvito, *Nature Physics*, 2010, **6**, 562–564.

[3] S. Sanvito, *Chemical Society Reviews*, 2011, **40**, 3336–3355.

[4] A. R. Rocha, V. M. Garcia-Suarez, S. W. Bailey, C. J. Lambert, J. Ferrer and S. Sanvito, *Nature Materials*, 2005, **4**, 335–339.

[5] L. Bogani and W. Wernsdorfer, *Nature Materials*, 2008, **7**, 179–186.

[6] R. Sessoli, D. Gatteschi, A. Caneschi and M. A. Novak, *Nature*, 1993, **365**, 141–143.

[7] N. J. Tao, *Nature Nanotechnology*, 2006, **1**, 173–181.

[8] S. Sanvito and A. R. Rocha, *Journal of Computational and Theoretical Nanoscience*, 2008, **3**, 624–642.

[9] E. Burzurí, Y. Yamamoto, M. Warnock, X. Zhong, K. Park, A. Cornia and H. S. J. van der Zant, *Nano Letters*, 2014, **14**, 3191–3196.

[10] V. Krinichnyi, *Synthetic Metals*, 2000, **108**, 173–222.

[11] I. Bergenti, V. Dediu, M. Prezioso and A. Riminucci, *Philosophical Transactions of the Royal Society A*, 2011, **369**, 3054–3068.

[12] Z. H. Xiong, D. Wu, Z. V. Vardeny and J. Shi, *Nature*, 2004, **427**, 821–824.

[13] L. Zhu, K. L. Yao and Z. L. Liu, *Applied Physics Letters*, 2010, **96**, 082115.

[14] S. Stepanow, J. Honolka, P. Gambardella, L. Vitali, N. Abdurakhmanova, T. C. Tseng, S. Rauschenbach, S. L. Tait, V. Sessi, S. Klyatskaya, M. Ruben and K. Kern, *Journal of the American Chemical Society*, 2010, **132**, 11900–11901.

[15] L. Margheriti, D. Chiappe, M. Mannini, P. Car, P. Sainctavit, M.-A. Arrio, F. B. de Mongeot, J. C. Cezar, F. M. Piras, A. Magnani, E. Otero, A. Caneschi and R. Sessoli, *Advanced Materials*, 2010, **22**, 5488–5493.

[16] A. Lodi Rizzini, C. Krull, T. Balashov, J. J. Kavich, A. Mugarza, P. S. Miedema, P. K. Thakur, V. Sessi, S. Klyatskaya, M. Ruben, S. Stepanow and P. Gambardella, *Physical Review Letters*, 2011, **107**, 177205.

[17] A. Lodi Rizzini, C. Krull, T. Balashov, A. Mugarza, C. Nistor, F. Yakhou, V. Sessi, S. Klyatskaya, M. Ruben, S. Stepanow and P. Gambardella, *Nano Letters*, 2012, **12**, 5703–5707.

[18] L. Malavolti, L. Poggini, L. Margheriti, D. Chiappe, P. Graziosi, B. Cortigiani, V. Lanzilotto, F. Buatier de Mongeot, P. Ohresser, E. Otero, F. Choueikani, P. Sainctavit, I. Bergenti, V. a. Dediu, M. Mannini and R. Sessoli, *Chemical Communications*, 2013, **49**, 11506–8.

[19] A. Cornia, M. Mannini, P. Sainctavit and R. Sessoli, *Chemical Society Reviews*, 2011, **40**, 3076–91.

[20] M. Mannini, F. Pineider, C. Danieli, F. Totti, L. Sorace, P. Sainctavit, M. A. Arrio, E. Otero, L. Joly, J. C. Cezar, A. Cornia and R. Sessoli, *Nature*, 2010, **468**, 417–421.

[21] S. Fahrendorf, N. Atodiresei, C. Besson, V. Caciuc, F. Matthes, S. Blügel, P. Kögerler, D. E. Bürgler and C. M. Schneider, *Nature Communications*, 2013, **4**, 2425.

[22] R. W. Saalfrank, A. Scheurer, I. Bernt, F. W. Heinemann, A. V. Postnikov, V. Schunemann, A. X. Trautwein, M. S. Alam, H. Rupp and P. Muller, *Dalton Transactions*, 2006, 2865–2874.

[23] S. Kahle, Z. Deng, N. Malinowski, C. Tonnoir, A. Forment-Aliaga, N. Thontasen, G. Rinke, D. Le, V. Turkowski, T. S. Rahman, S. Rauschenbach, M. Ternes and K. Kern, *Nano Letters*, 2012, **12**, 518–521.

[24] F. Totti, G. Rajaraman, M. Iannuzzi and R. Sessoli, *Journal of Physical Chemistry C*, 2013, **117**, 7186–7190.

[25] F. Moro, V. Corradini, M. Evangelisti, V. De Renzi, R. Biagi, U. del Pennino, C. J. Milios, L. F. Jones and E. K. Brechin, *Journal of Physical Chemistry B*, 2008, **112**, 9729–9735.

[26] M. Mannini, L. Margheriti, D. Chiappe, P. E. Car, P. Sainctavit, M. A. Arrio, F. B. de Mongeot, J. C. Cezar, F. M. Piras, A. Magnani, E. Otero, A. Caneschi and R. Sessoli, *Advanced Materials*, 2010, **22**, 5488–5493.

[27] G. Lippert, J. Hutter and M. Parrinello, *Molecular Physics*, 1997, **92**, 477–487.

[28] S. Goedecker, M. Teter and J. Hutter, *Physical Review B*, 1996, **54**, 1703–1710.

[29] G. Santarossa, A. Vargas, M. Iannuzzi, C. A. Pignedoli, D. Passerone and A. Baiker, *The Journal of Chemical Physics*, 2008, **129**, 234703.

[30] J. Perdew, K. Burke and M. Ernzerhof, *Physical Review Letters*, 1996, **77**, 3865–3868.

[31] Y. Zhang and W. Yang, *Physical Review Letters*, 1998, **80**, 890.

[32] J. Perdew, A. Ruzsinszky, G. Csonka, O. Vydrov, G. Scuseria, L. Constantin, X. Zhou and K. Burke, *Physical Review Letters*, 2008, **100**, 136406.

[33] E. Fabiano, L. A. Constantin and F. Della Sala, *Physical Review B*, 2010, **82**, 113104.

[34] E. Fabiano, L. A. Constantin and F. Della Sala, *The Journal of Chemical Physics*, 2011, **134**, 194112.

[35] S. Grimme, *Wiley Interdisciplinary Reviews: Computational Molecular Science*, 2011, **1**, 211–228.

[36] S. Grimme, J. Antony, S. Ehrlich and H. Krieg, *The Journal of Chemical Physics*, 2010, **132**, 154104.

[37] C. Adamo and V. Barone, *The Journal of Chemical Physics*, 1999, **110**, 6158.

[38] V. I. Anisimov, J. Zaanen and O. K. Andersen, *Physical Review B*, 1991, **44**, 943–954.

[39] M. Cococcioni and S. de Gironcoli, *Physical Review B*, 2005, **71**, 035105.

[40] S. L. Dudarev, G. A. Botton, S. Y. Savrasov, C. J. Humphreys and A. P. Sutton, *Physical Review B*, 1998, **57**, 1505–1509.

[41] B. Himmetoglu, A. Floris, S. de Gironcoli and M. Cococcioni, *International Journal of Quantum Chemistry*, 2014, **114**, 14–49.

[42] J. Bardeen, *Physical Review Letters*, 1961, **6**, 6–8.

[43] J. Tersoff and D. R. Hamann, *Physical Review B*, 1985, **31**, 805–813.

[44] V. Brazdova and D. R. Bowler, *Atomistic Computer Simulations: A Practical Guide*, John Wiley & Sons, 2013, p. 367.

[45] C. R. Jacob and M. Reiher, *International Journal of Quantum Chemistry*, 2012, **112**, 3661–3684.

[46] D. Gatteschi, R. Sessoli and J. Villain, *Molecular nanomagnets*, Oxford University Press, Oxford, UK, 2006.

[47] J. P. Malrieu, R. Caballol, C. J. Calzado, C. de Graaf and N. Guihéry, *Chemical reviews*, 2014, **114**, 429–92.

[48] L. Noodleman and J. G. J. Norman, *The Journal of Chemical Physics*, 1979, **70**, 4903.

[49] L. Noodleman, *Journal of Chemical Physics*, 1981, **74**, 5737.

[50] P. A. M. Dirac, *Proceedings of the Royal Society A*, 1926, **112**, 661–677.

[51] W. Z. Heisenberg, *Zeitschrift für Physik*, 1928, **49**, 619–636.

[52] J. H. Van Vleck, *The Theory of Electric and Magnetic Susceptibility*, Oxford University Press, Oxford, 1932.

[53] A. Bencini and F. Totti, *International Journal of Quantum Chemistry*, 2005, **101**, 819–825.

[54] A. Bencini and F. Totti, *Journal of Chemical Theory and Computation*, 2009, **5**, 144–154.

[55] A. Lunghi and F. Totti, *Journal of Materials Chemistry C*, 2014, **2**, 8333–8343.

[56] S. Accorsi, A.-L. Barra, A. Caneschi, G. Chastanet, A. Cornia, A. C. Fabretti, D. Gatteschi, C. Mortalo, E. Olivieri, F. Parenti, P. Rosa, R. Sessoli, L. Sorace, W. Wernsdorfer and L. Zobbi, *Journal of the American Chemical Society*, 2006, **128**, 4742–4755.

[57] L. Rigamonti, M. Piccioli, L. Malavolti, L. Poggini, M. Mannini, F. Totti, B. Cortigiani, A. Magnani, R. Sessoli and A. Cornia, *Inorganic Chemistry*, 2013, **4**, 5897–5905.

[58] L. Margheriti, M. Mannini, L. Sorace, L. Gorini, D. Gatteschi, A. Caneschi, D. Chiappe, R. Moroni, F. Buatier de Mongeot, A. Comia, F. M. Piras, A. Magnani and R. Sessoli, *Small*, 2009, **5**, 1460–1466.

[59] N. Dori, M. Menon, L. Kilian, M. Sokolowski, L. Kronik and E. Umbach, *Physical Review B*, 2006, **73**, 195208.

[60] G. Fratesi, V. Lanzilotto, S. Stranges, M. Alagia, G. P. Brivio and L. Floreano, *Physical Chemistry Chemical Physics*, 2014, **16**, 14834–14844.

[61] R. W. Saalfrank, A. Scheurer, I. Bernt, F. W. Heinemann, A. V. Postnikov, V. Schünemann, A. X. Trautwein, M. S. Alam, H. Rupp and P. Müller, *Dalton Transactions*, 2006, 2865–2874.

[62] J. Kortus, M. R. Pederson, T. Baruah, N. Bernstein and C. S. Hellberg, *Polyhedron*, 2003, **22**, 1871–1876.

[63] R. Singh, A. Banerjee, E. Colacio and K. K. Rajak, *Inorganic chemistry*, 2009, **48**, 4753–4762.

[64] J. Ribas-Arino, T. Baruah and M. R. Pederson, *The Journal of Chemical Physics*, 2005, **123**, 044303.

[65] U. del Pennino, V. Corradini, R. Biagi, V. De Renzi, F. Moro, D. Boukhvalov, G. Panaccione, M. Hochstrasser, C. Carbone, C. J. Milios and E. K. Brechin, *Physical Review B*, 2008, **77**, 085419.

[66] U. del Pennino, V. De Renzi, R. Biagi, V. Corradini, L. Zobbi, A. Cornia, D. Gatteschi, F. Bondino, E. Magnano, M. Zangrando, M. Zacchigna, A. Lichtenstein and D. W. Boukhvalov, *Surface Science*, 2006, **600**, 4185–4189.

[67] D. W. Boukhvalov, E. Z. Kurmaev, A. Moewes, M. V. Yablonskikh, S. Chiuzbàian, V. R. Galakhov, L. D. Finkelstein, M. Neumann, M. I. Katsnelson, V. V. Dobrovitski and A. L. Lichtenstein, *Journal of Electron Spectroscopy and Related Phenomena*, 2004, **137-140**, 735–739.

[68] D. Boukhvalov, A. Lichtenstein, V. Dobrovitski, M. Katsnelson, B. Harmon, V. Mazurenko and V. Anisimov, *Physical Review B*, 2002, **65**, 184435.

[69] C. J. Mundy, F. Mohamed, F. Schiffman, G. Tabacchi, H. Forbert, W. Kuo, J. Hutter, M. Krack, M. Iannuzzi, M. McGrath, M. Guidon, T. D. Kuehne, J. VandeVondele, V. Weber and T. Laino, *Cp2k Program Package*.

[70] C. Hartwigsen, S. Goedecker and J. Hutter, *Physical Review B*, 1998, **58**, 3641–3662.

[71] J. VandeVondele and J. Hutter, *The Journal of Chemical Physics*, 2007, **127**, 114105.

[72] J. Yeh and I. Lindau, *Atomic Data and Nuclear Data Tables*, 1985, **32**, 1–155.

[73] J. F. Nossa, M. F. Islam, C. M. Canali and M. R. Pederson, *Physical Review B*, 2013, **88**, 224423.

[74] K. Momma and F. Izumi, *Journal of Applied Crystallography*, 2011, **44**, 1272–1276.

[75] P. M. Panchmatia, B. Sanyal and P. M. Oppeneer, *Chemical Physics*, 2008, **343**, 47–60.

[76] J. Paier, M. Marsman, K. Hummer, G. Kresse, I. C. Gerber and J. G. Angyán, *The Journal of Chemical Physics*, 2006, **124**, 154709.

[77] C. Cao, S. Hill and H.-P. Cheng, *Physical Review Letters*, 2008, **100**, 167206.

[78] S. Gangopadhyay, A. E. Masunov, E. Poalelungi and M. N. Leuenberger, *The Journal of chemical physics*, 2010, **132**, 244104.

[79] G. J. Martyna and M. E. Tuckerman, *The Journal of Chemical Physics*, 1999, **110**, 2810.

[80] L. Genovese, T. Deutsch, A. Neelov, S. Goedecker and G. Beylkin, *The Journal of Chemical Physics*, 2006, **125**, 074105.

[81] L. Genovese, T. Deutsch and S. Goedecker, *The Journal of Chemical Physics*, 2007, **127**, 054704.

[82] L. Bengtsson, *Physical Review B*, 1999, **59**, 12301–12304.

[83] W. Tyson and W. Miller, *Surface Science*, 1977, **62**, 267–276.

[84] J. C. Boettger, *Physical Review B*, 1994, **49**, 798–800.

[85] R. J. Needs, *Physical Review Letters*, 1987, **58**, 53–56.

[86] V. Fiorentini and M. Methfessel, *Journal of Physics: Condensed Matter*, 1996, **8**, 6525.

[87] S. Tatay, C. Barraud, M. Galbiati, P. Seneor, R. Mattana, K. Bouzehouane, C. Deranlot, E. Jacquet, A. Forment-Aliaga, P. Jegou, A. Fert and F. Petroff, *ACS Nano*, 2012, **6**, 8753–8757.

[88] A. Saywell, G. Magnano, C. J. Satterley, L. M. A. Perdigão, A. J. Britton, N. Taleb, M. del Carmen Giménez-López, N. R. Champness, J. N. O'Shea and P. H. Beton, *Nature Communications*, 2010, **1**, 75.

[89] L. El-Kareh, P. Mehring, V. Caciuc, N. Atodiresei, A. Beimborn, S. Blügel and C. Westphal, *Surface Science*, 2014, **619**, 67–70.

[90] A. Bencini, G. Rajaraman, F. Totti and M. Tusa, *Superlattices and Microstructures*, 2009, **46**, 4–9.

[91] G. Rajaraman, A. Caneschi, D. Gatteschi and F. Totti, *Physical Chemistry Chemical Physics*, 2011, **13**, 3886–3895.

[92] W. Chen, V. Madhavan, T. Jamneala and M. F. Crommie, *Physical Review Letters*, 1998, **80**, 1469–1472.

[93] G. V. Hansson and S. A. Flodstroem, *Physical Review B*, 1978, **18**, 1572–1585.

[94] V. De Renzi, R. Rousseau, D. Marchetto, R. Biagi, S. Scandolo and U. del Pennino, *Physical Review Letters*, 2005, **95**, 046804.

[95] J. Repp, G. Meyer, S. Stojkovic, A. Gourdon and C. Joachim, *Physical Review Letters*, 2005, **94**, 026803.

[96] J. M. Burkstrand, G. G. Kleiman, G. G. Tibbetts and J. C. Tracy, *Journal of Vacuum Science and Technology*, 1976, **13**, 291.

[97] G. G. Tibbetts, J. M. Burkstrand and J. C. Tracy, *Physical Review B*, 1977, **15**, 3652–3660.

[98] F. Leibsle, C. Flipse and A. Robinson, *Physical Review B*, 1993, **47**, 15865–15868.

[99] F. M. Leibsle, S. S. Dhesi, S. D. Barrett and A. W. Robinson, *Surface Science*, 1994, **317**, 309–320.

[100] T. Choi, C. Ruggiero and J. Gupta, *Physical Review B*, 2008, **78**, 035430.

[101] S. M. Driver and D. P. Woodru, *Surface Science*, 2001, **492**, 11–26.

[102] C. F. Hirjibehedin, C. P. Lutz and A. J. Heinrich, *Science*, 2006, **312**, 1021–1024.

[103] Y. Yoshimoto and S. Tsuneyuki, *Surface Science*, 2002, **514**, 200–205.

[104] Y. Yoshimoto and S. Tsuneyuki, *Applied Surface Science*, 2004, **237**, 274–278.

[105] J. T. Hoeft, M. Polcik, M. Kittel, R. Terborg, R. L. Toomes and J. Kang, *Surface Science*, 2001, **492**, 1–10.

[106] S. Hong, T. S. Rahman, E. Z. Ciftlikli and B. J. Hinch, *Physical Review B*, 2011, **84**, 165413.

[107] X.-M. Tao, M.-Q. Tan, X.-X. Zhao, W.-B. Chen, X. Chen and X.-F. Shang, *Surface Science*, 2006, **600**, 3419–3426.

[108] H. C. Zeng and K. A. R. Mitchell, *Langmuir*, 1989, **5**, 829–833.

[109] J. Gómez Díaz, Y. Ding, R. Koitz, A. P. Seitsonen, M. Iannuzzi and J. Hutter, *Theoretical Chemistry Accounts*, 2013, **132**, 1350.

[110] M. E. Straumanis and L. S. Yu, *Acta Crystallographica Section A*, 1969, **25**, 676–682.

[111] T. Lederer, D. Arvanitis, M. Tischer, G. Comelli, L. Troeger and K. Baberschke, *Physical Review B*, 1993, **48**, 11277–11286.

[112] C. Cohen, H. Ellmer, J. M. Guigner, A. L'Hoir, G. Prevot, D. Schmaus and M. Sotto, *Surface Science*, 2001, **490**, 336–350.

[113] B. Croset, Y. Girard, G. Prévot, M. Sotto, Y. Garreau, R. Pinchaux and M. Sauvage-Simkin, *Physical Review Letters*, 2002, **88**, 056103.

[114] G. Prevot, B. Croset, A. Coati, Y. Garreau and Y. Girard, *Physical Review B*, 2006, **73**, 205418.

[115] C.-Y. Lin and B. A. Jones, *Physical Review B*, 2011, **83**, 014413.

[116] C. F. Hirjibehedin, C.-Y. Lin, A. F. Otte, M. Ternes, C. P. Lutz, B. A. Jones and A. J. Heinrich, *Science*, 2007, **317**, 1199–203.

[117] C. D. Ruggiero, M. Badal, T. Choi, D. Gohlke, D. Stroud and J. A. Gupta, *Physical Review B*, 2011, **83**, 245430.

[118] P. O. Gartland, *Phys. Norv.*, 1972, **6**, 201.

[119] G. A. Haas and R. E. Thomas, *Journal of Applied Physics*, 1977, **48**, 86–93.

[120] C. D. Ruggiero, T. Choi and J. A. Gupta, *Applied Physics Letters*, 2007, **91**, 253106.

[121] E. Y. Tsymbal, O. N. Mryasov and P. R. LeClair, *Journal of Physics: Condensed Matter*, 2003, **15**, R109.

[122] G. Jonker and J. Van Santen, *Physica*, 1950, **16**, 337–349.

[123] A. Urushibara, Y. Moritomo, T. Arima, A. Asamitsu, G. Kido and Y. Tokura, *Physical Review B*, 1995, **51**, 103–109.

[124] O. Chmaissem, B. Dabrowski, S. Kolesnik, J. Mais, J. Jorgensen and S. Short, *Physical Review B*, 2003, **67**, 094431.

[125] M. Bowen, M. Bibes, A. Barthelemy, J.-P. Contour, A. Anane, Y. Lemaitre and A. Fert, *Applied Physics Letters*, 2003, **82**, 233.

[126] A. Millis, B. Shraiman and R. Mueller, *Physical Review Letters*, 1996, **77**, 175–178.

[127] A. Millis, R. Mueller and B. Shraiman, *Physical Review B*, 1996, **54**, 5405–5417.

[128] B. Nadgorny, I. Mazin, M. Osofsky, R. Soulen, P. Broussard, R. Stroud, D. Singh, V. Harris, A. Arsenov and Y. Mukovskii, *Physical Review B*, 2001, **63**, 184433.

[129] J.-H. Park, E. Vescovo, H.-J. Kim, C. Kwon, R. Ramesh and T. Vekantesan, *Nature*, 1998, **392**, 794–796.

[130] J. Krempaský, V. Strocov, L. Patthey, P. Willmott, R. Herger, M. Falub, P. Blaha, M. Hoesch, V. Petrov, M. Richter, O. Heckmann and K. Hricovini, *Physical Review B*, 2008, **77**, 165120.

[131] C. Zener, *Physical Review*, 1951, **81**, 440–444.

[132] P. W. Anderson and H. Hasegawa, *Physical Review*, 1955, **100**, 675–681.

[133] H. Y. Hwang, S.-W. Cheong, P. G. Radaelli, M. Marezio and B. Batlogg, *Physical Review Letters*, 1995, **75**, 914–917.

[134] J. Rodriguez-Carvajal, M. Hennion, F. Moussa, A. H. Moudden, L. Pinsard and A. Revcolevschi, *Physical Review B*, 1998, **57**, 3189–3192.

[135] W. Pickett and D. Singh, *Physical Review B*, 1996, **53**, 1146–1160.

[136] V. Ferrari, J. M. Pruneda and E. Artacho, *Physica Status Solidi (a)*, 2006, **203**, 1437–1441.

[137] B. Zheng and N. Binggeli, *Journal of Physics: Condensed Matter*, 2009, **21**, 115602.

[138] C. Ma, Z. Yang and S. Picozzi, *Journal of Physics: Condensed Matter*, 2006, **18**, 7717–28.

[139] A. Chikamatsu, H. Wadati, H. Kumigashira, M. Oshima, A. Fujimori, N. Hamada, T. Ohnishi, M. Lippmaa, K. Ono, M. Kawasaki and H. Koinuma, *Physical Review B*, 2006, **73**, 195105.

[140] V. M. Lebarbier, D. Mei, D. H. Kim, A. Andersen, J. L. Male, J. E. Holladay, R. Rousseau and Y. Wang, *Journal of Physical Chemistry C*, 2011, **115**, 17440–17451.

[141] H. Jalili, J. W. Han, Y. Kuru, Z. Cai and B. Yildiz, *The Journal of Physical Chemistry Letters*, 2011, **2**, 801–807.

[142] M. Martin, G. Shirane, Y. Endoh, K. Hirota, Y. Moritomo and Y. Tokura, *Physical Review B*, 1996, **53**, 14285–14290.

[143] J. Pruneda, V. Ferrari, R. Rurali, P. Littlewood, N. Spaldin and E. Artacho, *Physical Review Letters*, 2007, **99**, 226101.

[144] J.-L. Maurice, F. Pailloux, A. Barthélémy, O. Durand, D. Imhoff, R. Lyonnet, A. Rocher and J.-P. Contour, *Philosophical Magazine*, 2003, **83**, 3201–3224.

[145] F. Tsui, M. C. Smoak, T. K. Nath and C. B. Eom, *Applied Physics Letters*, 2000, **76**, 2421.

[146] M. Angeloni, G. Balestrino, N. G. Boggio, P. G. Medaglia, P. Orgiani and A. Tebano, *Journal of Applied Physics*, 2004, **96**, 6387–6392.

[147] R. Herger, P. Willmott, C. Schlepütz, M. Björck, S. Pauli, D. Martoccia, B. Patterson, D. Kumah, R. Clarke, Y. Yacoby and M. Döbeli, *Physical Review B*, 2008, **77**, 085401.

[148] F. Li, Y. Zhan, T.-h. Lee, X. Liu, A. Chikamatsu, T.-f. Guo, H.-j. Lin, J. C. A. Huang and M. Fahlman, *Journal of Physical Chemistry C*, 2011, **115**, 16947–16953.

[149] P. Yu, W. Luo, D. Yi, J. X. Zhang, M. D. Rossell, C. Yang, L. You, G. Singh-Bhalla, S. Y. Yang and Q. He, *PNAS*, 2012, **109**, 9710–9715.

[150] M. Yoshimoto, H. Maruta, T. Ohnishi, K. Sasaki and H. Koinuma, *Applied Physics Letters*, 1998, **73**, 187.

[151] M. Izumi, Y. Konishi, T. Nishihara, S. Hayashi, M. Shinohara, M. Kawasaki and Y. Tokura, *Applied Physics Letters*, 1998, **73**, 2497.

[152] S. Piskunov, E. Heifets, T. Jacob, E. Kotomin, D. Ellis and E. Spohr, *Physical Review B*, 2008, **78**, 121406.

[153] T. T. Fister, D. D. Fong, J. A. Eastman, P. M. Baldo, M. J. Highland, P. H. Fuoss, K. R. Balasubramaniam, J. C. Meador and P. A. Salvador, *Applied Physics Letters*, 2008, **93**, 151904.

[154] K. Katsiev, B. Yildiz, K. Balasubramaniam and P. A. Salvador, *Applied Physics Letters*, 2009, **95**, 092106.

[155] L. Poggini, S. Ninova, P. Graziosi, M. Mannini, V. Lanzilotto, B. Cortigiani, L. Malavolti, F. Borgatti, U. Bardi, F. Totti, I. Bergenti, V. A. Dediu and R. Sessoli, *Journal of Physical Chemistry C*, 2014, **118**, 13631–13637.

[156] J. Choi, H. Dulli, S.-H. Liou, P. A. Dowben and M. Langell, *Physica Status Solidi (B)*, 1999, **45**, 45–58.

[157] J. Choi, P. A. Dowben and E. W. Plummer, *Physical Review B*, 1999, **59**, 13453–13459.

[158] C. N. Borca, B. Xu, T. Komesu, H. Jeong, M. T. Liu, S. H. Liou and P. A. Dowben, *Surface Science Letters*, 2002, **512**, L346–L352.

[159] H. Dulli, P. A. Dowben, S.-H. Liou and E. W. Plummer, *Physical Review B*, 2000, **62**, 629–632.

[160] R. Bertacco and J. Olivier, *Surface Science*, 2002, **511**, 366–372.

[161] S. Piskunov, E. Kotomin, E. Heifets, J. Maier, R. Eglitis and G. Borstel, *Surface Science*, 2005, **575**, 75–88.

[162] M. de Jong, I. Bergenti, V. Dediu, M. Fahlman, M. Marsi and C. Taliani, *Physical Review B*, 2005, **71**, 014434.

[163] M. de Jong, I. Bergenti, W. Osikowicz, R. Friedlein, V. Dediu, C. Taliani and W. Salaneck, *Physical Review B*, 2006, **73**, 052403.

[164] S. Picozzi, C. Ma, Z. Yang, R. Bertacco, M. Cantoni, A. Cattoni, D. Petti, S. Brivio and F. Ciccacci, *Physical Review B*, 2007, **75**, 094418.

[165] C. Cheng, K. Kunc and M. H. Lee, *Physical Review B*, 2000, **62**, 409–418.

[166] B. Nadgorny, *Journal of Physics: Condensed Matter*, 2007, **19**, 315209.

[167] A. J. Millis, *Nature*, 1998, **392**, 147–150.

[168] P. Reinhardt, I. D. P. R. Moreira, C. D. Graaf, R. Dovesi and F. Illas, *Chemical Physics Letters*, 2000, **319**, 625–630.

[169] G. Pilania and R. Ramprasad, *Surface Science*, 2010, **604**, 1889–1893.

[170] S. Piskunov, T. Jacob and E. Spohr, *Physical Review B*, 2011, **83**, 073402.

[171] R. Hammami, H. Batis and C. Minot, *Surface Science*, 2009, **603**, 3057–3067.

[172] L. Gonzalez-Tejuca, C. H. Rochester, J. L. Garcia Fierro and J. M. D. Tascon, *Journal of the Chemical Society, Faraday Transaction*, 1984, **80**, 1089–1099.

[173] S. Bhaskar, D. Allgeyer and J. a. Smythe, *Applied Physics Letters*, 2006, **89**, 254103.

[174] J. Baniecki, M. Ishii, K. Kurihara, K. Yamanaka, T. Yano, K. Shinozaki, T. Imada, K. Nozaki and N. Kin, *Physical Review B*, 2008, **78**, 195415.

[175] V. Alexandrov, S. Piskunov, Y. F. Zhukovskii, E. A. Kotomin and J. Maier, *Integrated Ferroelectrics*, 2011, **123**, 10–17.

[176] L. Vitali, S. Fabris, A. M. Conte, S. Brink, M. Ruben, S. Baroni and K. Kern, *Nano Letters*, 2008, **8**, 3364–8.

[177] A. Mugarza, C. Krull, R. Robles, S. Stepanow, G. Ceballos and P. Gambardella, *Nature Communications*, 2011, **2**, 490.

[178] K. Park, *Physical Review B*, 2011, **83**, 064423.

[179] A. Mugarza, R. Robles, C. Krull, R. Korytar, N. Lorente and P. Gambardella, *Physical Review B*, 2012, **85**, 155437.

[180] S. Barraza-Lopez, M. C. Avery and K. Park, *Physical Review B*, 2007, **76**, 224413.

[181] S. Barraza-Lopez, M. C. Avery and K. Park, *Journal of Applied Physics*, 2008, **103**, 07B907.

[182] H. Wende, M. Bernien, J. Luo, C. Sorg, N. Ponpandian, J. Kurde, J. Miguel, M. Piantek, X. Xu, P. Eckhold, W. Kuch, K. Baberschke, P. M. Panchmatia, B. Sanyal, P. M. Oppeneer and O. Eriksson, *Nature Materials*, 2007, **6**, 516–520.

[183] S. Ninova, V. Lanzilotto, L. Malavolti, L. Rigamonti, B. Cortigiani, M. Mannini, F. Totti and R. Sessoli, *Journal of Materials Chemistry C*, 2014, **2**, 9599–9608.

[184] L. Malavolti, V. Lanzilotto, S. Ninova, L. Poggini, I. Cimatti, B. Cortigiani, L. Margheriti, D. Chiappe, E. Otero, P. Sainctavit, F. Totti, A. Cornia, M. Mannini and R. Sessoli, *Nano Letters*, 2014, DOI: 10.1021/nl503925h.

[185] I. Cimatti, S. Ninova, V. Lanzilotto, L. Malavolti, L. Rigamonti, B. Cortigiani, M. Mannini, E. Magnano, F. Bondino, F. Totti, A. Cornia and R. Sessoli, *Beilstein Journal of Nanotechnology*, 2014, **5**, 2139–2148.

[186] M. A. Barral, R. Weht, G. Lozano and A. María Llois, *Physica B*, 2007, **398**, 369–371.

[187] C. F. Hirjibehedin, C. Y. Lin, A. F. Otte, M. Ternes, C. P. Lutz, B. A. Jones and A. J. Heinrich, *Science*, 2007, **317**, 1199–1203.

[188] G. Giovannetti, G. Brocks and J. van den Brink, *Physical Review B*, 2008, **77**, 035133.

[189] A. Rahmati, M. Ghoohestani, H. Badehian and M. Baizaee, *Material Research-Ibero-American Journal of Materials*, 2014, **17**, 303–310.

ACKNOWLEDGEMENTS

First of all, I would like to thank Federico Totti, Roberta Sessoli, and Andrea Caneschi for the possibility to continue my studies as a PhD student. It has been a very special experience for me due to its impact on my professional and personal growth.

I thank my supervisor, Federico Totti, for his help and assistance with my research project, as well as for his infinite patience and understanding during these three years.

The collision between theory and experiment has led to many fruitful discussions with the experimental team at the Laboratory for Molecular Magnetism (LAMM). In particular, I would like to thank Luigi Malavolti, Lorenzo Poggini, Irene Cimatti and Matteo Mannini for their help with the experimental surface science. Special thanks to Valeria Lanzilotto for her patience in unveiling to me the world of the spectroscopic techniques.

I would also like to thank my colleagues from the theoretical subgroup, Alessandro Lunghi, Guglielmo Fernandez Garcia, Matteo Briganti, Sara Giachetti, for the many useful discussions on computational chemistry (and not only). The ease with which they combine the hard work and fun, as well as their passion for theoretical science have always inspired me.

My gratitude extends to my close friends, who have had faith in me, supported me and lived through the emotions of the PhD program with me. My most sincere thanks go to Marie-Emmanuelle Boulon, Quentin Bodart, Diego Voccia, Tsveta Miteva, and Meryal Sabrieva.

Last but not least, I would like to thank my family and my boyfriend, Federico Bertelli, for their love and support.